

# Recent Progress in Silicon-Based Photonic Integrated Circuits and Emerging Applications

Zian Xiao, Weixin Liu, Siyu Xu, Jingkai Zhou, Zhihao Ren, and Chengkuo Lee\*

In recent years, with the further miniaturization of the semiconductor device in integrated circuits, power consumption and data transmission bandwidth have become insurmountable obstacles. As an integrated technology, photonic integrated circuits (PICs) have a promising potential in the post-Moore era with more advantages in data processing, communication, and diversified sensing applications for their ultra-high process speed and low power consumption. Silicon photonics is believed to be an encouraging solution to realize PICs because of the mature CMOS process. The past decades have witnessed a huge growth in silicon PICs. However, there is still a demand for the development of silicon PICs to enable powerful chip-scale systems and new functionalities. In this paper, a review of the photonic components, functional blocks, and emerging applications for PICs is offered. The common photonic components are classified into several sections, including on-chip light sources, fiber-to-chip couplers, photonic resonators, waveguide-based sensors, on-chip photodetectors, and modulators. The functional blocks of the PICs mentioned in this review are photonic memories and photonic neural networks. Finally, the paper concludes with emerging applications for further study.

## 1. Introduction

The rapid development of the Internet of Things (IoT) and the increased demand for computing services on the cloud have attracted more investigation into modern intelligent hardware systems to process data.<sup>[1,2]</sup> Although various custom electronic hardwares has been made to reduce energy consumption and improve data process performance, they still cannot part with the

basic electronic components of MOSFET. The speed and energy of these custom hardware are limited by electromagnetic crosstalk and Joule heating from their intrinsic resistor.<sup>[3]</sup> Meantime, capacitance uses up most energy and limits the maximum clock frequency in the high-performance computational unit because the movement of data requires the charging and discharging of chip-level metal interconnects. Consequently, numerous studies on innovative techniques for IoT and alternative designs for data processing have been conducted.<sup>[4–11]</sup>

With the good performance of light for long distances communication, integrated photonics also gets great achievements in sensing and computational operations.<sup>[12–20]</sup> Integrated photonics benefits from the batch microfabrication methods with the development of semiconductor fabrication.<sup>[21–23]</sup> Compared to silicon electronic devices, integrated photonics has three key obvious advantages. First, integrated photonics have the ability

to transfer data through multiplexing techniques, such as mode division multiplexing and wavelength division multiplexing (WDM). Second, integrated photonics can achieve extremely high modulation speed which is limited only by the bandwidth of optical modulators and photodetectors. Third, the photon is a kind of boson with zero rest mass, so the energy loss during signal transmission is small.<sup>[24]</sup> These unique advantages of photonics have led to its widespread use for information transmission and data processing. Integrated photonics not only has the characteristics of small size, low cost, and high integration but also take the advantage of broad bandwidth, high modulation speed, and multiple channels of optoelectronics.

Currently, we are on the cusp of integrated photonic technology innovation. Integrated photonics is a promising low-cost and mass-produced solution to a variety of technology areas.<sup>[25,26]</sup> Same to electronic integrated circuits, integrated photonic blocks are built up by many functional devices, like on-chip light sources, fiber-to-chip couplers, photonic resonators, photonic sensors, photodetectors, photonic tuning devices, photonic memories and so on. Complex systems are all based on the fundamental building blocks to fulfill complex functions, such as data encryption, photonic computing, spectrometer, beam scanning, and chemical sensing from near-infrared to far-infrared as shown in Figure 1.<sup>[27–32]</sup> By combining photonic chips and electronic chips, both can leverage and maximize their unique strengths.

Z. Xiao, W. Liu, S. Xu, J. Zhou, Z. Ren, C. Lee  
 Department of Electrical and Computer Engineering  
 National University of Singapore  
 4 Engineering Drive 3, Singapore 117583, Singapore  
 E-mail: elec@nus.edu.sg

Z. Xiao, W. Liu, S. Xu, J. Zhou, Z. Ren, C. Lee  
 Center for Intelligent Sensors and MEMS  
 National University of Singapore  
 4 Engineering Drive 3, Singapore 117583, Singapore  
 C. Lee  
 NUS Graduate School-Integrative Sciences and Engineering Programme (ISEP)  
 National University of Singapore  
 Singapore 119077, Singapore

 The ORCID identification number(s) for the author(s) of this article can be found under <https://doi.org/10.1002/adom.202301028>

DOI: 10.1002/adom.202301028

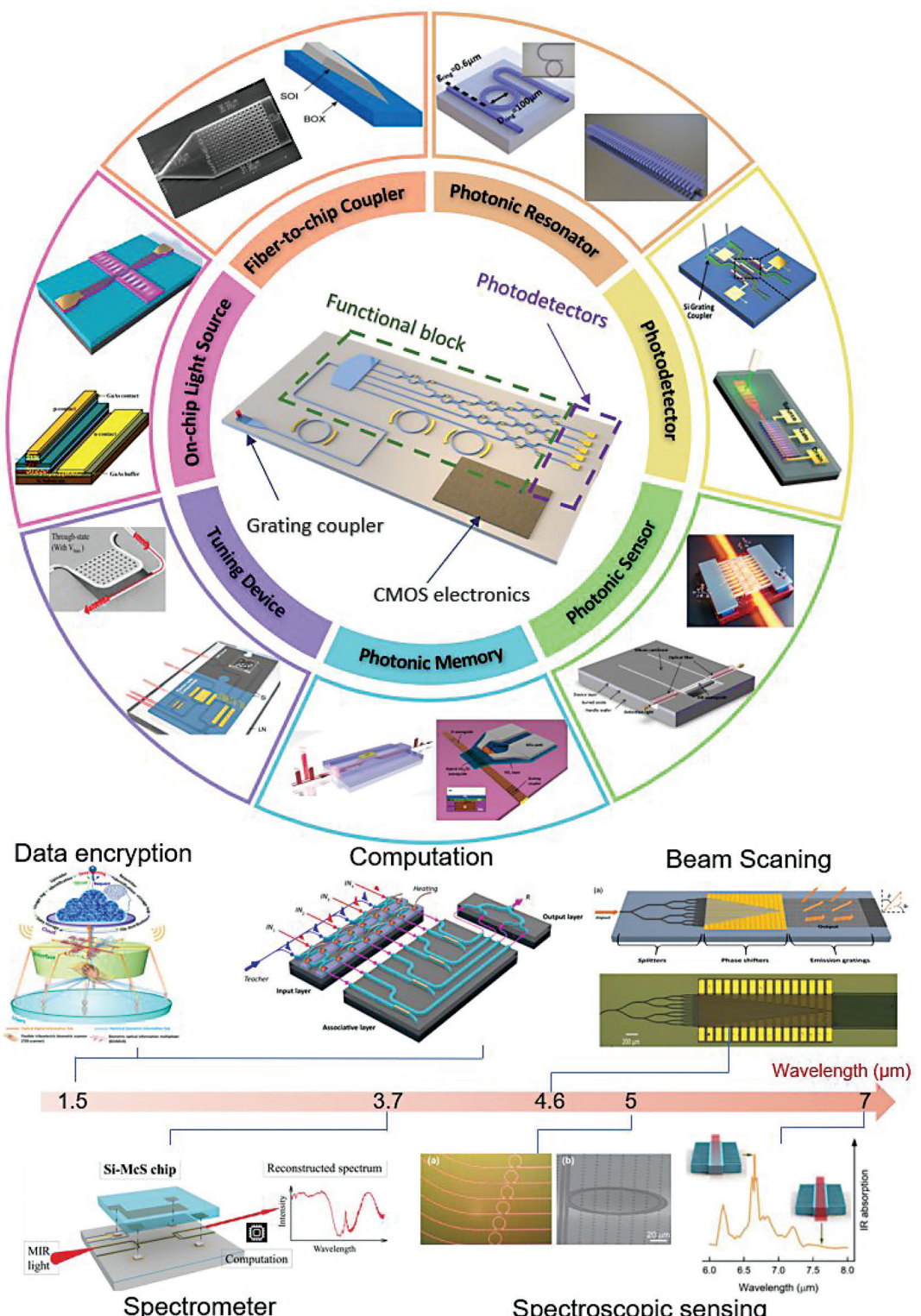


**Figure 1.** (Top) Schematic illustration for the electro-photonics integrated circuits and their subdevices. Electro-photonics integrated circuits combine the CMOS electronics chips and photonic functional blocks. Fiber-to-chip couplers can guide the light from off-chip fiber to chips. Photodetectors can convert the optical signal to electric signal for electronics chips. Electronics chips can control the performance of functional blocks (bottom) and applications at different wavelengths, such as data encryption, Adapted with permission.<sup>[27]</sup> Copyright 2022, American Association for the Advancement of Science. Photonic computing. Adapted with permission.<sup>[28]</sup> Copyright 2022, Optica Publishing Group. Spectrometer. Adapted with permission.<sup>[29]</sup> Copyright 2022, American Chemical Society. Beam scanning. Adapted with permission.<sup>[30]</sup> Copyright 2022, Optica Publishing Group. Spectroscopic sensing. Adapted with permission.<sup>[31]</sup> Copyright 2022, De Gruyter.

Reasonable functional distributions between photonic chips and electronic chips could be more advanced and more productive in the next generation of optoelectronic chips.<sup>[21,33–35]</sup>

The development of PICs goes through four stages: First, microelectronic process-based photonic devices replace discrete components, which helps enable process standardization. Second, photonic devices are integrated onto a single chip, achieving partial integration. Third, photoelectric integration technology integrates both light and electricity to achieve more complex functions. Finally, PICs technology substituted the electronics integrated circuits. With the continuous development of photonic technology and nanofabrication process, PICs will be widely popularized based on long-term coexistence with electronic integrated circuits.

In this review paper, we report the development trends and perspective of the silicon-based photonic devices and photonic functional blocks that can be integrated into chips during recent decades. For devices, the on-chip light sources are reviewed in Section 2. For off-chip light sources, fiber-to-chip interconnects are very important. The edge couplers and grating couplers were discussed in Section 3. Then, to enhance the wavelength selectivity, photonic resonators are also introduced in Section 4. After that, Section 5 and Section 6 review waveguide-based physical sensors and bio/chemical sensors, respectively. Section 7 summarizes the advanced on-chip photodetectors. To tune the optical signal, modulators are discussed in Section 8 and photonic memories are introduced in Section 9. Section 10 reviews the photonic neural network. In the last section, some specific application scenarios are talked about, such as wearable photonics, data encryption, human-machine interface, light detection and ranging (LiDAR) and integrated optoelectronic systems with a frequency comb. Finally, we conclude with the advantages and disadvantages of integrated photonics.

## 2. On-Chip Light Source

The silicon-based on-chip light source is a crucial component for PICs.<sup>[42–44]</sup> For silicon-based photonics, there are on-chip light source solutions and off-chip light source solutions. An off-chip light source offers advantages such as high light-emitting efficiency and reliable temperature control. Most published photonic systems rely on external light sources through fiber-to-chip couplers. Off-chip lasers allow to optimize photonic performance avoiding complicated process for on-chip lasers. However, the fiber-to-chip couplers introduce additional loss through off-chip laser. Additionally, the high package cost prevents co-packaging with off-chip lasers. On-chip lasers became increasingly urgent to improve system integration.

Extensive research has been conducted on several promising candidates for on-chip light sources, such as porous Si,<sup>[45]</sup> Si nanocrystals,<sup>[46]</sup> carbon nanotube emitter,<sup>[46–48]</sup> Si Raman lasers,<sup>[49–51]</sup> erbium (Er)-related light sources,<sup>[52–54]</sup> germanium (Ge)-on-Si lasers<sup>[55–58]</sup> and III-V based Si lasers.<sup>[59–66]</sup> According to their comprehensive performance, this section will mainly introduce Carbon nanotube emitter, Raman laser, Er-related light source, Ge-on-Si laser, and III-V based laser.

### 2.1. Carbon Nanotube Emitter

Semiconducting carbon nanotube (SCNT) is first reported by Misewich in 2003.<sup>[67]</sup> Device examples of light emission from SCNT have previously been demonstrated which all use traditional metallic electrodes.<sup>[68–70]</sup> However, metallic electrodes induce optical absorption loss and degrade the resonance modes of photonic cavities.<sup>[71,72]</sup> To overcome these challenges, nanocrystalline graphene electrodes are proposed instead of metallic electrodes.

Graphene electrodes show negligible optical insertion loss and do not cause quality factor ( $Q$ ) degradation. The schematic of the SCNT laser with graphene electrodes is shown in Figure 2a-i. The  $\text{Si}_3\text{N}_4$  is used as a waveguide. The scanning electron microscope (SEM) image is shown in Figure 2a-ii. The SCNT is localized in the cavity. The graphene electrodes act as source and drain electrodes. The underlying silicon substrate works as the back gate. A vertical electric field is generated between the SCNT and the Si substrate by applying a voltage to the back gate, enabling control of the charge in the SCNT channel. In this field-effect configuration, photons are emitted from the electrically driven SCNT.

### 2.2. Raman Laser

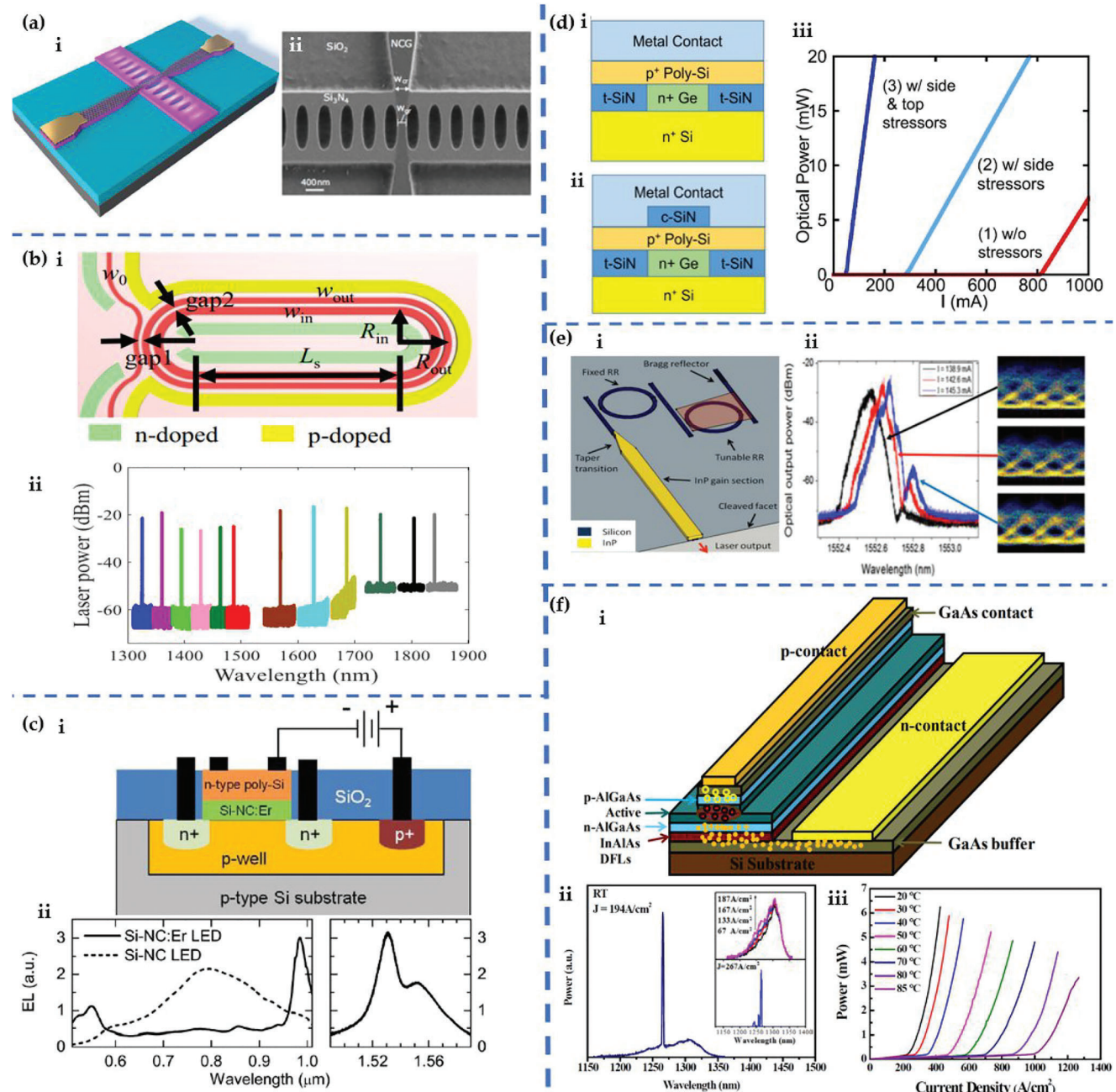
Silicon Raman lasers have the potential to serve as ideal light sources, due to their independence from phase-matching requirements and the ability to emit light in the mid-infrared wavelength range.<sup>[50,73–78]</sup> Raman lasers based on stimulated Raman scattering in high-Q resonators are promising for tunable on-chip lasers due to their low pump threshold powers and high output power.

Figure 2b-i illustrates a broadly tunable Raman laser with a high-Q multimode racetrack resonator.<sup>[37]</sup> It has a broad output wavelength range from 1325 to 1841 nm through a broadband high-Q multimode racetrack resonator. The multimode racetrack resonator achieves a high  $Q$  about  $1.4 \times 10^6$  over the wavelength from 1240 to 1680 nm. Figure 2b-ii provides selective laser output spectra at several fixed pump wavelengths. As the pump wavelength increases, the laser output power decreases due to the inverse relationship between the Raman gain coefficient and the Stokes wavelength. Additionally, the longer wavelength results in a larger free-carrier absorption coefficient, contributing to the reduction in output power.

A highly versatile Raman laser with tunability across a wide wavelength range was demonstrated by Ahmadi et al. in 2021.<sup>[79]</sup> The tunable directional coupler within the cavity is used to optimize both pump and signal coupling coefficients. The laser incorporates a ring cavity surrounded by a p-i-n junction, effectively eliminating free carriers and reducing nonlinear loss.

### 2.3. Er-Related Light Source

Extensive research has been conducted on Er-containing light sources due to the 1550 nm emission from  $\text{Er}^{3+}$  ions.<sup>[80–86]</sup> There are two types of Er-containing light sources: Er-doped materials and Er compound materials. Er compound materials have more Er density than Er-doped materials to increase the optical gain.



**Figure 2.** Silicon-based on-chip light source. a-i) Schematic of carbon nanotube emitter from Anna et al. a-ii) Scanning electron microscope image of the device. Adapted with permission.<sup>[36]</sup> Copyright 2023, Springer Nature. b-i) Schematic of the Raman laser from Zhang et al. b-ii) Laser output spectrum at different pump wavelengths. Adapted with permission.<sup>[37]</sup> Copyright 2022, Springer Nature. c-i) Schematic cross-section of the Si-NC:Er LED layout from Anopchenko et al. c-ii) Integrated EL spectral intensity. Adapted with permission.<sup>[38]</sup> Copyright 2012, American Institute of Physics. d-i) Ge laser with side nitride stressors from Ke et al. d-ii) Ge laser with top and side nitride stressors. d-iii) Integrated EL spectral intensity. Adapted with permission.<sup>[39]</sup> Copyright 2017, IEEE. e-i) Schematic of hybrid III-V/Si laser from Valicourt et al. e-ii) Output spectra depending on the active zone bias current. Adapted with permission.<sup>[40]</sup> Copyright 2015, Optica Publishing Group. f-i) Schematic of an InAs/GaAs quantum dot laser grown on a Si substrate from Tang et al. f-ii) Lasing spectrum. f-iii) Light output power against current density. Adapted with permission.<sup>[41]</sup> Copyright 2014, Optica Publishing Group.

The majority of Er ions in Er compound materials are optically active which is different from Er-doped materials. Among these materials, the Er-doped silicon nanocluster system has garnered significant interest as a gain medium in silicon photonics, which is grown by a CMOS-compatible process.

Figure 2c-i illustrates the schematic of the Er-doped silicon nanocluster light-emitting diode (LED) layout.<sup>[38]</sup> Figure 2c-ii displays the electroluminescence spectra of both the silicon nanocluster LED and the Er-doped silicon nanocluster LED at an injected current of 2  $\mu\text{A}$ . The external quantum efficiency of this

device at  $1.54\text{ }\mu\text{m}$  is also shown in Figure 2c-ii. It is worth noting that accessing Er emission at low voltages requires moderate injection frequencies.

#### 2.4. Ge-on-Si Laser

For PICs, silicon is an indirect-bandgap semiconductor, which limits its efficiency as a light emitter. To address this limitation, the integration of on-chip lasers in PICs has predominantly been accomplished using direct-bandgap compound semiconductors. The germanium (Ge)-on-Si laser presents a compelling option for future large-scale monolithic integration.<sup>[55–57,87,88]</sup> Its significant advantage over III-V-based Si lasers lies in its compatibility with Si technology in terms of materials and processing. Theoretical predictions in 2007 highlighted the potential for achieving light emission from Ge through band engineering with tensile strains and high doping levels.<sup>[58]</sup> Notably, n-type doping, the introduction of tensile strain, or the utilization of germanium–tin alloy are the three primary approaches employed to modify the band structure of Ge. These approaches can transform Ge from an indirect bandgap material to a direct bandgap material, thereby increasing the gain.

To further optimize the performance of Ge lasers, SiN stressors are employed to introduce tensile strain.<sup>[89]</sup> Figure 2d-i,ii illustrates the cross sections of the two structures. Specifically, Figure 2d-ii showcases the cross-section featuring side nitride stressors, while Figure 2d-iii depicts the cross-section with both top and side nitride stressors. In comparison to structure 1, the inclusion of side stressors resulted in a reduction of approximately  $523\text{ mA}$  in threshold current and an increase of 1.05% in wall-plug efficiency. Moreover, with the addition of top and side stressors, a further reduction of approximately  $761\text{ mA}$  in threshold current and a notable growth of 14% in wall-plug efficiency was achieved. Figure 2d-iii shows integrated EL spectral intensity. The significant enhancement in performance attributed to the top stressors can be attributed to their ability to introduce higher stress levels, reduce optical losses caused by metal contacts, and provide optical confinement in the vertical direction.

#### 2.5. III-V Based Laser

Taking benefits from the direct bandgap structures, integrating III-V semiconductors on Si substrates shows a promising path for on-chip light sources.<sup>[90–92]</sup> However, the lattice constants mismatch and thermal expansion coefficients of Si and III-V materials lead to a notable density of defects, including threading or misfit dislocations at the interface. The direct growth of III-V gain materials on a silicon-on-insulator (SOI) platform faces impediments. Several integration approaches have been explored for III-V materials integration, such as heterogeneous bonding, transfer printing, and epitaxial growth.

An InP/Si laser is demonstrated by Valicourt et al. in 2015 through bonding technology.<sup>[40]</sup> This laser structure comprises a passive section in silicon and an active region based on InP, as illustrated in Figure 2e-i. The corresponding measured spectra are depicted in Figure 2e-ii. To fabricate the device, the III-V part was bonded onto the silicon wafer. Additionally, heaters are integrated on top of the ring resonators to achieve thermal tuning

of the resonance peaks. The two rings are intentionally designed with slightly different expected free spectral ranges (FSRs) to create a Vernier effect, enabling the laser to operate in a single mode.

The utilization of nano-structures, particularly quantum dots (QDs), presents a viable method to suppress threading dislocations.<sup>[93,94]</sup> III-V QDs lasers are particularly attractive for reduced temperature sensitivity and low threshold current density.<sup>[95,96]</sup> Furthermore, the discrete distribution of threading dislocations enhances tolerance to defects and enables effective filtering of TDs, setting them apart from traditional bulk material and quantum well technologies.

III-V quantum dot lasers hold great promise due to their favorable properties, which are shown in Figure 2f-i. InAlAs/GaAs is used as a dislocation filter layer to reduce the density of threading dislocations. Additionally, Figure 2f-ii exhibits the lasing spectrum of a Si-based InAs/GaAs QD laser at an injection current density of  $194\text{ A cm}^{-2}$ . The characteristic between the output power and current density at different temperatures for this laser is illustrated in Figure 2f-iii.

In summary, the on-chip lasers are one kind of the key component in PICs. As long as a good trade-off solution between efficiency and lifetime can be found, on-chip lasers will be suitable for low-speed, large-volume optical interconnects. Among different kinds of solutions, III-V-based silicon lasers currently exhibit the highest performance and show significant potential for immediate commercial applications. The direct hetero-epitaxial growth of III-V materials on Si appears more promising for achieving low-cost and high-yield fabrication.

### 3. Fiber-to-Chip Coupler

Integrating an on-chip laser and photodetector with a single device for testing purposes can be costly. Therefore, efficiently guiding light from a fiber into a photonic chip or vice versa is crucial.<sup>[97]</sup> Generally, the most common solutions for such optical interconnects are namely edge coupling (or butt coupling) and grating coupling (or vertical coupling) according to the relative position of the fiber and the photonic chip, which can guide the light from fiber to photonic chips, or from photonic chips to fiber.<sup>[98]</sup> Edge couplers and grating couplers are passive flexible solutions to check the optical signal in the chip using an external laser light source. One of the key challenges with such devices is enabling high coupling efficiency, which is due to mode-field differences between fibers and waveguides, and the relative misalignments. However, the butt coupler requires a deep trench on the edge of the photonic chips due to its location, which means the fabrication process of butt couplers is more complicated.

For the edge coupling regime as shown in Figure 3a-i, the fiber (red one) is typically aligned horizontally with the edge coupler at the chip facet. The diameter of fiber cladding is around  $250\text{ }\mu\text{m}$ , which is bigger than the size of a fiber-to-chip coupler. In the chip-to-fiber propagation case, as the taper region decreases gradually, light confinement weakens, and the mode size becomes larger. The reverse occurs in the fiber-to-chip case, with the fiber mode distribution being confined in the gradually shrinking taper waveguide. To enhance the coupling efficiency and minimize propagation loss, a properly smooth and polished facet is necessary, resulting in additional fabrication costs in mass manufacturing. Edge couplers have large coupling efficiency and

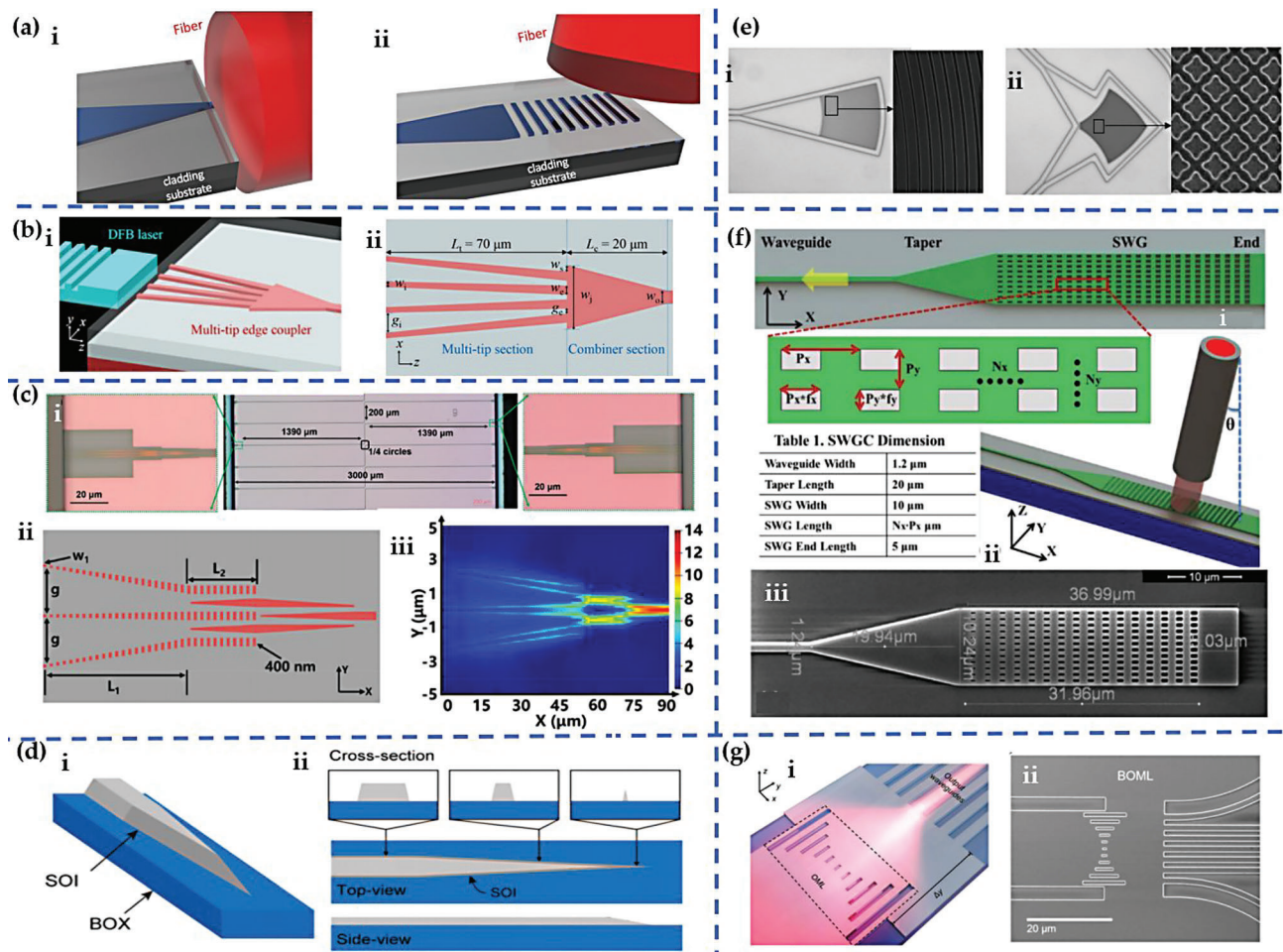


**Figure 3.** State-of-the-art grating couplers and edge couplers. a-i) An edge coupler based on an SOI wafer. a-ii) Grating coupler based on an SOI wafer. b-i) Double-tip edge coupler from Wang et al. b-ii) Optical micrograph of a 40  $\mu\text{m}$  long double-tip edge coupler. Adapted with permission.<sup>[100]</sup> Copyright 2019, IEEE. c-i) Optical micrograph of subwavelength metamaterial edge coupler from He et al. Adapted with permission.<sup>[101]</sup> Copyright 2021, American Chemical Society. c-ii) Top view of subwavelength metamaterial edge coupler. c-iii) The electric field distribution. d-i) Knife-edge taper from Takei et al. Adapted with permission.<sup>[102]</sup> Copyright 2013, American Institute of Physics. d-ii) Cross-section of knife-edge taper. e-i) Optical micrograph of single polarization grating coupler from Mekis et al. Adapted with permission.<sup>[103]</sup> Copyright 2011, IEEE. e-ii) Optical micrograph of a polarization-splitting grating coupler from Chen et al. Adapted with permission.<sup>[104]</sup> Copyright 2018, Optica Publishing Group. f-i) Top-view of a subwavelength grating coupler from Chen et al. Adapted with permission.<sup>[104]</sup> Copyright 2018, Optica Publishing Group. f-ii) Subwavelength grating coupler. f-iii) The SEM image of a subwavelength grating coupler. g-i) Bigradient on-chip metalens from Ren et al. g-ii) SEM image of fabricated bigradient on-chip metalens. Adapted with permission.<sup>[105]</sup> Copyright 2021, Wiley-VCH.

broad bandwidth, and recent researches show that coupling efficiencies are greater than  $-0.5$  dB over 100 nm of bandwidth.<sup>[99]</sup> What's more, edge coupling has low fiber-chip alignment tolerance. Meanwhile, edge couples cannot provide a wafer-level testing solution for its position on the photonic chips, which will further increase the cost and require higher accuracy for testing and packaging.

A schematic of the most common grating coupler is shown in Figure 3a-ii. A grating coupler consists of a periodic arrangement of different materials or structures.<sup>[106]</sup> On the SOI platforms, it is realized through etching in most cases, where the waveguide is silicon, and the substrate is buried silicon oxide (BOX). To guarantee a high coupling efficiency, the fiber is positioned vertically or slightly inclined at a specific angle above the device, which is dependent on the coupler design. Grating couplers provide a surface solution for convenient testing and can be positioned any-

where on a wafer. Besides, grating couplers have several benefits including compact size, low fabrication cost, and the ability to conduct wafer-level testing, while there are also some drawbacks such as a relatively low coupling efficiency, narrow bandwidth, and high wavelength sensitivity.

Edge couplers have been widely studied, and the inverse shrinking taper structure plays an important role in couplers. To achieve broad bandwidth, low coupling loss, compact size, and CMOS compatible, different structures of edge couplers are investigated. For horizontal direction structure, edge couplers are divided into several types, inverse tapers with non-linear profiles, multi-tip tapers, multiple tapers, and subwavelength grating structures.<sup>[107]</sup> To avoid the impacts of fabrication accuracy, a double-tip inverse taper is demonstrated for its high coupling efficiency. Moreover, the double-tip taper can improve the bandwidth and misalignment tolerance.<sup>[108]</sup> As shown

in Figure 3b-i, a double-tip inverse taper was fabricated on the SOI platform with a 220 nm top silicon layer through chlorine-based dry etching.<sup>[100]</sup> Multimode Interference (MMI) optical combiner has a high fabrication tolerance. Figure 3b-ii shows the optical micrograph of a 40 μm-long edge coupler sample, and such taper shows that a compact fiber coupler can achieve high coupling efficiency ( $\approx 1.1$  dB) at 1550 nm wavelength for both transverse-electric (TE) and transverse-magnetic (TM) modes.

Metamaterials, which artificially consist of subwavelength structures, have garnered significant research attention in microelectromechanical systems (MEMS) and photonics.<sup>[109–112]</sup> With their artificial optical features, curious physical phenomena have been observed in metamaterials, such as negative refractive index,<sup>[113,114]</sup> slow light effect,<sup>[115]</sup> and perfect absorption.<sup>[116–122]</sup> Metamaterials provide a novel solution compared to traditional materials for controlling light at the nanoscale.<sup>[123–128]</sup> Recently, they have emerged as a versatile toolkit for creating advanced metadevices with greatly improved efficiency. The deployments of on-chip metamaterials have led to the realization of high-performing and ultracompat building blocks, such as metalenses,<sup>[129]</sup> subwavelength photonics,<sup>[130,131]</sup> beam splitters<sup>[132,133]</sup> and nanoantenna sensors.<sup>[134–138]</sup>

By leveraging the metamaterial Si waveguide, as shown in Figure 3c-i, a subwavelength metamaterial edge coupler with multi-tapers is proposed.<sup>[101]</sup> Because the index contrast can be effectively reduced by leveraging the strengths of metamaterial, the footprint of this edge coupler is 90 μm, which is much less than other designs, and this edge coupler is fully CMOS process compatible. The coupling loss is 2.22/2.53 dB per facet at 1550 nm for TE/TM mode, and the bandwidth can reach 120 nm. Figure 3c-ii shows the structure of the subwavelength metamaterial edge coupler and the electric field distribution simulation is also shown in Figure 4c-iii.

Besides the horizontal structural transformations, many efforts have been paid to the vertical direction for edge couplers. To further increase the coupling efficiency, the optical mode should be fully expanded outside the silicon core at the end of the taper. So, it has strict requirements for fabricating such ultranarrow taper structures due to photolithographic resolution limits. To overcome such challenges, a double-patterning method is used in a knife-edge taper, which is shown in Figure 3d-i.<sup>[139]</sup> This edge coupler can have a tip width much smaller than 50 nm. The cross-section of the taper, shown in Figure 3d-ii, features a gradual decrease in height and width near its end. Such structure can further decrease the mode conversion loss to 0.35 and 0.21 dB for the TE- and TM-like modes.

Compared with edge couplers, vertical grating coupler occupies the majority of the fiber-to-chip couplers. It changes the direction of light from fiber to on-chip waveguide direction via grating structures and a spot-size converter is used to couple the light into the on-chip waveguide. The Bragg condition can explain this wave-vector conversion. The Bragg condition can be satisfied for different wavelengths by adjusting the parameters such as grating pitch, grating period, and beam incident angle. Vertical grating couplers offer several advantages, such as their compatibility with wafer-level testing without wafer dicing, flexibility in alignment and measurement, and a more compact size over edge coupler.

The simplest vertical grating coupler design is based on the periodic structure in one dimension. Figure 3e-i shows a schematic cross-sectional view of a single polarization grating coupler.<sup>[103]</sup> Polarization is one of the most important characteristics of light. This kind of design can only couple light that is polarized perpendicular to the plane of the figure, which means the transverse waveguide mode faces large loss with the orthogonal polarization state. As previously stated, the single polarization grating coupler can serve either as an input or an output port, provided the polarization of the incoming signal is known.

The other type of polarization-related grating coupler is the polarization-splitting grating coupler, which can couple both polarization from the fiber efficiently. As shown in Figure 4e-ii, this coupler has a grating periodic in two dimensions.<sup>[103]</sup> The polarization-splitting grating coupler can direct light from a fiber into two separate waveguides that have orthogonal polarization. The separated two waveguides receive the light polarized perpendicular to their respective axis, with the amplitude and phase of the light in each waveguide being determined by the polarization state of the incident mode. However, the performance of the polarization-splitting grating coupler is limited by the fabrication process due to its complex structure.

Apart from the structure of the grating, the coupling efficiency can also be increased through the recycling of the downward radiated power. To achieve a better performance, one widely investigated approach is using a bottom metal mirror.<sup>[140–142]</sup> By incorporating a metal reflector, the reflection of the light diffracted toward the substrate towards the grating can be maximized to near 100% reflectivity. The multilayer Bragg reflector is also investigated to enhance performance.<sup>[143,144]</sup>

For an efficient grating coupler that is simple in structure and easy to fabricate, the subwavelength grating coupler is the preferred option, as shown in Figure 3f-i.<sup>[104]</sup> The subwavelength grating coupler can provide higher degree of freedom for the effective index engineering. The single-mode fiber is angled at  $\theta$  to promote mode matching and suppress the second-order Bragg back reflection loss as shown in Figure 3f-ii, where the actual oxide cladding is visually neglected. Figure 3f-iii shows the SEM photo of the subwavelength grating coupler. This structure offers a broad bandwidth for mid-infrared.

Inverse design has been widely used in the design of integrated photonic devices.<sup>[145–149]</sup> Compared to traditional design methods, inverse design methods can accelerate the design process of silicon photonics.<sup>[150,151]</sup> In 2021, Cheng et al. presented an ultra-compact dual-mode grating coupler through inverse design method, which has a small footprint of 10 μm, a small insertion loss of 1.02/1.59 dB for TE<sub>0</sub>/TE<sub>1</sub> mode and a large equivalent linear taper angle of 40.4°.<sup>[152]</sup>

However, there are some drawbacks to grating couplers. First, the grating's narrow bandwidth results from the fact that only light within a specific wavelength range that satisfies the phase match condition can pass through it. Secondly, the inherent diffraction and scattering in the grating structure result in low coupling efficiency. Finally, the high directionality of the grating's teeth, which is sensitive to the oscillation direction of the electromagnetic vector, causes polarization sensitivity in the wave-vector conversion.

To further minimize the on-chip optical systems, an on-chip metalens is proposed to achieve ultrasmall focal lengths and spot

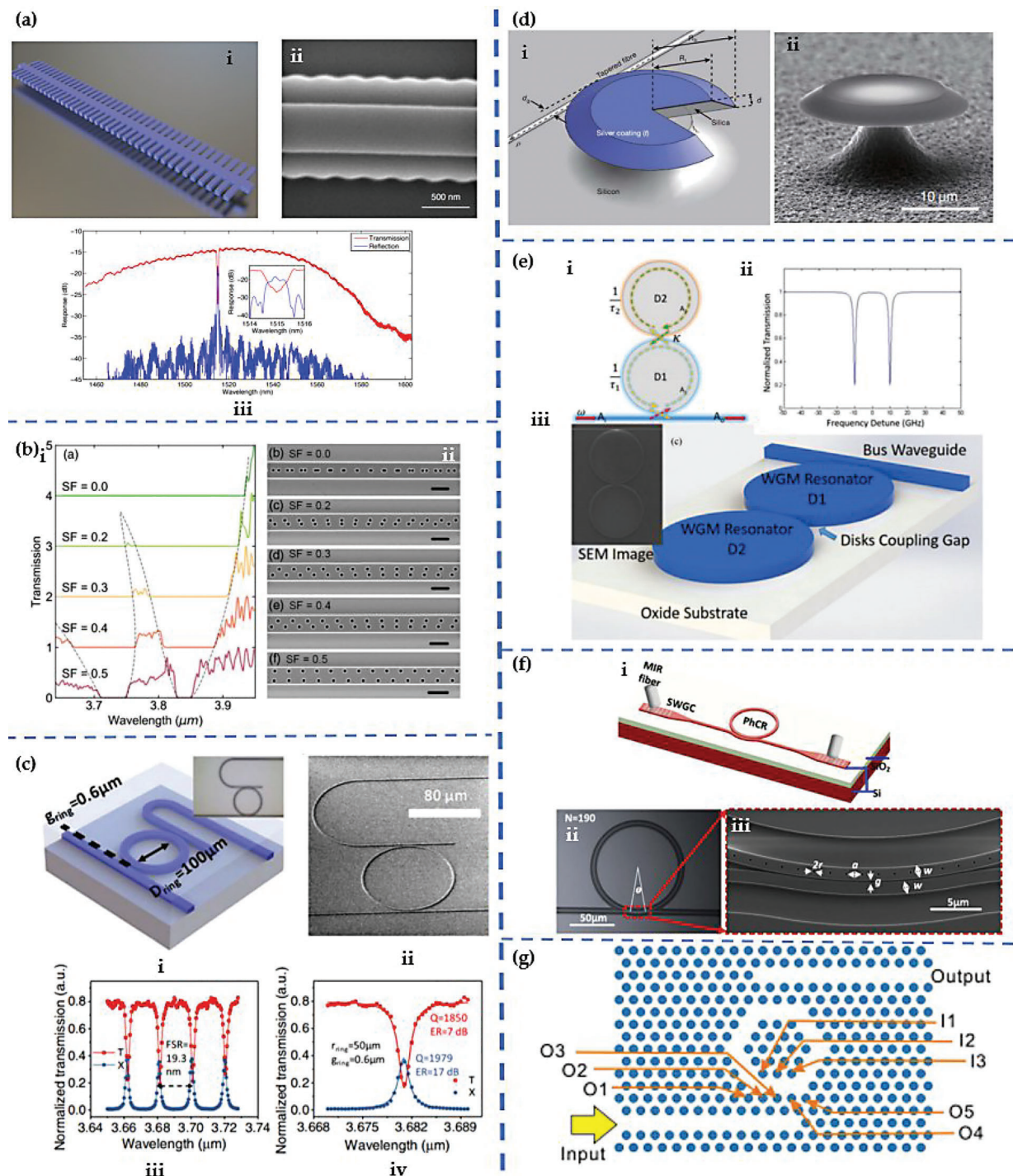


**Figure 4.** Photonic high-quality resonators. a-i) Bragg grating. a-ii) Grating on the slab: corrugation width on each side is 80 nm from Wang et al. Adapted with permission.<sup>[205]</sup> Copyright 2012, Optica Publishing Group. a-iii) Measured spectral responses of the Bragg grating on ridge waveguides on the slab. b-i) Measured transmission of aperiodic PhC nanobeams with different SFs from Wei et al. Adapted with permission.<sup>[213]</sup> Copyright 2018, Optica Publishing Group. b-ii) SEM image of the aperiodic PhC nanobeams with different SFs. c-i) Ring resonator based on AlNOI platform from Dong et al. Adapted with permission.<sup>[229]</sup> Copyright 2018, Optica Publishing Group. c-ii) SEM of AlN ring resonator based on AlNOI platform. c-iii) Spectrum of AlN ring resonator with  $r = 50 \mu\text{m}$ . c-iv) Zoom-in peak at 3.682  $\mu\text{m}$ . d-i) 2D SPP microdisk resonator with a tapered optical fiber passing under its edge from Min et al. Adapted with permission.<sup>[231]</sup> Copyright 2009, Springer Nature. d-ii) SEM of a fabricated silver-coated SPP microdisk. e-i) Schematic of dual microdisk resonators from Li et al. Adapted with permission.<sup>[232]</sup> Copyright 2016, IEEE. e-ii) Normalized transmission for dual microdisk obtained from theoretical equations. e-iii) Fabricated coupled dual microdisk resonator and the SEM image. f-i) PhCR from Sun et al. Adapted with permission.<sup>[239]</sup> Copyright 2020, Optica Publishing Group. f-ii) Microscope image of the PhCR. c-iii) Zoom-in microscope image of the PhCR. g) 2D PhC-based nano-ring resonator with three defects from Hsiao et al. Adapted with permission.<sup>[240]</sup> Copyright 2010, IEEE.

size at the subwavelength scale.<sup>[129,153]</sup> Figure 3g-i shows a bi-gradient on-chip metalens taper, which can be used as the taper in the coupler with high mode conversion efficiency. The size of the on-chip metalens can be significantly reduced by applying a Fresnel design. This design leads to a larger phase gradient, enabling subwavelength-scale ultrasmall focal lengths and spot sizes, which results in more efficient light focusing on the chip. The SEM image of the fabricated on-chip metalens is shown in Figure 3g-ii. The integration of on-chip metalenses for mode conversion and beam steering provides a new level of flexibility in compact on-chip light manipulation, with the aid of subwavelength structures.

In conclusion, the field of silicon photonic coupling has contributed to integrated optics. In recent years, researchers have approached this topic with great passion and excitement, yielding a large body of research results and solutions. Their efforts have been driven by four key factors: i) polarization-related losses and coupling efficiency, ii) bandwidth, iii) footprints, and iv) the capability for CMOS-compatible fabrication and practical packaging. Significant attention is currently being directed toward identifying design and fabrication processes for high-efficiency optical couplers that can be made using standard materials and processes commonly used in CMOS production. From an industrial perspective, factors such as material cost, assembly time, chip-to-chip variation, durability, and connection resilience also play a crucial role in determining the coupling and packaging strategy. However, to reach mass markets, strategies for wafer-level testing and packaging will need to be developed. There is still much work to be done in the field of fiber-to-chip coupling.

#### 4. Photonic Resonator

Resonators play an important role in communication as they offer high selectivity, flexible operation, and a high level of compactness with the potential for low unit cost. Different communication technologies are responsible for different frequency ranges. Integrated micromechanical resonators have been extensively researched in the radio frequency range.<sup>[154–164]</sup> In 5G communication broadband, the dominant technology for radio frequency filters is MEMS-based bulk acoustic wave (BAW).<sup>[165,166]</sup> BAW resonators consist of a piezoelectric film placed between two metal electrodes, inducing an acoustic wave that propagates vertically along the bulk of the piezoelectric film and forms a standing wave between the electrodes. The piezoelectric film plays an important role in MEMS systems, such as optical attenuators,<sup>[167–171]</sup> scanning mirrors,<sup>[172–176]</sup> and energy harvesters<sup>[177–186]</sup> and transducers.<sup>[187–190]</sup> To increase communication frequency to the terahertz range, small-scale integrated photonic resonators have been studied and demonstrated, driving exploration at both the signal transmitter and receiver sides. In various applications, specific frequencies or electrical responses are required, and several examples of typical geometries and materials will be presented.

##### 4.1. Photonic Crystal Resonator

Photonic bandgap materials and photonic crystals (PhCs) emerges in the late 1980s. Designing optical materials with periodic structures at the scale of wavelengths has proven to be an

effective method for manipulating the energies and fluxes of photons within these materials.<sup>[191–193]</sup> The refractive index changes periodically in PhCs, which conforms to the requirements of photonic bandgap (PBG).<sup>[156,159,161,194–197]</sup> Two different types of such structures exist in PhCs: one composed of isolated dielectric cylinders, and the other made up of air pores drilled in a dielectric matrix. The light within the PBG frequency range cannot propagate in the PhCs structure. However, by introducing specific defects in the PhCs structure, the PBG is changed.<sup>[155,160]</sup> These defects alter the local electromagnetic field through modifications to the surface state of the holes, such as changes to the refractive index, pattern size, pattern displacement, or by insertion of a different pattern. With the help of defects, microcavity or nanocavity-based PhCs resonators are demonstrated as photonic resonators in terms of resonant wavelength. The potential applications of PhCs to etalon,<sup>[198]</sup> microwave,<sup>[199]</sup> THz devices,<sup>[200]</sup> antennas,<sup>[201]</sup> sensors,<sup>[202,203]</sup> and mirrors<sup>[204]</sup> have been reported.

A Bragg grating is one kind of photonic crystal resonator that reflect a specific wavelength while transmitting all others. It has a grating structure that causes the refractive index to change periodically along the waveguide direction, creating a reflection interface for light propagation as shown in Figure 4a-i. The reflected light at a specific wavelength will propagate in the opposite direction. The specific reflected wavelength must satisfy the phase-matching condition of the coupled mode of the Bragg grating. The resonance wavelength and bandwidth are the two main parameters of a Bragg grating. One of the main motivations for using Bragg grating devices in integrated photonic circuits is their flexibility and high fabrication tolerance.

A Bragg grating is integrated into a compact SOI ridge waveguide, as shown in Figure 4a-ii.<sup>[205]</sup> The gratings are achieved through etching parts of the ridge or the slab. Figure 4a-iii displays a measured spectral response for the ridge waveguide gratings, which shows only one peak in the transmission spectrum over a wide wavelength range of 150 nm.

Several challenges remain in integrated grating structures. The small size of integrated grating structures can lead to waveguide nonuniformity due to poor fabrication accuracy, which often causes large fluctuations in the optical spectral responses. This can particularly affect applications that demand high uniformity in the passband. Additionally, imperfections in the grating realization may cause interference effects and result in group delay ripples. These ripples are a major limitation for applications that require time delay in fiber or integrated Bragg gratings.

Among all kinds of PBG structures, the photonic nanobeam waveguide is the simplest structure to be fabricated.<sup>[194,206–209]</sup> The first photonic nanobeam waveguide was demonstrated in 1997 by simply introducing a defect into a nanobeam that changes the bandgap of the photonic nanobeam.<sup>[210]</sup> A proper bandgap is important for nanobeams to choose wavelength. To trim the bandgaps of the aperiodic PhC nanobeams, a widely known method is changing the hole size.

Multiple resonances are also desirable for a single nanobeam. Conventional methods of achieving multimode nanocavities involve extending the cavity length. The fundamental mode is confined to the center, and the higher-order modes distribution is shifted, resulting in limited field overlap between different modes. Another solution is utilizing both dielectric and air modes in a tapered nanocavity. However, the overlap between

these two modes is also limited, since dielectric modes are mainly focused in dielectric regions, and air modes are mainly focused in air regions. The multiple mode-matched resonances can be solved using nonperiodic PhC nanobeams.<sup>[211,212]</sup>

The design of aperiodic PhC nanobeam structures which consists of two discrete adjustable components is investigated.<sup>[213]</sup> Figure 4b-i shows the images of samples with different shift factors(SF), where one way to increase bandgaps of aperiodic PhC nanobeams by varying the SF of the hole arrays is shown. Figure 4b-ii shows the measurement transmission of such nanobeams. Besides, the  $Q$  factor of this aperiodic PhC nanobeam is relatively low due to the strong scattering of photons at the interfaces with the abrupt refractive index changes. To enhance the  $Q$  factor and suppress light scattering, the gradual change of the filling factor of holes in photonic crystal reflectors is commonly used.

#### 4.2. Ring and Disk Resonator

One of the first single-ring resonators with integrated throughput and drop-out is presented in Haavisto and Pajer.<sup>[214]</sup> The waveguide is fabricated by a thin film of PMMA. The single-ring resonator is composed of a ring waveguide and two straight channel waveguides that are tangential to the ring with a designed distance. When light from the bus waveguide enters, it excites the circular resonant mode of the ring waveguide, causing light at the resonant wavelength to couple into the drop waveguide. As a result, the output spectrum of the drop port reveals a resonant peak.

In order to integrate more devices in the chip, the footprint of the ring resonator should be as small as possible, while  $Q$  value should still be high enough. Improvement in fabrication technologies and new material has made it possible to fabricate ring resonators with smaller radii. Hence, various material platforms have been studied to create a comprehensive collection for different wavelengths. These include SOI, organic crystals,<sup>[215,216]</sup> silicon-on-silicon nitride,<sup>[217]</sup> silicon-on-sapphire,<sup>[218]</sup> germanium-on-insulator,<sup>[219]</sup> silicon-on-lithium-niobate ( $\text{LiNbO}_3$ ),<sup>[220]</sup> germanium-on-silicon (GOS),<sup>[221]</sup> germanium-on-silicon nitride,<sup>[222]</sup> silicon–germanium alloy ( $\text{SiGe}$ )-on-silicon (SGOS),<sup>[223]</sup> and aluminum nitride (AlN)-on-insulator (AlNOI).<sup>[224–227]</sup> Among these platforms, AlN is a CMOS-compatible material with a large bandgap of 6.2 eV. Additionally, AlN also exhibits high thermal conductivity which is crucial for high-power and high-frequency applications, as well as low loss and high breakdown field strength, making it an attractive material for a wide range of electronic and photonic applications.<sup>[226,228]</sup> The use of AlN in these areas has gained significant interest in recent years, leading to its integration into a variety of devices, including high-frequency transistors, acoustic filters, and resonators, among others. The schematics and SEM images of the single-ring resonator on the AlNOI platform are presented in Figure 4c-i,ii.<sup>[229]</sup> A FSR of 19.3 nm is observed as shown in Figure 4a-iii for a ring resonator. Figure 4c-iv shows the zoom-in peak at 3.682  $\mu\text{m}$ . These measure results show that the AlN ring resonator enables high-quality application in MIR.

The disk resonator is a unique variant of the ring resonator with a zero inner radius. The mode size in the adjacent wave-

uide needs to match the whispering gallery-mode width propagating in the disk. The fabrication technology for microdisk resonators is like that for microring resonators and the materials used can be silicon, silica, or organic single crystals.<sup>[230]</sup> Compared to the microring resonator, the disk resonator has potentially lower scattering loss because no sidewall on the inner side.

The plasmonic microdisk can achieve a high-quality factor  $Q$  by coating a layer of noble metal on its surface, which excites surface plasmon polaritons (SPP) at the interfaces between metal and dielectric materials as shown in Figure 4d-i.<sup>[231]</sup> With this design, whispering-gallery modes in the near-infrared can achieve  $Q$  factors of over  $6 \times 10^7$  at room temperature, thanks to the combination of a silicon dioxide microcavity disk and a thin layer of metal. A scanning electron micrograph of a silver-coated microdisk resonator is shown in Figure 4d-ii. The significance of phase-matching between the cavity and fiber eigenmodes is evident in the transmission spectra.

Autler-Townes splitting (ATS) effect is also one effect that can be invested in a cascaded optical microdisk as shown in Figure 4e-i.<sup>[232,233]</sup> When the two resonance photons interact coherently, they create a transparent region in the photonic absorption or transmission spectrum. The normalized transmission plot is also shown in Figure 4e-ii, where the ATS spectrum is not shown. ATS is the splitting of energy levels caused by the interaction between the optical field and the resonant mode. The experiment involves using two coupled microdisk resonators, one of which is equipped with a microheater, to demonstrate efficient reconfiguration of the ATS mode through resonance detuning. A 3D schematic of the coupled dual disk resonator is shown in Figure 4e-iii. The fabrication process begins with patterning the surface of the SOI wafer with photonic structures, such as disks and waveguides, using deep-UV lithography and dry etching. The entire structure is then coated with a  $\text{SiO}_2$  cladding layer to achieve the critical coupling condition and meet fabrication requirements.

Combining the PhC nanobeam and ring resonator, the photonic crystal ring resonator (PhCR) has been investigated.<sup>[234]</sup> This kind of PhCR allows for high-quality mode confinement compared to a 1D PhC nanobeam waveguide. The schematic structure of the proposed PhCR is shown in Figure 4f-i. Circular holes with a periodic arrangement are incorporated into a normal ring. Figure 4f-ii shows the top-view microscope image of a fabricated device. To enable effective evanescent coupling between the bus waveguide and the PhCR resonator, the bus waveguide includes a circular section around the PhCR, covering a certain angle as shown in Figure 4f-iii. The resulting coupling region is a nearly uniform area with a gap. The pulley coupling scheme in PhCR resonator allows for a wider gap range to be fabricated, leading to better critical coupling and improved quality factor  $Q$ .

2D PhCs have shown the advantages of ultracompact size and high contrast of light. PhC filters are suitable basic units for PICs for their flexible structure and excellent performance.<sup>[235–237]</sup> 2D PhC-based microring resonators also have the advantages of 2D PhC and microring resonators, which have very well optical confinement and small footprint size. A PhC-based ring resonator of the hexagonal lattice was proposed by Hsiao and Lee as shown in Figure 4g.<sup>[238]</sup> Performance upon a scenario of a single-hole binding mechanism was explored. Owing to the well light confinement, the footprint size of a hexagonal microring resonator

is as small as possible. The PhC structure is made up of holes in the SOI platform. The microring resonator is created by removing specific holes along a hexagonal shape. The hexagonal microring resonator is surrounded by two PhC waveguides, which are produced by removing two rows of holes. The bending angle of the hexagonal ring resonator is smoother compared to ring resonators in a square lattice, thus reducing the impact of counterpropagating modes. By depositing different probe molecules within the holes, O1, O2, and O3, the output spectrums are different.

To summarize, with great progress in both theory and fabrication, photonic resonators played an important role in various fields. As communication bandwidth improves, the frequency of communication will continually increase. The growth of communication requires the development of high-quality resonators for filters and signal emitters. Photonic resonators are highly promising platforms for next-generation communication.

## 5. Waveguide-Based Physical Sensor

Photonic sensors can leverage advanced frequency metrology to provide cost-effective measurement solutions. Photonic physical sensors are robust against electromagnetic interference and drift compared to their electronic competitors, which are sensitive to environmental variables such as mechanical shock and electromagnetic interference, driving the data over time.<sup>[209,241,242]</sup> So, when affected by electromagnetic, electronic sensors require time-consuming calibration. These limitations of electronic sensors raised lots of interest in photonic sensors. Photonic physical sensors are mainly based on refractive index changes, which are different from photonic chemical sensors. This section mainly focuses on waveguide-based physical sensors, as they provide cost-effective and robust measurement solutions.

### 5.1. Photothermal Sensor

For years, optical sensing has garnered significant attention. Among various optical sensing methods, multi-wavelength optical sensing is a crucial aspect that is widely used in optical imaging, spectroscopy, and bio/chemical research. A multi-wavelength optical sensing system has been developed.<sup>[243]</sup> It incorporates MXene into the Mach-Zehnder interferometer (MZI) structure, resulting in a high efficiency upon exposure to red light (690 nm) due to the efficient photothermal conversion of  $Ti_3C_2T_x$ . The system, shown in **Figure 5a-i**, is a wavelength-sensitive photothermal optical sensor. The sensing arm of the MZI has multiple bends to enhance light-matter interaction, as depicted in **Figure 5a-ii** in the schematic of the MMI structure. The proposed multi-wavelength optical sensor is built on the SOI platform. **Figure 5a-iii** shows the cross-section of the sensor.  $Ti_3C_2T_x$  MXene films are layered on the MZI structure, as depicted in **Figure 5a-iv**, with silicon oxide added between the films to minimize signal loss due to film absorption.

When the pumping light is activated, the  $Ti_3C_2T_x$  MXene films efficiently absorb it and produce heat. This causes the waveguide underneath the films to heat up, leading to a refractive index change due to the thermo-optic effect in silicon. The output

light power will change due to the phase difference caused by the asymmetrical structure and thermo-optic effect caused by MXene heating. The wide operating wavelength range of  $Ti_3C_2T_x$  MXene films allows the pumping wavelength of the proposed photothermal optical sensor to cover a broad range, from visible to near-infrared light, with the potential to extend even further into the short-wave infrared (SWIR) range. The strong spectral sensitivity of the PHOS makes it responsive to different wavelengths.

### 5.2. Pressure Sensor

The successful implementation of the transfer-and-bond method has led to the fabrication of a flexible photonic tactile sensor.<sup>[244]</sup> The transfer methods of photonic circuits are demonstrated in **Figure 5b-i** while retaining their optical performance. The fabrication process is depicted in **Figure 5b-ii**. In brief, photonic circuits in silicon are patterned using the traditional CMOS process. Then, the substrate undergoes chemical etching to undercut the silicon device layer, thus weakening the bonding force. A PDMS film is laminated onto the substrate and peeled off. Then the whole silicon photonic layer is lifted off and transferred on the flexible PDMS film. **Figure 5b-i** displays images of typical photonic circuits. The devices have single-mode silicon waveguides as long as 1 cm, with hardly noticeable deformations or dislocations in the transferred devices. When subjected to pressure, the output spectrum will change.

Optomechanical sensing, which is based on the connection between mechanical movements and optical resonances, has received significant attention for sensor applications due to its small size, high sensitivity, and immunity to electromagnetic interference.<sup>[250]</sup> An optomechanical pressure sensor that aims to offer a more compact design and highly sensitive acoustic signal detection at specific frequency points has been proposed, as shown in **Figure 5c-i**.<sup>[245]</sup> The device is fabricated on an SOI substrate, and a silicon cantilever beam is fabricated through etching processing. Optomechanical cantilever structures can provide an accurate pressure-to-deflection conversion. The input and output optical fibers are fixed to straight grooves arranged at opposite ends of the rib waveguide, as depicted in **Figure 5c-ii**, with their centers aligned with that of the waveguide at the desired position. The operation of the device is shown in **Figure 5c-iii**. Pressure causes the cantilever beam to deflect, altering the relative position and coupling condition between the waveguide and fibers, which affects the light transmission.

Besides cantilevers, the use of diaphragm structures in MEMS systems is widespread, and a new optomechanical pressure sensor that utilizes a ring resonator structure has been proposed to deliver a high-sensitivity, accurate linear output, compatibility with CMOS technology, and ease of integration as a reliable optical pressure sensor.<sup>[246]</sup> The optomechanical pressure sensor, depicted in **Figure 5d-i,ii**, is a reliable and high-sensitivity optical pressure sensor featuring linear output, compatibility with CMOS technology, and easy integration. The microring resonator is positioned in the center of the diaphragm, which deforms under applied pressure. The pressure sensor array system is shown in **Figure 5d-iii**, allowing measurement of the parameters of pressure waves due to differences in sensor radii. The radius of the microring resonator can vary due to the displacement caused by

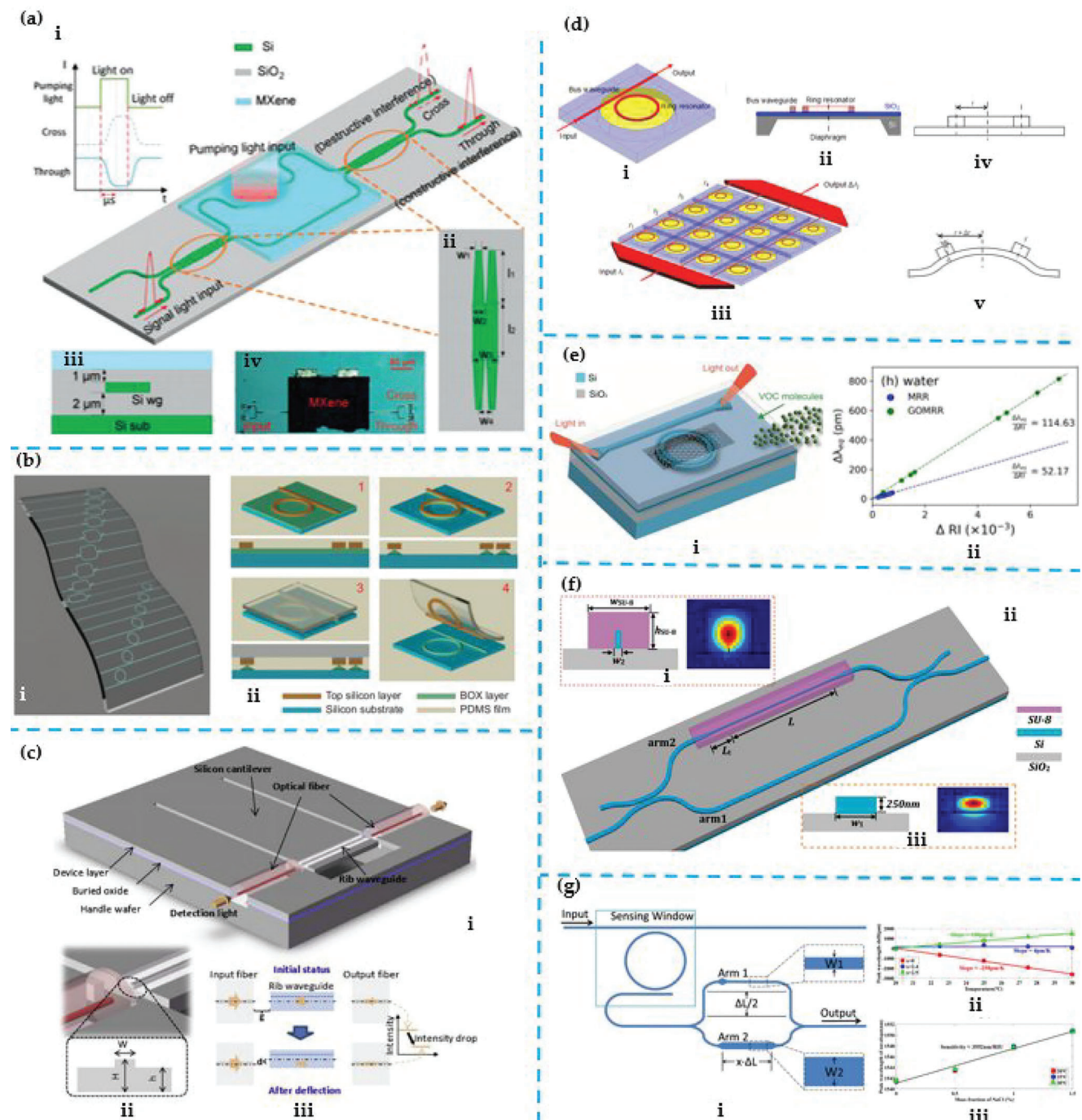


**Figure 5.** Waveguide-based physical sensor. a-i) Photothermal optical sensor from Zuo et al. Adapted with permission.<sup>[243]</sup> Copyright 2019, De Gruyter. a-ii) Details of MMI. a-iii) Cross-section of the proposed sensor. a-iv) Optical microscope image of the proposed sensor. b-i) Silicon photonic circuits on a flexible plastic substrate from Chen et al. Adapted with permission.<sup>[244]</sup> Copyright 2012, Springer Nature. b-ii) Fabrication procedures to transfer and bond silicon photonic circuits from a wafer substrate to a flexible PDMS substrate. c-i) An optomechanical pressure sensor from Li et al. Adapted with permission.<sup>[245]</sup> Copyright 2019, Elsevier. c-ii) A cross-section of rib waveguide and alignment fiber. c-iii) Working principle of the pressure sensor. d-i) The optomechanical pressure sensor from Zhao et al. Adapted with permission.<sup>[246]</sup> Copyright 2012, Optica Publishing Group. d-ii) Cross-section of the pressure sensor. d-iii) The 4 × 4 sensor array. d-iv) Illustration of the radius change before pressure is applied. e-i) Schematic of GO-coated MRR from Tsui et al. Adapted with permission.<sup>[247]</sup> Copyright 2020, Springer Nature. e-ii) Equilibrium resonance shift as a function of change in refractive index for water vapor. e-iii) Fitted peak wavelengths of the envelopes as a function of NaCl concentration. f-i) MZI-based temperature sensor with Si/SU-8 hybrid waveguides from Guan et al. Adapted with permission.<sup>[248]</sup> Copyright 2016, Optica Publishing Group. f-ii) The cross-section and the mode (power) distribution of the sensing arm. f-iii) The cross-section and the mode (power) distribution of the reference arm. g-i) Temperature-insensitive sensor from Zhang et al. g-ii) Fitted peak wavelengths of the envelopes as a function of temperature. g-iii) Peak wavelengths of the envelopes as a function of NaCl concentration. Adapted with permission.<sup>[249]</sup> Copyright 2019, Optica Publishing Group.

shear stress, as demonstrated in Figure 4d-iv,v. The change in radius resulting from the shear stress is the combination of both the deformation of the diaphragm and the relative movement of the microring resonator. The radius change caused by the shear stress can be primarily attributed to the deformation of the diaphragm, as the displacement of the ring resonator is made negligibly small. Thus, the pressure can be measured by monitoring the shift in the output spectra, which is a result of the shear stress induced on the diaphragm.

### 5.3. Humidity Sensor

In addition to light and pressure, monitoring and control of humidity are becoming increasingly crucial in environmental, medical, and industrial applications. The fundamental principle behind a waveguide-based humidity sensor is the change in refractive index.

The photonic waveguide can be coated by graphene oxide (GO) film, using a drop-casting technique. Although a single layer of graphene is non-porous, the stacking of graphene can form mesopores that exhibit exceptional water vapor adsorption due to capillary condensation. Both experiments and molecular dynamics simulations have confirmed the formation of multi-layer water in GO laminates through capillary condensation in the interlayer space.<sup>[247]</sup> The integration of graphene oxide into a silicon microring resonator (MRR) improves its sensitivity as a humidity sensor due to its molecular permeation properties, as shown in Figure 5e-i. Water molecules can penetrate easily between graphene oxide flakes, leading to a change in the film's refractive index and therefore a change in the output spectrum. Figure 5e-ii shows that compared to an MRR without graphene oxide coating, the graphene oxide-coated MRR has a wider range of refractive index changes for the same range of water vapor flow rates. This indicates that for certain vapor flow rates, the delivered vapor concentration to the graphene oxide-coated MRR can be significantly different from that of the uncoated MRR.

### 5.4. Temperature Sensor

Temperature is also one of the most important physical quantities in the world. Various optical structures, including Bragg gratings and MZIs, have been studied for building temperature sensors. Additionally, different materials, such as graphene and negative thermo-optic coefficient (TOC) materials, are being explored in the context of photonic temperature sensors.<sup>[251–255]</sup> The silicon has a large TOC ( $\approx 1.86 \times 10^{-4} \text{ }^{\circ}\text{C}^{-1}$ ) compare to silicon oxide. Therefore, silicon-based temperature photonic sensor is usually employed where requires precise temperature because of their high sensing solution at small temperature variations.

A silicon-based temperature sensor can enhance temperature sensitivity through an unbalanced MZI structure with hybrid waveguides, which is shown in Figure 5f-ii.<sup>[248]</sup> The negative-TOC material is used as the waveguide core in MZI-based temperature sensor as shown in Figure 5f-i. While the other reference arm still keeps the Si as the core as shown in Figure 5f-iii. Therefore, the temperature-dependent phase differential of the two arms is further strengthened.

A temperature-insensitive waveguide sensor based on SOI has been developed to minimize temperature effects.<sup>[249,256]</sup> The sensor, shown in Figure 5g-i, includes a microring resonator and an MZI. By adjusting the structure size of the MZI, the peak position of the cascaded transmission spectrum is made immune to temperature variation, and only sensitive to changes in the sensing area. The cladding of the ring has been etched to create a sensing window, making the tested solution close to the ring waveguide. Figure 5g-ii illustrates the peak wavelengths of the envelopes as a function of temperature. The transmission spectra were tested at various temperatures with varying concentrations of NaCl solution, as seen in Figure 5g-iii. The spectra exhibit a noticeable redshift as the concentration increases, while the sensor remains almost unaffected by temperature variations.

Besides silicon-based waveguides, organic photonic waveguides are also promising candidates for sensing technologies for their confinement geometry and light-scattering properties.<sup>[257]</sup> In 2023, Kumar et al. reports an amphibian-like organic optical waveguide made from blue-violet fluorescent crystal.<sup>[258]</sup> Such organic optical waveguides possess the remarkable ability to confine the light in both air and water while offering exceptional mechanical flexibility. This opens up exciting possibilities for manipulating optical signals with precision, particularly in micro-probe applications directed at specific sites.

In summary, the most promising and emerging physical sensing technologies based on silicon-based waveguides have been discussed. The fabrication and design integration of sensing systems on a single chip using various methods including optoelectronic integration techniques, and flexible photonic techniques also have been shown. To minimize the environmental disturbance, a cascaded configuration of the MZI-ring resonator system has been presented. There is an urgent need for the development of a simpler interrogation system to analyze the sensor output. The need for a broadband source and a photodetector to measure a broad range of wavelengths makes the use of this sensing challenging.

## 6. Waveguide-Based Bio/Chemical Sensor

The development of multi-functional, highly sensitive, and low-cost bio/chemical sensors is crucial in various industries, including agriculture, health, and environmental sciences, but is challenging due to the diversity of substances and reactions.<sup>[265–274]</sup> This requires a combination of advanced technology and knowledge in chemistry and material sciences. In response to the growing demand for such sensors, many optical chemical sensors have been developed in recent decades.<sup>[275,276]</sup> These sensors use lights of different wavelengths to analyze the sensors and typically consist of a wavelength-selectable light source, the sensor material that interacts with analytes, and a light detector. Using techniques like refractive index, absorbance, and Raman scattering can cover different regions of the spectrum.<sup>[277,278]</sup> By leveraging the properties of the light, such as the intensity, lifetime, polarization, and wavelength of light, bio/chemical information can be analyzed.

For waveguide-based sensors, the detection principle of most infrared bio/chemical sensors is based on evanescent field detection. The bio/chemical analytes interact influence the cladding refractive index and induce an additional optical absorption.<sup>[279]</sup>

Bio/chemical analytes disrupt the evanescent field and alter the cladding's refractive index, causing a shift in resonant peaks in photonic resonators (as seen in **Figure 6a-i**), and reducing light transmission intensity in waveguides (as seen in **Figure 6a-ii**).<sup>[259]</sup>

Optical ring resonators are also commonly used for refractive index-based bio/chemical sensors. To further increase the sensitivity, the Vernier effect is also used by using double-cascaded ring resonators.<sup>[260]</sup> The cladding SiO<sub>2</sub> opening is fabricated on the SOI platform as the sensing window. **Figure 6bi,ii** shows the schematics of two cascaded rings with microheaters. In this case, a PDMS made microfluidic channel is bonded to the photonic sensor.

To increase the alignment tolerance between the photonic sensors and the read-out unit, the back-side coupling interface system is illustrated in **Figure 6c-i**.<sup>[261]</sup> It includes a germanium-on-silicon waveguide covered with a mesoporous silica coating that is in contact with the water stream to be monitored. The back side microlens-based optical interface enables convenient and rapid chip replacement using the expanded beam concept. Additionally, the integration of lenses on the back side of the chip allows for cost-effective wafer-scale fabrication. The design of the grating structure is depicted in **Figure 6c-ii**. The fabrication process of the sensor chip is divided into three stages. First, the waveguides with grating couplers are created. Second, the micro-lenses on the back side are formed. Finally, a mesoporous enrichment coating is deposited as a top cladding on the Ge waveguide. To enhance the downward directionality, gold was deposited directly on top of the Ge grating.

The suspended sensor platform increases the interaction area while maintaining acceptable loss in light propagation. It offers an adjustable refractive index for the lateral cladding, resulting in suspended waveguides with lower refractive index contrast horizontally and higher contrast vertically. This improves light confinement vertically while providing a large lateral evanescent field, which enhances sensitivity. Additionally, the suspended design further boosts sensitivity and reaction time due to the larger interaction area beneath waveguides and improved gas flow mobility.

**Figure 6d-i** shows a proposed subwavelength-engineered suspended Si waveguide platform for gas sensing.<sup>[31]</sup> Two spiral waveguides are used to increase the sensitivity area without consuming the lateral area. Each spiral waveguide is covered by a separate chamber for gas feeding. The limit of detection (LoD) is primarily determined by the noise floor of the external read-out unit and has the potential to be improved to the level of several ppm. This platform offers sensitive and rapid detection, identification, and measurement of a specific analyte in a gas mixture without the need for additional adsorptive coatings, providing ample opportunities for use in environmental monitoring and clinical diagnosis.

The device is produced through one-step lithography on an SOI wafer and dry etching of silicon, followed by wet etching to remove the beneath BOX layer. The inset in **Figure 6d-i** displays a cross-sectional image of the fabricated suspended waveguide captured by a SEM. **Figure 6d-ii** shows an optical microscope image of the spiral structure characterized in our experiment. **Figure 6d-iii** displays the zoom-in graph of the spiral sensing area. The analyte molecules are uniformly distributed around the waveguide at subwavelength cladding as well as upper/lower air cladding, lead-

ing to increased absorption through interaction with the guided light's evanescent field.<sup>[280]</sup>

However, many current waveguide-based analyte probes using evanescent fields have limited light-matter interaction strength, which restricts their usage in high-sensitivity scenarios. To further increase the sensitivity, one way is to confine more evanescent fields in air.<sup>[281]</sup> An all-dielectric metamaterial-assisted comb waveguide sensor is designed for enhanced sensitivity as shown in **Figure 6e-i**.<sup>[262]</sup> The waveguide is made using a CMOS-compatible process on a mature SOI platform. The high confinement of the optical field is achieved through the subwavelength grating metamaterial that creates a large discontinuity in the longitudinal electric field at periodic high-index-contrast Si/air interfaces and enables refractive index engineering. The waveguide operates in the long-wave infrared (6–14 μm) spectrum, which is rich in molecular absorption fingerprints but is currently underdeveloped due to absorption by bottom cladding materials in existing waveguide platforms. The BOX layer beneath the waveguide is locally removed to make the SOI suitable for long-wave infrared operation. The waveguide operates at deep-subwavelength levels and has a vertically confined mode distribution, resulting in low propagation loss over a wide wavelength range and immunity to fabrication errors. By optimizing the period and duty cycle of the waveguide, an external confinement factor of 113% with a low propagation loss of 4.7 dB cm<sup>-1</sup> is achieved.

The use of silicon oxide as substrate or cladding restricts the spectral range for silicon photonics. To maximize silicon's potential in integrated photonics, the transfer of silicon photonic devices to new substrates is pursued. This is demonstrated by integrating silicon photonic devices on calcium fluoride (CaF<sub>2</sub>) substrates for low-loss operation in the mid-infrared (MIR) band, as shown in **Figure 6f-i**.<sup>[32]</sup> The finished device on the CaF<sub>2</sub> substrate, as seen in **Figure 6f-ii**, is successfully fabricated using the transfer method.

A typical transmission spectrum from the platform was measured and is displayed in **Figure 6f-iii**. This figure shows that resonant peaks from two 60 μm radius microring resonators, which are nearly critically coupled to the same bus waveguide, are distinguishable. As depicted in **Figure 6f-iv**, the optical resonance exhibits an intrinsic *Q* of  $6.2 \times 10^4$ , which corresponds to a linear propagation loss of 3.8 dB cm<sup>-1</sup>.

The transfer technique provides numerous opportunities for integrating silicon photonics with new materials. Besides being suitable for mid-IR photonics, the method is also adaptable to integrating silicon photonics with other substrates that have mechanical, electrical, or optical properties different from silicon, thus granting unconventional functionalities to silicon photonic circuits.

In various sensing applications, mixture analysis is a critical component. Rather than relying on human-crafted features, machine learning utilizes its unique learning capability to identify key features from the data set, building data-driven models.<sup>[282–286]</sup> In recent years, deep learning specifically has garnered much attention and transformed the field of data science.<sup>[287,288]</sup> The advancements in machine learning have broadened the scope of data-driven sensing applications. Machine learning has become a vital technique in device design, with researchers using it to optimize the design of metamaterial devices on demand. Sensors like microring resonators and

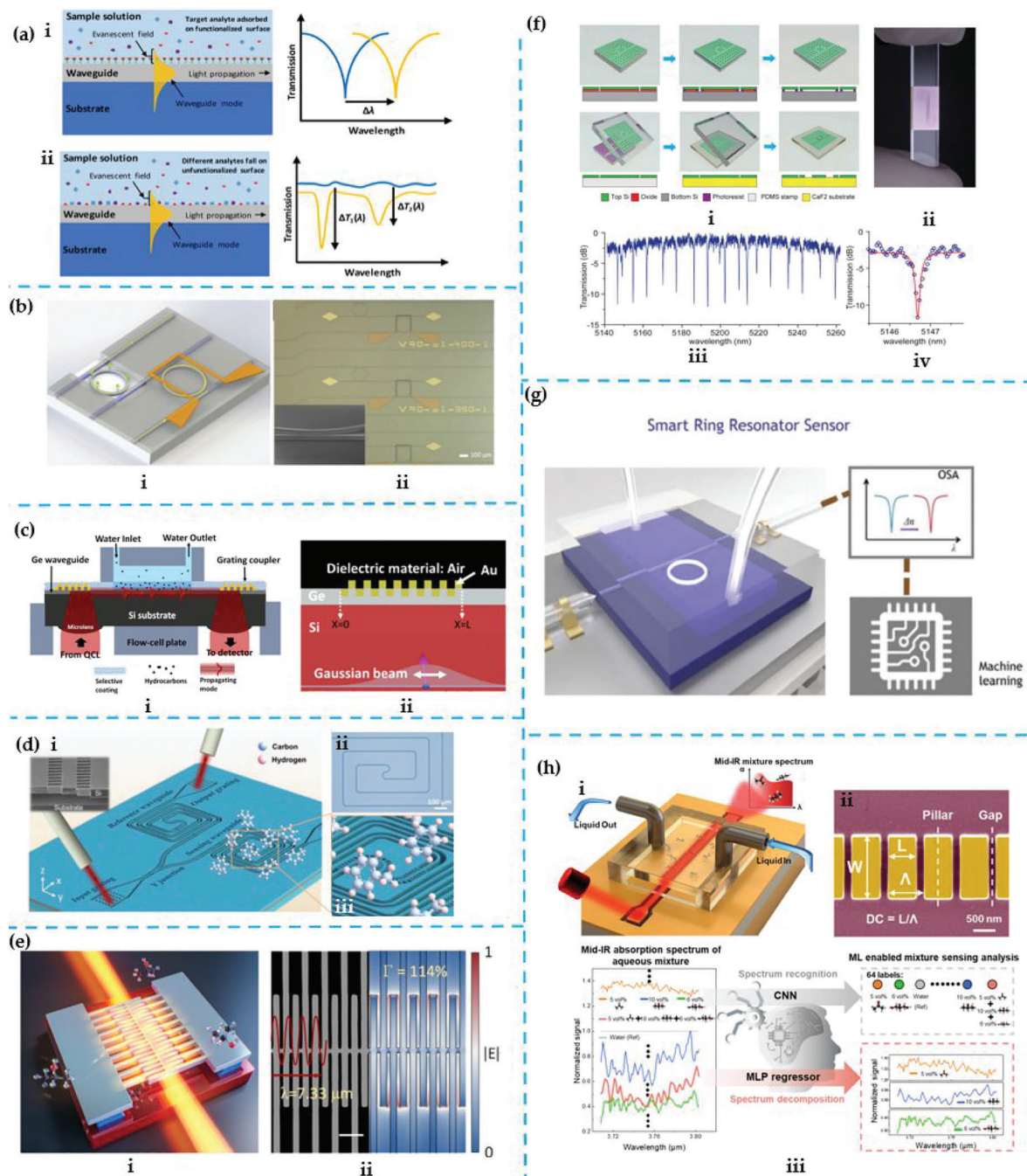


**Figure 6.** Waveguide-based bio/chemical sensor. a-i) Refractive index-based sensor with its surface functionalized to selectively adsorb analyte. The optical signal change in the sensor is known inducing by the absorbed analyte from Ma et al. Adapted with permission.<sup>[259]</sup> Copyright 2020, Springer Open. a-ii) Absorption-based sensor without surface functionalization. The different analytes adsorbed on the sensor surface are distinguished by their induced characteristic absorption peaks. b-i) Cascaded ring resonator for Vernier effect from Chang et al. Adapted with permission.<sup>[260]</sup> Copyright 2020, Optica Publishing Group. b-ii) SEM of cascaded ring resonator with oxide opening. c-i) Back-side coupling sensor with integrated micro-lenses from Beneitez et al. Adapted with permission.<sup>[261]</sup> Copyright 2020, Optica Publishing Group. c-ii) A cross-section of the back-side grating structure. d-i) Suspended waveguide sensor from Liu et al.<sup>[31]</sup> d-ii) Optical image of the suspended Si spiral waveguide. d-iii) Zoom-in view of the sensing waveguide. Adapted with permission.<sup>[31]</sup> Copyright 2021, De Gruyter e-i) Metamaterial-assisted comb waveguide sensor from Liu et al. Adapted with permission.<sup>[262]</sup> Copyright 2022, American Chemical Society. e-ii) Top-view SEM image of metamaterial-assisted comb waveguide sensor. f-i) Transfer process from Chen et al. Adapted with permission<sup>[32]</sup> Copyright 2014, American Chemical Society. f-ii) Image of finished silicon photonic devices on a CaF<sub>2</sub> substrate. f-i,ii) Measured transmission spectrum. f-iv) Zoom-in of the resonance. g-i) Smart ring resonator from Li et al. Adapted with permission.<sup>[263]</sup> Copyright 2021, Optica Publishing Group. g-ii) Data library building. g-iii) Transformation of spectra to matrices. g-iv) Neural network training with matrices. g-v) Composition prediction. h-i) Al-enhanced metamaterial sensor from Zhou et al. h-ii) Design of subwavelength waveguide grating. h-iii) Machine learning for CNN and MLP regressor. Adapted with permission.<sup>[264]</sup> Copyright 2022, American Chemical Society.

surface plasmonic sensors have seen improvements in selectivity through the use of machine learning. The technique has also been used to boost the performance of low-cost and mobile plasmonic sensing platforms, reducing inter-device variability in gas sensor applications.

A ring resonator-based smart sensor enabled by machine learning is demonstrated for the analysis of multiple chemicals, as illustrated in Figure 6g.<sup>[263]</sup> The sensor combines a ring resonator and a PDMS microfluidic network.<sup>[289]</sup> The smart sensor features a single label-free ring resonator for the analysis of multiple components in a mixture, instead of using multiple labeled ring resonators. First, different bio/mechanic mixtures are rinsed in the resonator chip to build the data library. Then, the resonant spectrum of the mixture is analyzed using a machine learning model based on an artificial neural network, which is trained to separate the spectrum into spectra of individual components. This allows for target identification and quantification using not just the resonant peak shift, but also extracting features from the entire spectrum. After being trained, the smart sensor accurately quantified three kinds of chemicals at varying ratios with low root-mean-squared error. This simplification of the ring resonator-based platform for chemical analysis shows a high level of accuracy. Despite it being a simple model system for demonstration purposes, it holds great promise for analyzing complex samples in photonic nanodevices.

For MIR sensing, the use of machine learning can minimize the impact of the strong water absorption for waveguide liquid sensors, enabling more accurate analysis of complex liquid mixture components. Figure 6h-i demonstrates an AI-powered metamaterial waveguide sensing platform for analyzing aqueous mixtures in the MIR.<sup>[264]</sup> The waveguide geometry, as shown in Figure 6h-ii, is carefully designed on the SOI platform, utilizing subwavelength grating metamaterials to enhance the sensitivity of the waveguide sensor in a compact footprint. A PDMS microfluidic channel is then bonded to the chip surface and defines the sensing area. By using a convolutional neural network (CNN) and a multilayer perceptron (MLP) regressor, a machine learning-based sensor can perform two tasks: spectral recognition and decomposition of ternary mixtures in a water solution, as demonstrated in Figure 6h-iii. The CNN is trained to identify the absorption spectra of mixtures with 64 predefined ratios, resulting in a high classification accuracy. Additionally, the sensor can differentiate the spectra of four solutions. The AI-enhanced metamaterial waveguide sensor demonstrates its potential for mixture recognition and quantification through the use of machine learning. This AI-enhanced waveguide sensor offers a cost-efficient and powerful solution for MIR spectrometry and holds promise for the development of a MIR spectrometer-on-a-chip.

This section reviews the recent advancements in infrared waveguide-based nanophotonics as a promising technology for various bio/chemical sensing applications. Optical detection offers advantages such as high sensitivity, low detection limit, low interference, strong multiplexing capabilities, and resilience to electromagnetic interference, making it preferable over other detection methods. Waveguide-based nanophotonics technologies also offer the potential for on-chip integration, making it a promising alternative to conventional optical sensors based on fibers or free-space resonators.

## 7. On-Chip Photodetector

The photodetector (PD) is a crucial component in optoelectronic links, as it converts optical signals into electrical signals in real time. With the trend towards miniaturization and integration, PDs are now being combined with waveguides to create compact photonic systems that can perform spectroscopic sensing with multiplexing/demultiplexing functions. This section will delve into the recent progress made in on-chip photodetectors that span the ultraviolet to MIR spectrum, covering a range of materials including perovskites, germanium, III-V semiconductors, and 2D materials.

For short wavelength light from ultraviolet to visible, the metal halide perovskites have gained much attention due to their exceptional optoelectronic properties, such as long charge carrier diffusion lengths and lifetimes, high optical absorption coefficients, tunable direct bandgaps, low trap density, high charge carrier mobility, and high external quantum efficiency in comparison to silicon.<sup>[290–292]</sup> To improve light harvesting and charge transport capabilities in the ultraviolet to the visible light range, a porous and interface-fused perovskite film photodetector has been introduced, as depicted in Figure 7a-i.<sup>[293]</sup> The Mie porous structure enhances the light-harvesting ability of the films thanks to its strong Mie scattering capabilities, especially for films with large pore sizes. Furthermore, the strong ionicity of the interface between the perovskite nanocrystals leads to their fusion during recrystallization, which promotes carrier transport. Additionally, the high work function of the metal used for contact, Au, leads to good ohmic contact between the semiconductor and metal. Furthermore, Figure 7a-ii displays the responsivity ( $R_i$ ) of the photodetector across ultraviolet to visible light (540 nm). The response speed was about 700 Hz at 532 nm. The voltage-dependent photoresponse was studied by adding different biases and using a silicon photodetector as a reference. The results are significantly higher, over one order of magnitude than those of commercial GaN or SiC photodetectors.

However, the use of photolithography in processing metal halide perovskites is not possible as water and acetone, which are necessary reagents in photolithography, would cause the perovskites to deteriorate. The compatibility of halide perovskite materials with semiconductor technology is achieved using parylene, a type of polymer.<sup>[294]</sup>

Silicon-based PDs are commonly used in the visible spectrum, but they cannot work for detecting infrared whose wavelength is above 1.1  $\mu\text{m}$  because of its indirect bandgap (1.12 eV). The energy of photons in telecom wavelengths (0.78–0.95 eV) is not enough to surpass the indirect bandgap of silicon, which prevents the generation of electron-hole pairs. The development of PDs for telecom wavelengths (1.4–1.6  $\mu\text{m}$ ) using established CMOS technology is a crucial step toward the integration of photonics and electronics on a single chip.

An effective solution to extend the wavelength range of on-chip PDs to the NIR region is integrating III-V semiconductors onto the Si chip using wafer bonding techniques and incorporating Ge (with a bandgap of 0.67 eV) with Si.<sup>[295]</sup>

The InGaAs PIN PD integrated on an SOI waveguide has been demonstrated with good performance.<sup>[296]</sup> The photodetector is made possible through the use of an evanescent coupling scheme, which can couple light from the waveguide to the

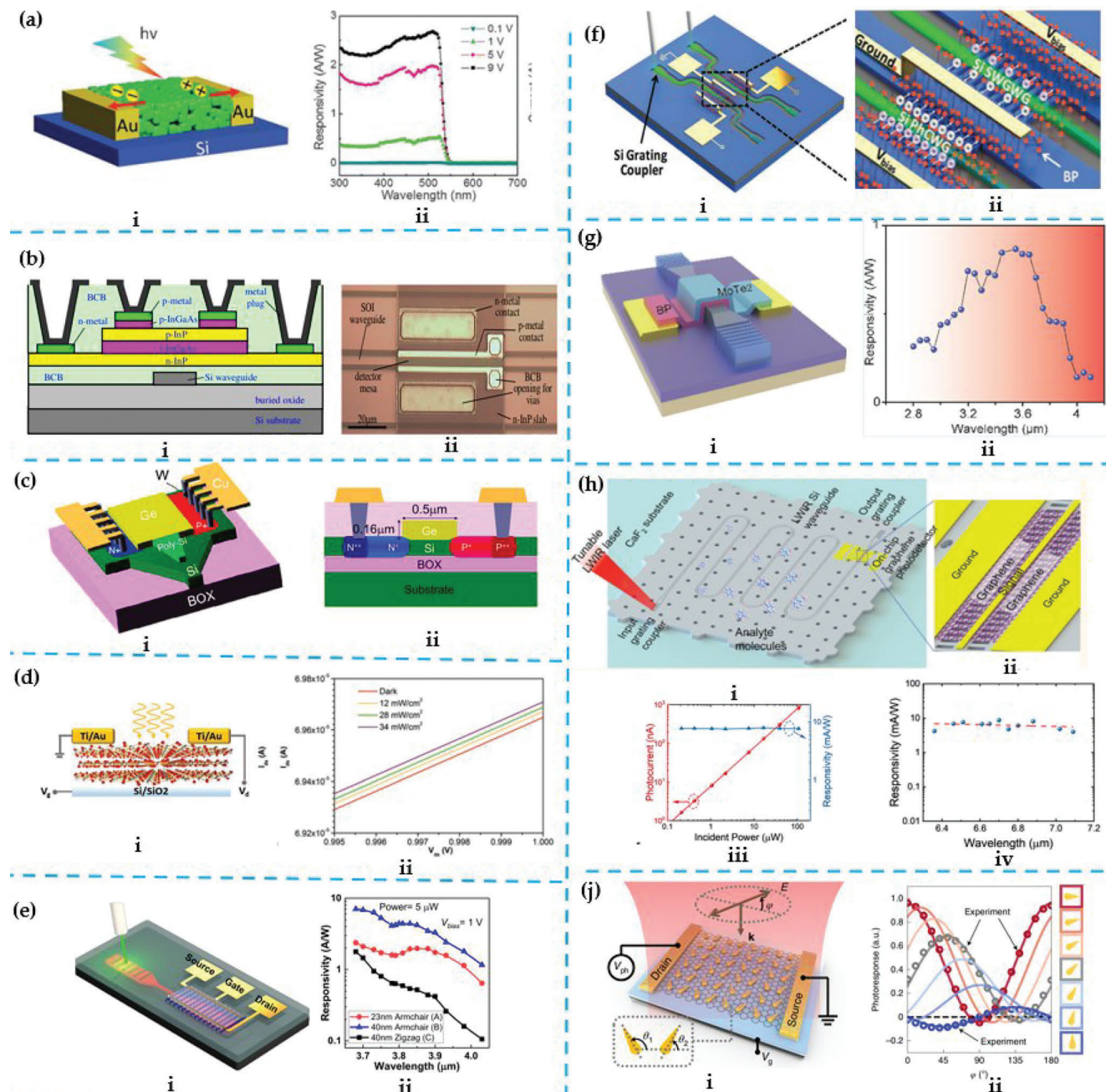


**Figure 7.** On-chip photodetectors. a-i) Photodetector based on the MIE porous and perovskite film from Xue et al. Adapted with permission.<sup>[293]</sup> Copyright 2017, Wiley-VCH. a-ii) Responsivity spectra of Mie porous PDs under different biases. b-i) Cross-section of an InGaAs PIN photodetector integrated with an SOI waveguide from Sheng et al. Adapted with permission.<sup>[296]</sup> Copyright 2016, Optica Publishing Group. b-ii) Top view of a fabricated device. c-i) Germanium waveguide p-i-n photodetector from Chen et al. Adapted with permission.<sup>[298]</sup> Copyright 2010, Optica Publishing Group. c-ii) Cross-section of germanium waveguide p-i-n photodetector. d-i) PdSe<sub>2</sub>-based photodetector from Liang et al. Adapted with permission.<sup>[300]</sup> Copyright 2019, Wiley-VCH. d-ii) The photoresponsivity on 4.05  $\mu$ m light as a function of gate bias. e-i) Black phosphorous-based photodetector from Huang et al. Adapted with permission.<sup>[301]</sup> Copyright 2018, American Chemical Society. e-ii) Spectral responsivity of devices. f-i) Configuration of the proposed shared-BP photonic system that consists of a PhC waveguide and a subwavelength grating waveguide from Ma et al. Adapted with permission.<sup>[302]</sup> Copyright 2018, Wiley-VCH. f-ii) Zoom-in view of the two BP photodetectors. g-i) BP/MoTe<sub>2</sub> heterostructures photodetector from Chen et al. Adapted with permission.<sup>[303]</sup> Copyright 2022, American Chemical Society. g-ii) Spectral-dependent responsivity of the BP/MoTe<sub>2</sub> heterostructures photodetector. h-i) Graphene/silicon/halide waveguide from Ma et al. Adapted with permission.<sup>[304]</sup> Copyright 2021, American Chemical Society. h-ii) Zoom-in view of graphene/silicon/halide waveguide. h-iii) Photocurrent and responsivity as a function of incident power. h-iv) Spectral responsivity of graphene/silicon/halide waveguide from Wei et al. i-i) Nanoantenna-mediated semimetal photodetector. j-ii) Measured photoresponse of nanoantennas with  $\theta$ . Adapted with permission.<sup>[305]</sup> Copyright 2022, Springer Nature.

InGaAs PIN PD via a very thin bonding layer (less than 200 nm).<sup>[297]</sup> This allows for a thin absorption layer (100 nm) and a short device length (40  $\mu\text{m}$ ) due to the phase-matching condition. Figure 7b-i illustrates the cross-section of such a PD. The top view of a fabricated device before the final metallization for plugs and pads is shown in Figure 7b-ii.

A germanium waveguide p-i-n PD is also a critical building block.<sup>[298]</sup> To minimize the transit time of the Si PD, a thin germanium layer is adopted. This PD shows a 3-dB optoelectrical bandwidth of  $\approx$ 67 GHz. A Si waveguide taper, along with a thick poly-Si taper, is utilized to couple light from the single-mode Si waveguide to the germanium-on-SOI waveguide, as shown in Figure 7c-i. The germanium layer size and doping configuration in the Ge PD are shown in Figure 7c-ii. Due to their large bandwidth and CMOS compatibility, it makes the germanium PD a desirable option for optical interconnects in silicon photonics.

Although germanium p-i-n PDs have great performance in the telecom wavelengths, they demand advanced fabrication processes for III-V semiconductor devices. Besides, the significant lattice mismatch and thermal expansion coefficient differences between III-V materials and Si are major challenges for the heteroepitaxial growth process.<sup>[299]</sup> For example, there is a large lattice mismatch between Si ( $a_0 = 5.4310 \text{\AA}$ ) and most III-V compounds, i.e., GaAs (lattice constant,  $a_0 = 5.6533 \text{\AA}$ ), InP ( $a_0 = 5.8587 \text{\AA}$ ) and the 6.1  $\text{\AA}$  family, such as InAs ( $a_0 = 6.0584 \text{\AA}$ ), GaSb ( $a_0 = 6.0594 \text{\AA}$ ) and AlSb ( $a_0 = 6.1355 \text{\AA}$ ). Bridging the significant lattice mismatch between III-V compounds and Si is a major challenge in growing III-V materials on Si substrates. For example, the mismatch between GaAs and Si is 4.1%, while between InP and Si, it is 7.5%. The challenges posed by the lattice mismatch and varying thermal expansion coefficients in heterogeneous integration of III-V detectors on Si substrates can lead to a high density of defects, such as threading dislocations and micro-cracks, which severely impact device performance.

For MIR photodetection, 2D materials such as graphene have been proposed for MIR photodetection, which can void lattice mismatch problems.<sup>[306,307]</sup> Besides graphene, a transition metal dichalcogenide, PdSe<sub>2</sub>, has been proven a promising material for MIR sensing. With its unique pentagonal atomic structure, the bandgap of PdSe<sub>2</sub> is thickness dependent and can be manipulated from 0 eV for bulk to 1.3 eV for the monolayer.<sup>[308]</sup> This unique characteristic enables devices based on PdSe<sub>2</sub> with the possibility to detect from the visible and MIR regions. A PdSe<sub>2</sub>-based transistor was fabricated as depicted in Figure 7d-i.<sup>[300]</sup> A MIR light at 4.05  $\mu\text{m}$  was used to illuminate the transistor at room temperature. The flake has a thickness of about 50 nm. As shown in Figure 7d-ii, the source-drain current increases with the power density of the MIR laser. Notably, the PdSe<sub>2</sub>-based photodetectors exhibit high photoresponsivity across the visible, near-infrared, and mid-infrared regions.

Black phosphorus (BP) is also a promising material for PD with its superior narrow direct bandgap and layered lattice structure.<sup>[301]</sup> Figure 7e-i shows the schematics of the evanescent coupling scheme BP PD. The source and drain electrodes are placed directly on BP along the two sides of the output grating coupler and in proximity to the active light-BP interaction region for effective collection of photocarriers. The spectral response under a fixed power is measured. The spectral responsivity is consistent with the power dependence measurement as shown in

Figure 7e-ii. The responsivity is decreasing with increasing wavelength. Subband transition in BP causes a peak between 3.8 and 3.9  $\mu\text{m}$  from an increase in photon absorption.

Slow light stands out among other light-matter interaction-enhancing technologies for its easy realization. Slow light has extremely low group velocity, resulting in enhanced light-matter interaction.<sup>[309]</sup> The slow light effect can also be used to enhance the responsivity of BP PD. A comparison was made between identical BP PD on a slow light waveguide and a normal waveguide. Figure 7f-i schematically illustrates the proposed shared-BP PDs.<sup>[302]</sup> Specifically, at the BP PD shown in Figure 7f-ii, more light is absorbed, and consequently more electron-hole pairs are generated in the BP photonic crystal waveguide PD due to the inherent slow light effect, as compared with the subwavelength grating waveguide counterpart. The 3 dB bandwidth increases from 0.78 to 1.64 kHz as the incident power raises from 53.76 to 107.2  $\mu\text{W}$  which is due to the reduced free carrier concentration in the channel. The experiments reveal that the slow light effect does not worsen the noise or power dependence in the trap saturation region of the BP PD.

Besides single-layer 2D material PD, heterostructure 2D material PDs are also investigated.<sup>[310-312]</sup> Due to the van der Waals of BP, BP can be transferred onto other 2D materials to form a new class of heterostructure PD. Figure 7g-i shows a heterostructure 2D material PD.<sup>[303]</sup> This PD has vertically stacked BP/MoTe<sub>2</sub> heterostructures, which were integrated into the silicon waveguide via the traditional dry transfer technique. Figure 7g-ii demonstrates the spectral response of the PD with the excitation fixed power. The result shows that the device could exhibit a high photoresponsivity over a broad spectral bandwidth. The bandwidth of this PD is about 10 MHz. With the hybrid structure, the cutoff wavelength of the detector can extend up to 8  $\mu\text{m}$  by integrating the narrow-gap arsenic- or carbon-doped black phosphorus with silicon waveguides.

Several platforms have been developed to extend the cutoff wavelength into the long infrared range, such as suspended silicon, germanium-on-silicon, and silicon-germanium alloy-on-silicon, all offering low propagation losses. However, the suspended waveguides present challenges in subsequent processes and integration. While GOS and SGOS waveguides have demonstrated promise for long wavelength IR applications, the most accessible, cheap, and mature platform remains SOI with its transparency window extending up to 8  $\mu\text{m}$ . Hence, a transfer printing technique that transfers the Si device layer from SOI to CaF<sub>2</sub> with high efficiency is being explored to fully leverage the benefits of the SOI platform.

Meanwhile, semimetallic materials like graphene are suitable options for photodetection at longer wavelengths due to their gapless nature, providing high-speed photoresponse from ultraviolet to terahertz. However, a large dark current is generated when bias is applied, lowering the detection sensitivity. Hence, a zero-bias operation is preferred to minimize both dark current and power consumption.

Figure 7h-i displays a heterogeneously integrated long wavelength infrared PD on a graphene/Si/CaF<sub>2</sub> waveguide with zero power consumption in standby mode.<sup>[304]</sup> The high-yield fabrication of this PD is achieved through a simple transfer printing process using PDMS stamps. The structure of the long wavelength infrared heterogeneously integrated graphene/Si/CaF<sub>2</sub>

waveguide PD with zero standby power consumption is shown in Figure 7h-ii. The graphene membrane is transferred onto the waveguide and a 5 nm thick aluminum oxide layer is deposited to electrically separate the graphene and Si waveguide. The integration of the waveguide and plasmonic enhancement results in a high broadband responsivity of around  $8 \text{ mA W}^{-1}$  when the graphene photodetector operates under zero-bias conditions. The photocurrents as a function of incident power are depicted in Figure 7h-iii, and the device displays broadband photoresponse from 6.3 to 7.1  $\mu\text{m}$  as seen in Figure 7h-iv. The 3 dB bandwidth of this device is predicted to range from 10 to 500 GHz.

The significance of polarization is paramount in optics-related areas such as imaging, remote sensing, and navigation. Many photonic components are made to manipulate the polarization.<sup>[313,314]</sup> However, precise polarization evaluation is difficult and often requires bulky polarization optics. Recently, on-chip polarization-sensitive photodetectors have emerged as a viable option for polarization detection, making it possible to create advanced polarization cameras.<sup>[305]</sup> The illustration in Figure 7j-i showcases a nanoantenna-mediated few-layer graphene photodetector that offers configurable transitions between unipolar and bipolar polarization dependence. The device consists of periodically oriented metallic nanoantennas on a graphene transistor. By controlling the orientation angles of the nanoantennas ( $\theta_1, \theta_2$ ), the PRs of our device can vary from positive to negative values. The photoresponse of a single nanoantenna with different orientation angles is shown in Figure 7j-ii. The detectivity of polarization-angle perturbation for this device is  $0.02^\circ \text{ Hz}^{-1/2}$ . As a result, the photodetectors become polarization dependent, with a single antenna exhibiting varying photoresponse depending on its orientation angle.

In conclusion, for visible waveband PDs, the indirect bandgap semiconductor silicon has exhibited its irreplaceable position with a high maturity level of processing technology. III-V materials have excellent optoelectronic properties such as higher intrinsic carrier concentration and mobility. III-V semiconductor PDs are promising candidates for high-efficiency broad-spectrum on-chip detection with their 3 dB bandwidth at high frequency. 2D materials show potential for infrared photodetection at room temperature, but the growth and synthesis methods need further exploration to achieve large-scale production. To improve device quality, future efforts should focus on optimizing device design and fabrication techniques, while addressing issues such as low light absorption, dark current, and other noise sources.

## 8. On-Chip Modulator

Electro-optic modulators are an essential component for active function in photonic integrated circuits, which convert signals from the electrical to the optical domain. They are the basis of telecommunication, data center optical networks, and quantum information processing.<sup>[315]</sup> Large-scale integration and low fabrication cost requirements also come from emerging applications including optical spectroscopic sensing, LiDAR, and artificial neural network, promoting the rapid development of on-chip modulator.

Generally, by applying a voltage or current bias, the refractive index of the material may be changed. In general, the mainstream modulation principles can be further divided into

three major categories including 1) pure phase modulation, i.e., electro-refraction involving a change of the real part of the refractive index ( $\Delta n$ ) (Figure 8a), 2) concurrent modulation of the real and imaginary part of the refractive index ( $\Delta n$  and  $\Delta k$ ) (Figure 8e) and 3) intensity modulation via electro-absorption (Figure 8h) resulting from the change of the imaginary part ( $\Delta k$ ) or other schemes of optical attenuation. Essentially, pure phase modulation is often regarded as more challenging than intensity modulation. This is because phase modulation can be converted into intensity modulation either by forming constructive/destructive interference in a MZI, or including a resonant structure that allows shifts in resonance conditions induced by refractive index, whereas the reverse is not possible. The primary effects that are traditionally useful in state-of-the-art nonresonant modulators include the thermo-optic effect, free-carrier plasma dispersion effect, and Pockels effect (otherwise known as the linear electro-optic effect). In the past decade, with the development of advanced micro-/nanofabrication technology, MEMS have flourished as a new paradigm of on-chip modulator devices.<sup>[316,317]</sup> In this section, we describe the basic configuration of nonresonant modulators and their working principle.

### 8.1. Pure Phase Modulation

A sketch illustrating the general idea of pure phase modulation is presented in Figure 8a, where a perfect spectral shift is expected to occur. As a result of simple design, low cost, and large optical tunability, one of the most widely adopted methods of achieving pure phase modulation in silicon devices has relied on the thermo-optic effect by locally controlling the temperature in the phase-shifting region. Research efforts are mainly focused on improving the performance of thermo-optic phase shifters (TOPS). An effective way to improve TOPS is to reduce heat leakage to the environment, such as forming an air-gap trench or suspending devices with substrate undercut. To further improve the tuning efficiency, TOPS devices with geometrical design optimization using folded waveguides have been proposed to reduce power consumption as well as footprint,<sup>[318]</sup> as shown in Figure 8b-i. The TOPS consumes 2.56 mW for a  $\pi$  phase shift while featuring 1.23 dB optical loss, whose footprint is only 0.0023 mm<sup>2</sup>. In addition to the commonly adopted metal resistive heater, a TOPS with an integrated doped silicon heater has been demonstrated by Watts et al., as shown in Figure 8b-ii.<sup>[319]</sup>

Since silicon itself exhibits a negligible Pockels effect due to the centrosymmetric crystal structure, phase modulation can be implemented by building mature Si photonic devices on foreign materials with a strong Pockels effect. Lithium niobate (LiNbO<sub>3</sub>) is a promising material for optical modulators due to its strong Pockels effect which can operate at CMOS-compatible voltages.<sup>[320-323]</sup> To avoid the direct etching of LiNbO<sub>3</sub> itself, a heterogeneously integrated Si-on-LiNbO<sub>3</sub> hybrid modulator was proposed by Xu et al.<sup>[324]</sup> As shown in Figure 8c-i, its core concept is to leverage the electro-refractive modulation contributed from the portion of optical mode leaked into LiNbO<sub>3</sub> substrate. The key performance metrics, i.e., voltage length product  $V_\pi L$  of 12.3 V cm is obtained. Alternatively, as a family member in CMOS-compatible

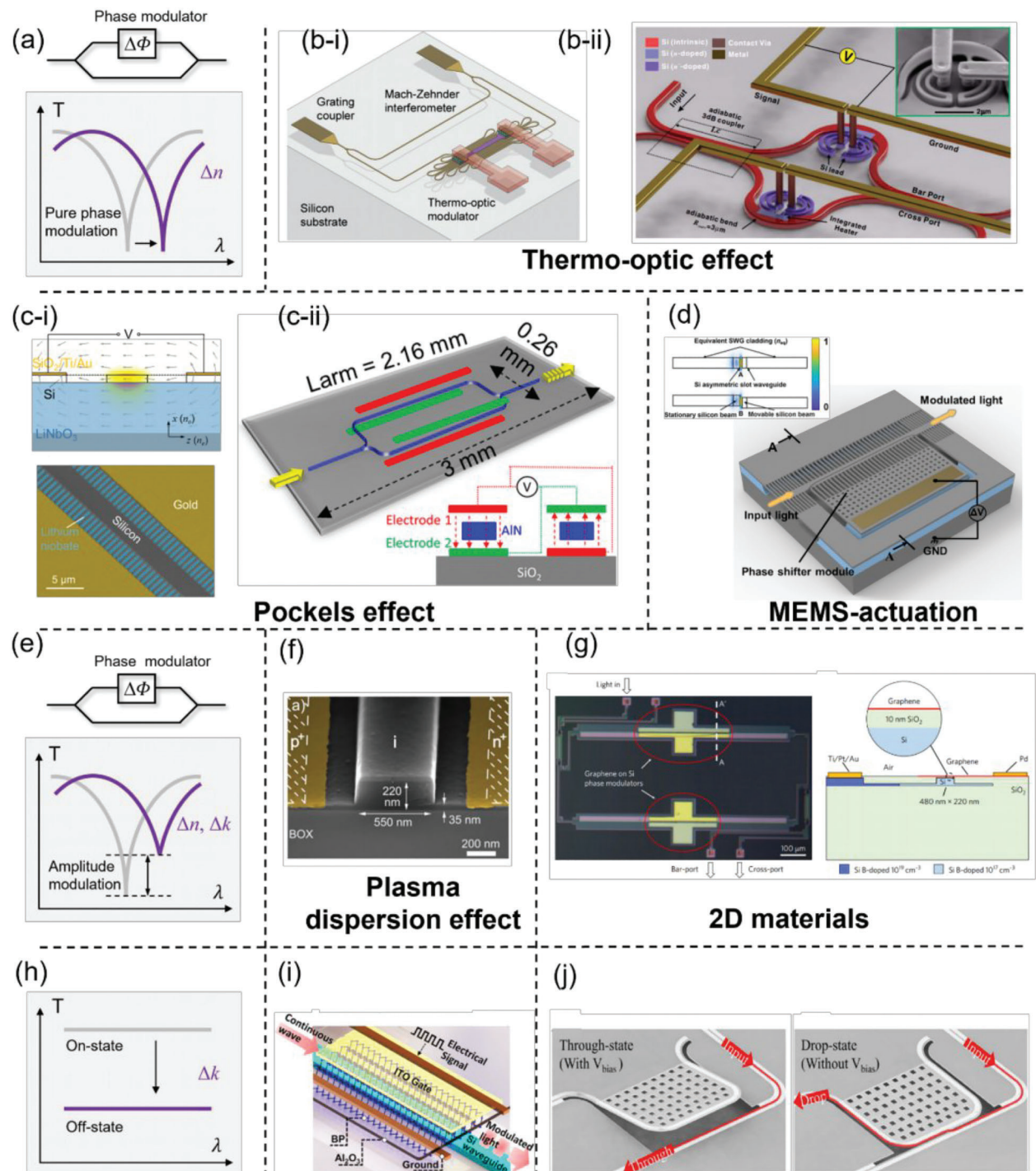


**Figure 8.** Nanophotonics modulator. a) Typical spectral shift in MZI where pure phase modulation is realized. b-i) TOPS with folded waveguide structures for tuning efficiency improvement. Adapted with permission.<sup>[318]</sup> Copyright 2019, Optica Publishing Group. b-ii) TOPS with integrated resistive silicon heater. Adapted with permission.<sup>[319]</sup> Copyright 2013, Optica Publishing Group. c-i) Si-on-LiNbO<sub>3</sub> hybrid EO modulator. Adapted with permission.<sup>[324]</sup> Copyright 2022, Wiley-VCH. c-ii) AlN EO modulator with parallel electrodes providing out-of-plane electric field. Adapted with permission.<sup>[326]</sup> Copyright 2020, American Chemical Society. d) MEMS phase shifter based on movable asymmetric slot waveguide. Adapted with permission.<sup>[329]</sup> Copyright 2022, Optica Publishing Group. e) Typical spectral as a result of concurrent modulation of the real and imaginary part of the refractive index. f) Free carrier injection modulator with p+/i/n+ configuration. Adapted with permission.<sup>[325]</sup> Copyright 2007, Optica Publishing Group. g) 2D materials integrated phase modulators based on graphene-insulator-silicon capacitor. Adapted with permission.<sup>[332]</sup> Copyright 2017, Springer Nature. h) Representative spectral change of intensity modulator. i) 2D materials-based intensity modulator using black phosphorus. Adapted with permission.<sup>[331]</sup> Copyright 2021, Elsevier. j) MEMS-actuated intensity modulator, switched between on/off state. Adapted with permission.<sup>[333]</sup> Copyright 2020, Optica Publishing Group.

materials, AlN possesses a satisfactory Pockels coefficient ( $r_{13}, r_{33} \approx 1 \text{ pm V}^{-1}$ ). Compared with LiNbO<sub>3</sub> which possesses a higher Pockels coefficient ( $r_{33} = 30 \text{ pm V}^{-1}$ ), the availability for chip-scale integration and CMOS compatibility of AlN compensate for its moderate EO coefficient. Wafer-scale AlN deposition technology has been widely studied. Following the pioneering work reported in 2012 utilizing simple co-planar electrode structures,<sup>[325]</sup> a more straightforward structure was demonstrated in which AlN is sandwiched between standard parallel metal electrodes.<sup>[326]</sup> As shown in Figure 8c-ii, the electrodes from different arms of MZI are connected using the push-pull configuration, doubling the effective tuning efficiency.

Furthermore, silicon photonics MEMS phase shifters have been also demonstrated on SOI.<sup>[327,328]</sup> Typically, for MEMS-actuation, a microstructure is placed in the vicinity of a waveguide, perturbing the evanescent field of the optical mode through tunable microstructures, e.g., nanobeam cantilevers or bridges. In addition, Sun et al. propose a phase shifter via modulating the confined optical mode through tunable slot waveguides as shown in Figure 8d. Like most MEMS phase shifters, its modulation speed of 10 kHz is mainly limited by the mechanical frequency of the actuator.<sup>[329]</sup>

## 8.2. Concurrent Modulation of Phase and Amplitude

As revealed by a typical spectral response in Figure 8e where spurious amplitude modulation occurs, electro-optic phase shifters based on free-carrier plasma dispersion effect usually suffer from considerable insertion loss, especially in the long wavelength range. The coupled modulation of phase and amplitude becomes a major restriction when proliferating them in a coherent photonic network in which adjustments of purely optical phase are required. Notably, compared with thermo-optic effect or Pockels effect, these devices relatively feature low half-wave voltage. Different schemes of electrical manipulation of the charge density include carrier injection, accumulation, or depletion. As shown in Figure 8f, common p-type/intrinsic/n-type diode structures were formed around the lossless intrinsic waveguide core to electrically control the carrier injection into the path of the propagating light.<sup>[325]</sup> With an ultra-compact modulation length of only 100–200  $\mu\text{m}$ , the device exhibits high modulation efficiency with  $V_{\pi}L$  of 0.036  $\text{V}_{\text{cm}}$ , being 100-fold smaller than Pockels counterparts.

In addition to above mentioned conventional configurations, some other types of phase shifters have also been proposed and used extensively. More recently, attempts have been made to investigate alternative modulation mechanisms in other materials potentially compatible with silicon photonic technology, such as 2D materials and phase change materials.<sup>[330]</sup> In particular, phase shifters based on graphene integrated on Si have been reported, in which phase change is realized in the form of a Si-insulator-graphene capacitor. By applying a bias to the capacitor, the charge is accumulated on the graphene electrode, shifting its Fermi level and thereby modifying its complex conductivity. In this way, both the effective index and optical loss of the waveguide are tuned simultaneously. A static modulation depth of 35 dB and modulation efficiency of 0.28  $\text{V}_{\text{cm}}$  have been demonstrated.

## 8.3. Intensity Modulation

Different from interferometer where light interferes constructively or destructively, amplitude modulation exploits the attenuation of the intensity of a propagating mode directly resulting from the absorption, or more generally, any perturbation that manipulates the intensity of the propagating light. In semiconductors, the electro-absorption effect could result from the distortion of energy bands caused by the applied electric field. Especially, Huang et al. integrated black phosphorus (BP) modulator on silicon waveguides to leverage the gating effect through a combination of the Burstein-Moss effect and Franz-Keldysh effect, as shown in Figure 8i.<sup>[331]</sup> The Franz-Keldysh effect is an electro-absorption phenomenon based on the principle of semiconductor bandgap decrease that occurs upon the external electric field, while the former suggests an increase in the absorption edge (optical band gap) as the Fermi level is possibly raised above the conduction band due to the filling of free electrons in the heavily doped cases. When different gate bias is applied to manipulate BP's optical properties through the gating effect, the propagating light in the Si waveguide interacts with BP and thereby its intensity is modulated. Additionally, MEMS-based movable waveguides or actuators have been exploited for optical attenuation. For example, in Figure 8j, MEMS cantilever can be actuated electrostatically to bend upwards, thereby eliminating the light coupling between input-port to drop-port, translating into switching the light between on- and off-state.

In many cases, the requirements for an optical modulator of high modulation speed, low losses, compact footprint, and low power consumption appear to be contradictory, and therefore application-specific engineering is necessary to achieve an optimal trade-off. On the one hand, further improving the performance of these individual components could move them closer to practical applications. On the other hand, future integrated EOMs may demand other functionality for emerging applications such as nonvolatile pure phase modulation. It is envisaged that the development of a new generation of integrated EOMs with unique functionalities.

## 9. Photonic Memory

Recent advances in various data-intensive applications, including AI, autonomous vehicles and high-performance computing, have posed unprecedented demands on the data processing capability and power management of current electronic integrated circuits. These systems, primarily based on the Von Neumann architecture, separate data, and processing, leading to high latency, slow data transfer rates, and significant energy costs.<sup>[338]</sup> To address this so-called Von Neumann bottleneck, researchers have explored in-memory/near-memory computing as an alternative approach.<sup>[339–341]</sup> This approach involves processing data within the memory itself or near the memory. Particularly, photonic integrated circuits, which deliver and process information in the optical domain with superior speed and bandwidth, would benefit greatly from the adoption of optically accessible photonic memories for data storage and retrieval without time-consuming and power-consuming electro-optical conversions. Similar to electronic technology, photonic memories can be classified as either volatile or non-volatile types. Volatile memories require sustained

power to retain their stored data, which in turn results in relatively fast operation speed. In contrast, non-volatile memories can retain the data even when the power is turned off, making them more energy-efficient and ideal for long-term data storage. This section will primarily focus on the rewritable mechanisms for nonvolatile photonic memory devices that can be integrated into the on-chip photonic computing architectures.

To date, different mechanisms or materials have been proposed to demonstrate non-volatile photonic memories and modulate light through light-matter interactions, including charge-trapping effects, phase transition materials, and ferroelectric materials.

In electronic integrated circuits, floating-gate technology is widely adopted for nonvolatile electronic storage such as flash, EPROM, and EEPROM memory.<sup>[342]</sup> The floating gate is insulated by dielectric materials so that electrons trapped in this gate are kept inside for a considerable period. Notably, the complex refractive index of the materials can also be modulated by electron doping and thus perturb the optical mode propagating through the effective region. Based on the hole accumulation in Si and the induced plasma dispersion, Barrios et al. first proposed floating gate-based photonic memory in a ring resonator configuration with an on-top hanging  $\text{Si}_3\text{N}_4$  floating gate.<sup>[343]</sup> This work predicted a modulation depth of 91% (10.4 dB) between the uncharged and charged ( $3.75 \times 10^{12} \text{ e cm}^{-2}$ ) states with a read time of only 9 ps. In 2016, Song et al. experimentally demonstrated Si-based programmable non-volatile memory, as presented in Figure 9a. It comprises an optical waveguide with a poly-Si floating gate, which is separated by a thin oxide layer.<sup>[344]</sup> Switching energy is measured as smaller than 20 pJ in a micro-ring resonator. The multi-level and four-bit memory read capacity is also demonstrated with a micro-ring resonator array. Nevertheless, this poly-Si-based photonic memory only can impose a slight effective index variation due to the small spatial overlap and the relatively weak free-carrier dispersion effect. To solve this problem, novel 2D materials-based floating gates, both in monolithic and heterogeneous configurations, have recently been explored as optical memory.<sup>[345–347]</sup> For example, the graphene floating gate theoretically only requires a small number of trapped charges to achieve sufficient effective index tuning, hence, reducing its bias voltage and operation power. Figure 9b shows the waveguide-based photonic memory by leveraging graphene as both the back gate (BG) and the floating gate (FG).<sup>[344]</sup> At the programming state (negative  $V_D$  and  $V_G$ ), the tunneling current density from drain to FG is much larger than that from FG to source due to the barrier height difference. That is, electrons could successfully tunnel into FG from the drain with negligible flowing out to the source. At the erasing state (positive  $V_D$  and  $V_G$ ), the tunneling current density from FG to drain becomes much larger than that from source to FG because of barrier alternation, thus erasing the electrons stored in FG.

Another promising approach for developing photonic memory is using phase change materials (PCMs), which can exhibit two distinct states with different electrical conductivity and optical transparency. Currently, transition metal oxides (TMOs) and chalcogenides-based PCMs have been extensively explored for nonvolatile photonic applications. TMOs are compounds of oxygen atoms bound to transition metals, which have enabled revolutionary applications such as resistance random access mem-

ory (ReRAM) and high-performance supercapacitors.<sup>[348,349]</sup> Recently, vanadium dioxide, an archetypal TMO, has shown interesting optical properties due to its sensitive metal-insulator transition (MIT) near room temperature.<sup>[350,351]</sup> Its optical switching ability during MIT makes it a promising choice for high-speed reversible optical modulators,<sup>[352]</sup> and its bistable hysteresis states provide potential memory function in optical modulation. As presented in Figure 9c, Jung et al. demonstrated a compact hybrid  $\text{VO}_2$ -Si optical memory element integrated into a Si waveguide, which can be optically written with energy as low as 23.5 pJ per pulse and with a 10–90% rise time of  $\approx 100$  ns.<sup>[353]</sup> It is worth noting that the  $\text{VO}_2$  optical memory shown in this work is volatile, as the temperature-induced phase transition in  $\text{VO}_2$  is typically reversible and returns to the insulating state from the metallic state when the temperature cooled down below the transition point. Therefore, other switching mechanisms, such as electric field tuning,<sup>[354]</sup> ionic gating,<sup>[355]</sup> and mechanical straining,<sup>[356]</sup> are required to enable the non-volatile function in  $\text{VO}_2$  optical memory. Another main branch of PCMs is chalcogenides, which can be rapidly and reversibly switched between amorphous and crystalline states. For the current on-chip integration of PCMs, the phase transitions are triggered by photothermal and electrothermal approaches.<sup>[330,357]</sup> In the photothermal triggered system, as shown in Figure 9d, a short pulse of a focused laser beam with high intensity can locally heat the well-studied PCM, alloy  $\text{Ge}_2\text{Sb}_2\text{Te}_5$  (GST), above the melting temperature to initiate the amorphization in a part of GST.<sup>[355]</sup> The resulting amorphous state can be read out by a low-intensity laser beam. Erasure is accomplished by heating above the crystallization temperature (but below the melting temperature) for a few nanoseconds. As a result, their on-chip memories feature single-shot readout with low switching energies of 13.4 pJ and high speeds of around 1 GHz. Alternatively, electrothermal tuning of PCMs using microheaters to enable their phase transitions. Transparent heaters including indium-tin-oxide (ITO) and fluorine-doped tin oxide (FTO),<sup>[358,359]</sup> or graphene heaters,<sup>[360,361]</sup> can be adopted for low insertion losses. In 2022, C. Rios et al. also explored using doped Si as both the light guide and resistive heater to actuate structural phase transition in  $\text{Sb}_2\text{Se}_3$  via single electrical pulses.<sup>[336]</sup> The device configuration is presented in Figure 9e. A section of the waveguide was phosphorus doped to act as a microheater, demonstrating record phase modulation up to  $0.09 \pi \mu\text{m}^{-1}$  with a low insertion loss of  $\approx 0.01 \text{ dB } \mu\text{m}^{-1}$ .

Ferroelectric materials possess an inherent electric dipole moment, or spontaneous polarization, that can be altered by the application of an external electric field in a non-volatile manner.<sup>[362,363]</sup> By exploiting the polarization-sensitive photonic response of ferroelectric materials, it is also possible to design photonic memory devices that can store and retrieve information compactly and efficiently. Barium titanate (BTO) is one of the most well-studied ferroelectric materials, known for its superior Pockels coefficient of approximately 923 pm V<sup>-1</sup> in thin film architectures.<sup>[364]</sup> Geler-Kremer et al. have recently presented a non-volatile electro-optic phase shifter that utilizes  $\text{BaTiO}_3$  thin films monolithically integrated with silicon waveguides, as depicted in Figure 9f.<sup>[337]</sup> By selectively manipulating ferroelectric domains in BTO via electrical control signals, the authors achieve precise and non-volatile tuning of the optical phase without introducing any significant changes in optical absorption. The

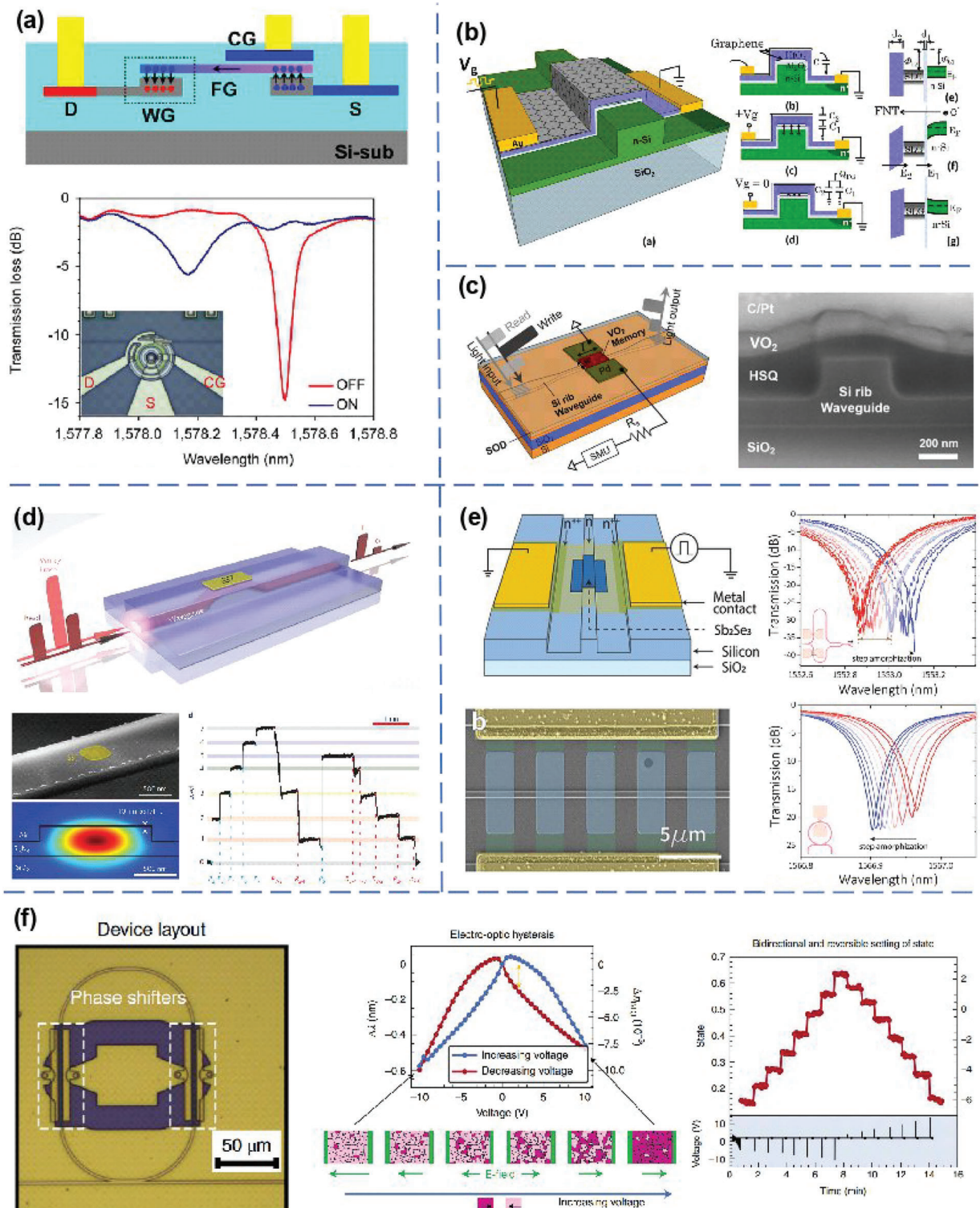


**Figure 9.** Waveguide-integrated photonic memories. a) Polycrystalline-silicon floating gate for non-volatile memory. Adapted with permission.<sup>[344]</sup> Copyright 2016, Springer Nature. b) Graphene-based floating gate non-volatile optical switch. Adapted with permission.<sup>[334]</sup> Copyright 2015, IEEE. c) Waveguide-integrated VO<sub>2</sub>-Si optical memory. Adapted with permission.<sup>[343]</sup> Copyright 2022, American Chemical Society. d) Integrated all-photonic multi-level memory based on GST. Adapted with permission.<sup>[335]</sup> Copyright 2015, Springer Nature. e) Electrically reprogrammable PCM for ultracompact non-volatile phase shifter. Adapted with permission.<sup>[336]</sup> Copyright 2012, Springer Open. f) Ferroelectric multi-level non-volatile phase shifter. Adapted with permission.<sup>[337]</sup> Copyright 2022, Springer Nature.

resulting device demonstrates stable and high-fidelity operation with eight levels of phase modulation, offering a nondestructive optical readout and exceptionally low switching energy, as low as 4.6 pJ. This work represents a significant advance in the development of photonic memory devices and provides important insights into the potential for the integration of ferroelectric materials with silicon-based photonic circuits.

## 10. Photonic Neural Network

Recently, the rising of artificial intelligence (AI) greatly accelerated the development of Internet of Things (IoT) technology. Massive and various information from the widespread deployment of sensor nodes is expected to be processed by efficient edge computing systems in an autonomous and high-speed manner and sent to the cloud for data storage or further processing. However, limited by the physics and fabrication technology, the electronic integrated circuits will eventually be unable to provide huge computation power and fulfill the requirement of ever-increasing processing speed, which impedes further interaction between different edge computing systems. As an alternative solution for this daunting challenge, the photonic computation chips equipped with AI capability, namely the on-chip photonic neural network (PNN), have been proposed and reported in recent years with several successful functional demonstrations.<sup>[15,28,365–370]</sup> Relying on the intrinsic property of light, the computation task can be implemented at ultrafast speed without power consumption in propagation in the ideal case,<sup>[371]</sup> and the large optical bandwidth (tens of THz)<sup>[372]</sup> is also beneficial for high-capacity signal transmission and modulation using the extra dimensions of light, e.g., wavelength or polarization, as compared with the electronic integrated circuits. Based on the above unique merits, the PNN is deemed as one of the most promising candidates to realize the AI-enhanced edge computing system by partially replacing or hybrid integrated with the necessary electronic components.

In 2017, on-chip deep learning (DL) using a coherent nanophotonic circuit, which has been demonstrated by Shen et al., completely motivated the upsurge of research interest in PNN. As shown in **Figure 10a**, by cascading 56 programmable MZI with 2 phase shifters (PS) in a specific arrangement, the array of MZI can represent any unitary matrix ( $U$  or  $V^\dagger$ ) and rectangular diagonal matrix ( $\Sigma$ ). As a real-valued matrix ( $M$ ) can be decomposed to the multiplication of these two types of matrices ( $M = U\Sigma V^\dagger$ ) through singular value decomposition, the shown MZI array is capable of expressing the desired weight matrix in each layer of the neural network by configuring the PSs in MZIs accordingly. After the input light encoded by the input vector passes through the programmed MZI array, the matrix-vector multiplication (MVM), which is the core operation in the neural network, will automatically execute in the propagation and output the corresponding light intensity, namely the multiplication result of weight matrix and the input vector. In the proof of concept, although the on-chip training is not presented, the vowel recognition in the inference step is successfully achieved with an accuracy of 76.7%. Compared with the recognition accuracy of 91.7% using a digital computer, the degradation of accuracy is mainly because of the thermal crosstalk between different PSs, which can be suppressed by the following calibration steps or adding

the thermal isolation trenches. Overall, the proposed nanophotonic circuit proves the feasibility of performing AI computation with enhanced computational speed and power efficiency, and still leaving space to raise the integration level of PNN for further developing and utilizing the advantage of light in PNN.

Despite this MZI-based PNN employing light interference to accomplish intensity modulation and element encoding, one thing we should note is that a real-value weight matrix instead of a complex-valued matrix is adopted, while the interference-based PNN is capable of constructing a complex-valued neural network by tuning the intensity and phase of light. In 2021, Zhang et al. reported an optical neural chip for implementing the complex-valued neural network. As shown in **Figure 10b**, the whole chip is divided into three parts: input preparation, weight multiplication & accumulation and coherent detection. In the part of input preparation, the multi-input light signals dictated by the machine learning (ML) task will be encoded through the internal PS and external PS of MZI in terms of magnitude and phase. Then, the complex-valued input will pass through the part of weight multiplication & accumulation to perform the complexed-valued MVM and the summation is realized by passively light interference. Finally, the magnitude and phase information of the output vector is recovered by coherent detection using the intensity of the output signal light and reference light. Compared with its real-valued counterparts, an 8.5% improvement in accuracy is obtained by employing this complex-valued PNN in handwriting recognition with a testing accuracy of 90.5%. By combining the advantage of the complex-valued neural network (e.g., fast learning rate and more trainable parameters in the same physical chip structure) and photonic integrated circuits, this work shows the possibility of implementing large-scale optical DL algorithms using the proposed PNN.

Besides the superiority in executing complex-valued neural networks, another unique advantage of light in performing ML tasks is the capability of parallel processing, for example, WDM. In 2021, Feldmann et al. developed an integrated photonic tensor core for parallel convolutional processing, as shown in **Figure 10c**. The whole computing platform consists of a frequency comb as a multi-wavelength source, a directional coupler-based on-chip photonic tensor core, which is covered with phase change material<sup>[3]</sup> (PCM) for non-volatile memory, as an optical kernel in convolution neural network (CNN), and multiplexing/ demultiplexing components for performing convolution in 16 wavelength channels simultaneously. An accuracy of 95.3% is achieved in MNIST handwritten digit recognition by experimentally implemented CNN, which is comparable with the calculated prediction accuracy (96.1%). This work demonstrated the true in-memory photonic computing with WDM for parallel and fast optical signal processing, and the computation speed is expected to further rising (e.g.,  $10^{15}$  multiply-accumulate operations per second) based on advanced photonics and fabrication technology.

Currently, most PNN demonstration is focused on the realization of the single-layer neural network; reuse of chips or takeover by computer is still required for following layer processing. Besides, the input dataset still needs to record in the memory unit before sending it to the PNN, which restrains the processing speed. In 2022, Ashtiani et al. first presented an integrated end-to-end PNN with three layers of CNN in the same chips (**Figure 10d**). An array of grating couplers is used to directly receive the

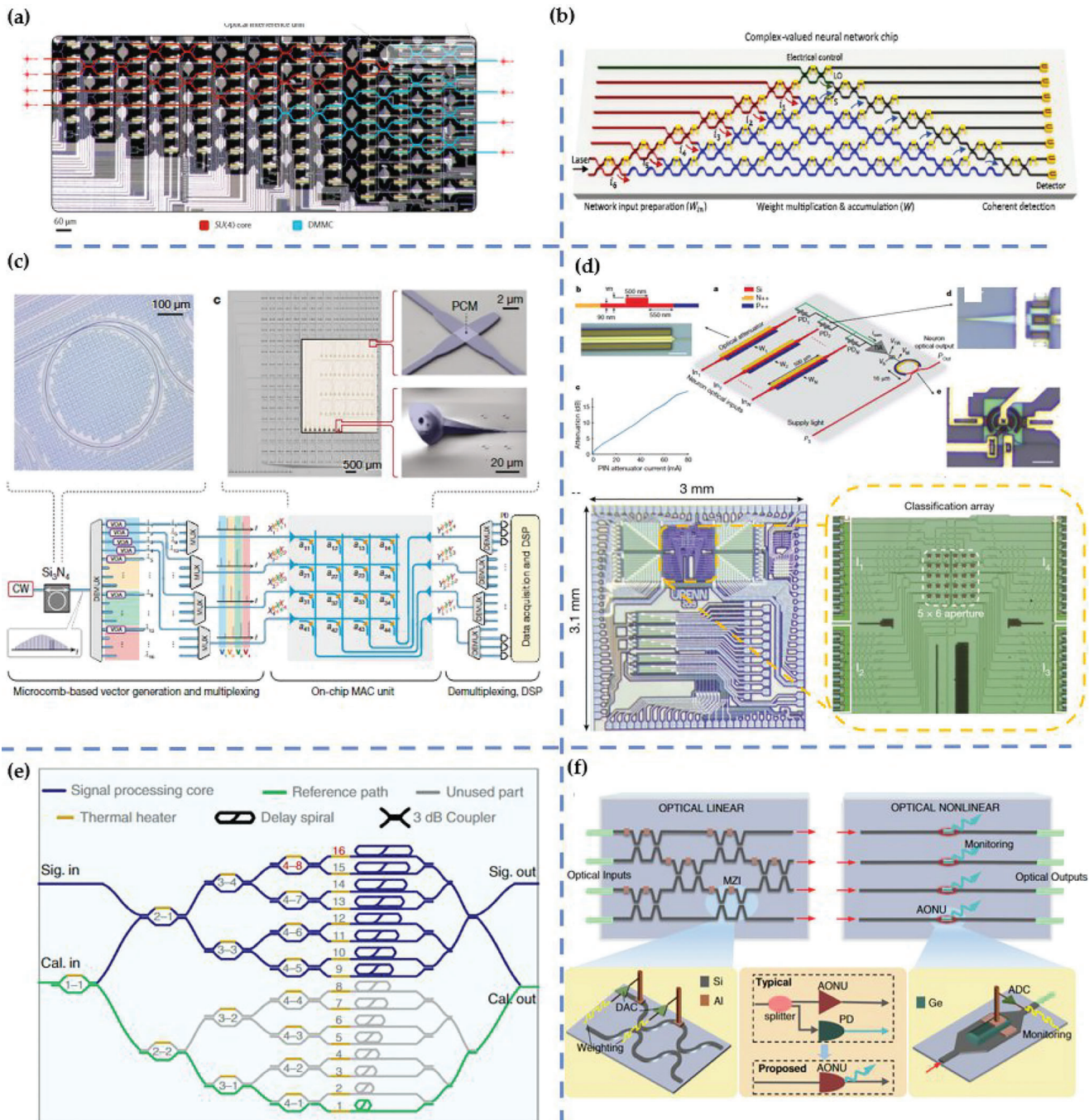


**Figure 10.** Schematic of several reported PNN. **a)** On-chip ML using a coherent nanophotonic circuit configured by the MZI array. This is the first demonstration of photonic interference computing chip. Adapted with permission.<sup>[373]</sup> Copyright 2017, Springer Nature. **b)** An optical neural chip for performing complex-valued neural network. Adapted with permission.<sup>[374]</sup> Copyright 2021, Springer Nature. **c)** An integrated photonic tensor core for parallel convolutional processing using PCM and frequency comb. Adapted with permission.<sup>[3]</sup> Copyright 2021, Springer Nature. **d)** An on-chip PNN for image classification, including the optical information receiving unit and computation unit. Adapted with permission.<sup>[375]</sup> Copyright 2022, Springer Nature. **e)** A self-calibrating programmable photonic integrated circuits for fast-converging training of on-chip parameters. Adapted with permission.<sup>[376]</sup> Copyright 2022, Springer Nature. **f)** An MZI-based PNN with Ge-Si photodiode for on-chip monitoring and activation. Adapted with permission.<sup>[377]</sup> Copyright 2022, Springer Nature.

image formed by the light passing through the pixels printed on the transparent films. In the route of light, the optical attenuator is responsible for the one-to-one weight elements encoding as well as MVM, while the summation is performed in the electrical domain: the current generated from on-chip SiGe photodiodes in each branch are summed together. Following the dataflow in the neural network, the summed current will convert to the voltage through TIA and be applied in one PN junction microring modulator (MRR) to execute the ReLU activation function. Then the light output of MRR, which corresponds to the output of ReLU, will be the input element of the next neural layer. An accuracy of 89.8% is realized in classifying four-class letter images. Albeit the structure of demonstrated on-chip neural network is still relatively small, this PNN provides a viable solution for increasing the layer numbers and integration level of PNN in single chips, which premises the great potential for the next generations of photonic ML systems.

In addition to realizing the on-chip inference task, how to effectively accomplish the training of neural network on-chip rather than training on the computer is also one of the challenges that need to be overcome in developing advanced PNN. In 2020, Zhou et al. proposed a self-configuring and reconfigurable photonic signal processor.<sup>[378]</sup> Instead of relying on the back-propagation algorithm for gradient descent, only the fine-tuning of each PS through the electronic control interface is needed after obtaining the result from front propagation to gradually approach the optimal solution. Based on this self-configuring training method, three signal processing functions: optical switching, optical MIMO descrambler, and tunable optical filter have been demonstrated. Except for the gradient descent method, other training algorithms, such as genetic algorithm<sup>[379]</sup> and bacterial foraging,<sup>[380]</sup> have also been applied to the PNN for a more simple on-chip training process. Going one step further, a self-calibrating programmable photonic integrated circuit for precise and fast-converging training is shown in Figure 10e. The self-calibration is realized by three steps: introducing the reference path into the circuit, using the Kramers-Kronig relationships to retrieve the phase information based on amplitude measurements and employing a rapid convergence self-calibration algorithm. A function of dial-up signal processing with complex impulse responses is demonstrated using only 25 training iterations. Nonlinear activation function completed in the optical domain is of great importance to achieve all-optical computing.<sup>[381]</sup> A PNN with a non-intrusive self-monitoring function, as well as activation, is presented at the end of 2022 (Figure 10f). Counting on the custom-designed Ge–Si photodiode at the end of the MZI array, a part of the output light will convert to photocurrent, and the rest of the output light that passes through the photodiode will be imposed the activation due to the free carrier absorption effect. With the photocurrent, the power of light that inject into the photodiode can be obtained, then the power of output light from the photodiode (activation result) can be uniquely determined so that achieving the monitoring operation. An *in situ* training for object classification and semantic segmentation tasks is completed based on the monitoring signal, and an accuracy of 97.3% in MNIST handwriting recognition is attained in simulation using the FCA-based activation function. Building upon the realization of several self-driving functions and the compact circuit structure design, we can confidently anticipate a

large-scale and highly-integrated PNN with high-speed and automatic processing capability to reform the current edge computing system in the future.

## 11. Photonics Future Application

In recent years, the field of smart photonics has experienced tremendous growth and advancement. In addition to its utilization in data processing and data communication, photonic technologies have found various applications in areas such as wearable photonics, encryption of data, human–machine interfaces, LiDAR, and many others.

Wearable photonics offers a promising solution for its robust optical sensing, high data transmission speed, and advanced data multiplexing technology. A combination of photonics and triboelectric nanogenerator (TENG) can reduce power consumption and generate a low-power consumption wearable system as shown in Figure 11a.<sup>[382]</sup> The TENG senses the mechanical signal and converts it into electrical signals through the interaction of triboelectrification and electrostatic induction.<sup>[385–389]</sup> The high voltage generated by the TENG can be used by an AlN modulator, with its moderate Pockels effect. Additionally, the capacitive nature of the AlN modulator allows for open-circuit operation of the TENG, providing continuous force sensing capability that is not affected by operating speeds. Biometrics-protected optical communication can be constructed by combining triboelectric and photonic technology, which is shown in Figure 11b.<sup>[27]</sup> The combination enables the multiplexing biometric information into the optical signal and this multiplexing consumes zero power.

Besides biometrics-protected optical communication, various human–machine interfaces (HMIs) have been developed including interactive gloves, eye blinking/body motion-triggered interfaces, voice/breath monitors, and self-induced wireless interfaces.<sup>[390–397]</sup> A typical structure of TENG photonic HMI is shown in Figure 11c-i.<sup>[326]</sup> A combination of TENG and AlN modulators for readout is proposed as shown in Figure 11c-ii. The electrical signals from TENG transform into the photonic form through AlN MZI modulators. Finally, the TENG HMI is used for robotic hand control. This work demonstrates a generic approach for developing self-sustainable TENG HMIs with stable, low power consumption, and real-time features for wearable systems.

LiDAR technology has attracted a lot of attention due to its huge application potential.<sup>[398–400]</sup> The silicon photonics LiDAR modules have several advantages compared to traditional mechanical LiDAR. First, it can provide on-chip optics without external optical elements to minimize the size. Moreover, integrated optical filters are used to reduce noise influence. Furthermore, the absence of extra optics and mechanical parts enables the module robust toward mechanical shocks. Finally, the fabrication process for the silicon photonics LiDAR is compatible with the existing CMOS process. Among many kinds of solid-state LiDAR, focal plane array-based 3D sensors stand out among other solid-state LiDARs due to their electronic scanning without mechanical moving parts.<sup>[383]</sup> A Schematic of the 2D focal plane switch array with the lens and output beam is shown in Figure 11d-i. Light is coupled onto the photonic chip employing one of the input ports and then routed to the selected grating antenna by turning on the corresponding row and column. Figure 11d-ii shows

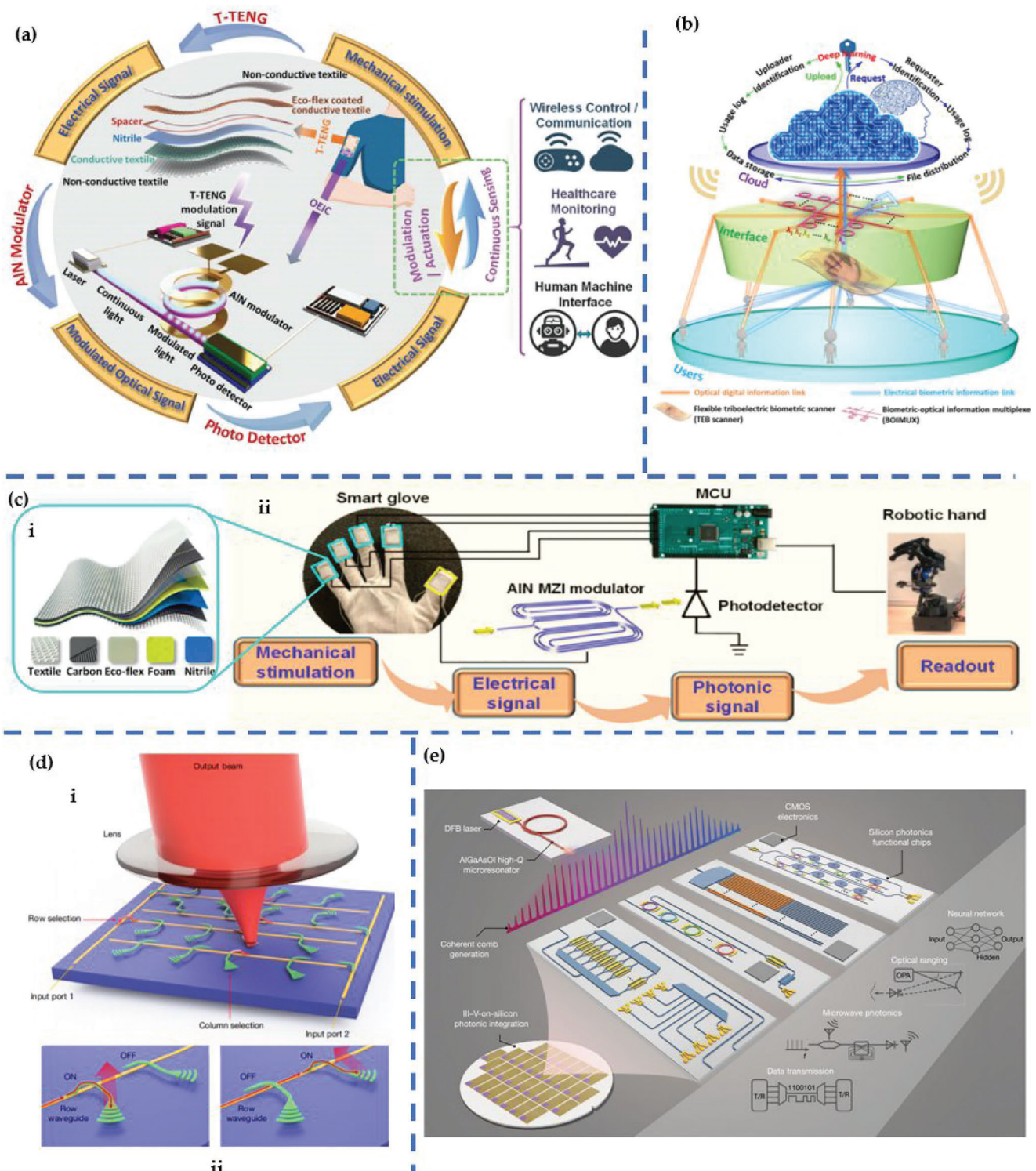


**Figure 11.** PICs towards emerging applications. a) Wearable triboelectric/photonics nano-energy-nano-system (NENS) featuring the integration of photonic modulator and textile triboelectric nanogenerator on a wearable platform from Dong et al. Adapted with permission.<sup>[382]</sup> Copyright 2020, Wiley-VCH. b) Architecture and operation principle of biometrics-protected optical communication from Dong et al. Adapted with permission.<sup>[27]</sup> Copyright 2020, AAAS. c-i) Textile interface. c-ii) Continuous real-time robotic hand control using the smart glove based on wearable THMI–nanophotonic systems from Dong et al. Adapted with permission.<sup>[326]</sup> Copyright 2020, American Chemical Society. d-i) Focal plane switch array of grating antennas and MEMS actuated optical switch from Zhang et al. Adapted with permission.<sup>[383]</sup> Copyright 2022, Springer Nature. d-ii) 1D FPSA beam scanner demonstrating the working principle. e) Microcomb-based silicon photonic optoelectronic systems from Shu et al. Adapted with permission.<sup>[384]</sup> Copyright 2022, Springer Nature.

schematics of the MEMS optical switches and grating antennas in different states.

Combining microcomb and other photonic components is also a key technology in optical computing, atomic clock, and synthesizer systems.<sup>[401–404]</sup> An AlGaAs-on-insulator microresonator is used to generate a microcomb that can be directly pumped by a distributed on-chip laser. Such a coherent comb is used to drive silicon photonics that contains versatile functionalities as shown in Figure 11e.<sup>[384]</sup> Thin-film lithium niobate is also a leading platform for microcomb.<sup>[405]</sup> Based on this combination, communication and microwave system-level integrated photonics are demonstrated, which show high performance with a small footprint and high performance. Combining microcomb and other photonic components makes the full integration of a wide range of optical systems possible and will significantly accelerate the development of PICs. Microcomb-driven silicon photonic systems will provide a mass-produced and low-cost solution to a broad range of optoelectronics applications, therefore facilitating the next generation of integrated photonics.

In conclusion, the integration of photonics and multidisciplinary has become one of its core development directions with the continuous development of photonics. Through the cross-integration and mutual reference of photonics and broader disciplines, it is expected to explore more applications making full use of photonics. Photonics is also expected to develop photonic chiplet technologies that are weakly related to intellectual property block or fabrication processes, seek better performance and realize rapid development to further enhance the performance of existing photonic devices and systems.

## 12. Conclusion

In this review, we reviewed the recent advances achieved in silicon-based PICs. An overview of basic components and functional blocks is displayed. Silicon-based PICs shows great promise for low-power application, high-sensitivity sensors, and high-speed computational capability. Especially in the post-Moore era, PICs technology has become a necessary solution to reduce IO power consumption and increase bandwidth and integrated photonic sensors pave the way to miniaturize the sensors and increase their sensitivity. Hence, PICs are an emerging field that combines speed and power consumption for next-generation applications.

However, silicon-based PICs currently encounter limitations in technological advancements, such as the lack of systematic design methods compared to its electronic partner, standardized manufacturing processes, as well as the need for improved density of photonic devices. Although photonics has demonstrated excellent communication performance in the past forty years, PICs are a relatively recent research focus. A systematic design method for PICs has not been established and the footprint of the current photonic functional block is bigger than its electronic partner, which increases the cost for the same quantity due to the CMOS fabrication process. Furthermore, optical calculation precision is lower than that of electronic chips, which constrains the potential uses of optical chips.

Besides systematic design tools, more promising optical materials should be investigated and their fabrication process should be compatible with the current CMOS fabrication process to re-

duce the cost and achieve large-scale manufacturing. Silicon-based PICs exhibit several inherent limitations, including restricted thermal tolerance, susceptibility to nanoscale dimension variations and postfabrication rigidity. As a promising alternative, organic photonics presents several distinct advantages, such as tunable electronic bandgap, good solution processability, and mechanical flexibility.<sup>[406–419]</sup> Moreover, various essential components, including lasers, waveguides, resonators, modulators, sensors, and functional circuits, have already been successfully demonstrated in this field.<sup>[215,216,420–424]</sup> Ultimately, to unlock the complete potential of optical chips in terms of performance and cost, it is essential to fully develop the photonic functional blocks, CMOS fabrication process, and packaging.

## Acknowledgements

Z.X., W.L., S.X., and J.Z. contributed equally to this work. This work was partly funded by Singapore Ministry of Education (MOE) Academic Research Fund Tier 2, grant number MOE-T2EP502200014. This work was also sponsored by Advanced Research and Technology Innovation Centre Project, grant number HWMRP1/A-0005947-20-00 and National Research Foundation Competitive Research Programme, grant number NRCRP15-2015-02.

## Conflict of Interest

The authors declare no conflict of interest.

## Keywords

integrated photonics, optoelectronics, photonic devices, photonic integrated circuits, silicon photonics

Received: May 2, 2023

Revised: July 24, 2023

Published online: September 10, 2023

- [1] S. K. Garg, S. Versteeg, R. Buyya, *Future Gener. Comput. Syst.* **2013**, *29*, 1012.
- [2] S. Madakam, R. Ramaswamy, S. Tripathi, *J. Comput. Commun.* **2015**, *3*, 164.
- [3] J. Feldmann, N. Youngblood, M. Karpov, H. Gehring, X. Li, M. Stappers, M. Le Gallo, X. Fu, A. Lukashchuk, A. S. Raja, J. Liu, C. D. Wright, A. Sebastian, T. J. Kippenberg, W. H. P. Pernice, H. Bhaskaran, *Nature* **2021**, *589*, 52.
- [4] F. Wen, T. He, H. Liu, H. Y. Chen, T. Zhang, C. Lee, *Nano Energy* **2020**, *78*, 105155.
- [5] B. Dong, Q. Shi, Y. Yang, F. Wen, Z. Zhang, C. Lee, *Nano Energy* **2021**, *79*, 105414.
- [6] L. Liu, X. Guo, C. Lee, *Nano Energy* **2021**, *88*, 106304.
- [7] Q. Shi, Z. Zhang, Y. Yang, X. Shan, B. Salam, C. Lee, *ACS Nano* **2021**, *15*, 18312.
- [8] L. Liu, X. Guo, W. Liu, C. Lee, *Nanomaterials* **2021**, *11*, 2975.
- [9] J. Zhu, H. Wang, Z. Zhang, Z. Ren, Q. Shi, W. Liu, C. Lee, *Nano Energy* **2020**, *73*, 104760.
- [10] S. Chen, H. Xu, D. Liu, B. Hu, H. Wang, *IEEE Internet Things J.* **2014**, *1*, 349.
- [11] Z. Yang, Y. Yue, Y. Yang, Y. Peng, X. Wang, W. Liu, *2011 Int. Conf. on Multimedia Technology* (Ed.: A. A. Farag), IEEE, Piscataway, NJ **2011**, pp. 747–751.

- [12] W. Liu, M. Li, R. S. Guzzon, E. J. Norberg, J. S. Parker, M. Lu, L. A. Coldren, J. Yao, *Nat. Photonics* **2016**, *10*, 190.
- [13] W. Zhang, A. Tait, C. Huang, T. Ferreira de Lima, S. Bilodeau, E. C. Blow, A. Jha, B. J. Shastri, P. Prucnal, *Nat. Commun.* **2023**, *14*, 1107.
- [14] T. Wu, M. Menarini, Z. Gao, L. Feng, *Nat. Photonics* **2023**, *17*, 710.
- [15] G. Mourgias-Alexandris, M. Moralis-Pegios, A. Tsakyridis, S. Simos, G. Dabos, A. Totovic, N. Passalis, M. Kirtas, T. Rutirawut, F. Y. Gardes, A. Tefas, N. Pleros, *Nat. Commun.* **2022**, *13*, 5572.
- [16] J. Bao, Z. Fu, T. Pramanik, J. Mao, Y. Chi, Y. Cao, C. Zhai, Y. Mao, T. Dai, X. Chen, X. Jia, L. Zhao, Y. Zheng, B. Tang, Z. Li, J. Luo, W. Wang, Y. Yang, Y. Peng, D. Liu, D. Dai, Q. He, A. L. Muthali, L. K. Oxenløwe, C. Vigliari, S. Paesani, H. Hou, R. Santagati, J. W. Silverstone, A. Laing, et al., *Nat. Photonics* **2023**, *17*, 573.
- [17] M. Prabhu, C. Errando-Herranz, L. De Santis, I. Christen, C. Chen, C. Gerlach, D. Englund, *Nat. Commun.* **2023**, *14*, 2380.
- [18] T. Yan, R. Yang, Z. Zheng, X. Lin, H. Xiong, Q. Dai, *Sci. Adv.* **2022**, *8*, eabn7630.
- [19] K. K. Mehta, C. D. Bruzewicz, R. McConnell, R. J. Ram, J. M. Sage, J. Chiaverini, *Nat. Nanotechnol.* **2016**, *11*, 1066.
- [20] A. Khilo, S. J. Spector, M. E. Grein, A. H. Nejadmalayeri, C. W. Holzwarth, M. Y. Sander, M. S. Dahlem, M. Y. Peng, M. W. Geis, N. A. DiLello, J. U. Yoon, A. Motamedi, J. S. Orcutt, J. P. Wang, C. M. Sorace-Agaskar, M. A. Popović, J. Sun, G.-R. Zhou, H. Byun, J. Chen, J. L. Hoyt, H. I. Smith, R. J. Ram, M. Perrott, T. M. Lysczarz, E. P. Ippen, F. X. Kärtner, *Opt. Express* **2012**, *20*, 4454.
- [21] A. H. Atabaki, S. Moazeni, F. Pavanello, H. Gevorgyan, J. Notaros, L. Alloatti, M. T. Wade, C. Sun, S. A. Kruger, H. Meng, K. Al Qubaisi, I. Wang, B. Zhang, A. Khilo, C. V. Baiocco, M. A. Popović, V. M. Stojanović, R. J. Ram, *Nature* **2018**, *556*, 349.
- [22] V. Stojanović, R. J. Ram, M. Popović, S. Lin, S. Moazeni, M. Wade, C. Sun, L. Alloatti, A. Atabaki, F. Pavanello, N. Mehta, P. Bhargava, *Opt. Express* **2018**, *26*, 13106.
- [23] J. S. Orcutt, B. Moss, C. Sun, J. Leu, M. Georgas, J. Shainline, E. Zgraggen, H. Li, J. Sun, M. Weaver, S. Urošević, M. Popović, R. J. Ram, V. Stojanović, *Opt. Express* **2012**, *20*, 12222.
- [24] B. J. Shastri, A. N. Tait, T. Ferreira de Lima, W. H. P. Pernice, H. Bhaskaran, C. D. Wright, P. R. Prucnal, *Nat. Photonics* **2021**, *15*, 102.
- [25] M. Lipson, *Nat. Mater.* **2022**, *21*, 974.
- [26] W. Bogaerts, P. De Heyn, T. Van Vaerenbergh, K. De Vos, S. Kumar Selvaraja, T. Claes, P. Dumon, P. Bienstman, D. Van Thourhout, R. Baets, *Laser Photonics Rev.* **2012**, *6*, 47.
- [27] B. Dong, Z. Zhang, Q. Shi, J. Wei, Y. Ma, Z. Xiao, C. Lee, *Sci. Adv.* **2022**, *8*, eab19874.
- [28] J. Y. S. Tan, Z. Cheng, J. Feldmann, X. Li, N. Youngblood, U. E. Ali, C. D. Wright, W. H. P. Pernice, H. Bhaskaran, *Optica* **2022**, *9*, 792.
- [29] Q. Qiao, X. Liu, Z. Ren, B. Dong, J. Xia, H. Sun, C. Lee, G. Zhou, *ACS Photonics* **2022**, *9*, 2367.
- [30] J. Midkiff, K. M. Yoo, J.-D. Shin, H. Dalir, M. Teimourpour, R. T. Chen, *Optica* **2020**, *7*, 1544.
- [31] W. Liu, Y. Ma, Y. Chang, B. Dong, J. Wei, Z. Ren, C. Lee, *Nanophotonics* **2021**, *10*, 1861.
- [32] Y. Chen, H. Lin, J. Hu, M. Li, *ACS Nano* **2014**, *8*, 6955.
- [33] C. Sun, C.-H. O. Chen, G. Kurian, L. Wei, J. Miller, A. Agarwal, L.-S. Peh, V. Stojanovic, in *2012 IEEE/ACM Sixth Int. Symp. on Networks-on-Chip* (Eds: J. Sparsø, J. Madsen), IEEE, Piscataway, NJ **2012**, pp. 201–210.
- [34] C. Sun, M. T. Wade, Y. Lee, J. S. Orcutt, L. Alloatti, M. S. Georgas, A. S. Waterman, J. M. Shainline, R. R. Avizienis, S. Lin, B. R. Moss, R. Kumar, F. Pavanello, A. H. Atabaki, H. M. Cook, A. J. Ou, J. C. Leu, Y.-H. Chen, K. Asanović, R. J. Ram, M. A. Popović, V. M. Stojanović, *Nature* **2015**, *528*, 534.
- [35] A. Sludds, S. Bandyopadhyay, Z. Chen, Z. Zhong, J. Cochrane, L. Bernstein, D. Bunandar, P. ben Dixon, S. A. Hamilton, M. Streshinsky, A. Novack, T. Baehr-Jones, M. Hochberg, M. Ghobadi, R. Hamerly, D. Englund, *Science* **2022**, *378*, 270.
- [36] A. P. Ovyyan, M.-K. Li, H. Gehring, F. Beutel, S. Kumar, F. Hennrich, L. Wei, Y. Chen, F. Pyatkov, R. Krupke, W. H. P. Pernice, *Nat. Commun.* **2023**, *14*, 3933.
- [37] Y. Zhang, K. Zhong, X. Zhou, H. K. Tsang, *Nat. Commun.* **2022**, *13*, 3534.
- [38] A. Anopchenko, A. Tengattini, A. Marconi, N. Prtljaga, J. M. Ramírez, O. Jambois, Y. Berencén, D. Navarro-Urrios, B. Garrido, F. Milesi, J.-P. Colonna, J.-M. Fedeli, L. Pavesi, *J. Appl. Phys.* **2012**, *111*, 063102.
- [39] A. Ghrib, M. de Kersauson, M. El Kurdi, R. Jakomin, G. Beaudoin, S. Sauvage, G. Fishman, G. Ndong, M. Chaigneau, R. Ossikovski, I. Sagnes, P. Boucaud, *Appl. Phys. Lett.* **2012**, *100*, 201104.
- [40] G. de Valicourt, G. Levaufre, Y. Pointurier, A. Le Liepvre, J.-C. Antona, C. Jany, A. Accard, F. Lelarge, D. Make, G.-H. Duan, *J. Lightwave Technol.* **2015**, *33*, 1608.
- [41] M. Tang, S. Chen, J. Wu, Q. Jiang, V. G. Dorogan, M. Benamara, Y. I. Mazur, G. J. Salamo, A. Seeds, H. Liu, *Opt. Express* **2014**, *22*, 11528.
- [42] D. Liang, J. E. Bowers, *Nat. Photonics* **2010**, *4*, 511.
- [43] Z. Zhou, B. Yin, J. Michel, *Light: Sci. Appl.* **2015**, *4*, e358.
- [44] Z. Wang, A. Abbasi, U. Dave, A. De Groote, S. Kumari, B. Kunert, C. Merckling, M. Pantouvakis, Y. Shi, B. Tian, K. Van Gasse, J. Verbist, R. Wang, W. Xie, J. Zhang, Y. Zhu, J. Bauwelinck, X. Yin, Z. Hens, J. Van Campenhout, B. Kuyken, R. Baets, G. Morthier, D. Van Thourhout, G. Roelkens, *Laser Photonics Rev.* **2017**, *11*, 1700063.
- [45] N. Koshida, H. Koyama, *Appl. Phys. Lett.* **1992**, *60*, 347.
- [46] L. Pavesi, L. Dal Negro, C. Mazzoleni, G. Franzò, F. Priolo, *Nature* **2000**, *408*, 440.
- [47] E. Minoux, O. Groening, K. B. K. Teo, S. H. Dalal, L. Gangloff, J.-P. Schnell, L. Hudanski, I. Y. Y. Bu, P. Vincent, P. Legagneux, G. A. J. Amaralunga, W. I. Milne, *Nano Lett.* **2005**, *5*, 2135.
- [48] W. Zhu, C. Bower, O. Zhou, G. Kochanski, S. Jin, *Appl. Phys. Lett.* **1999**, *75*, 873.
- [49] O. Boyraz, B. Jalali, *Opt. Express* **2004**, *12*, 5269.
- [50] H. Rong, S. Xu, Y.-H. Kuo, V. Sih, O. Cohen, O. Raday, M. Paniccia, *Nat. Photonics* **2007**, *1*, 232.
- [51] H. Rong, A. Liu, R. Jones, O. Cohen, D. Hak, R. Nicolaescu, A. Fang, M. Paniccia, *Nature* **2005**, *433*, 292.
- [52] F. Priolo, G. Franzò, D. Pacifici, V. Vinciguerra, F. Iacona, A. Irrera, *J. Appl. Phys.* **2001**, *89*, 264.
- [53] M. Fujii, M. Yoshida, Y. Kanzawa, S. Hayashi, K. Yamamoto, *Appl. Phys. Lett.* **1997**, *71*, 1198.
- [54] G. Franzò, S. Boninelli, D. Pacifici, F. Priolo, F. Iacona, C. Bongiorno, *Appl. Phys. Lett.* **2003**, *82*, 3871.
- [55] X. Sun, J. Liu, L. C. Kimerling, J. Michel, *Appl. Phys. Lett.* **2009**, *95*, 011911.
- [56] X. Sun, J. Liu, L. C. Kimerling, J. Michel, *Opt. Lett.* **2009**, *34*, 1198.
- [57] J. Liu, X. Sun, R. Camacho-Aguilera, L. C. Kimerling, J. Michel, *Opt. Lett.* **2010**, *35*, 679.
- [58] J. Liu, X. Sun, D. Pan, X. Wang, L. C. Kimerling, T. L. Koch, J. Michel, *Opt. Express* **2007**, *15*, 11272.
- [59] G. Roelkens, J. Brouckaert, D. Taillaert, P. Dumon, W. Bogaerts, D. Van Thourhout, R. Baets, R. Nötzel, M. Smit, *Opt. Express* **2005**, *13*, 10102.
- [60] B. Ben Bakir, A. Descos, N. Olivier, D. Bordel, P. Grosse, E. Augendre, L. Fulbert, J. M. Fedeli, *Opt. Express* **2011**, *19*, 10317.
- [61] T. Okumura, T. Maruyama, H. Yonezawa, N. Nishiyama, S. Arai, *IEEE Photonics Technol. Lett.* **2009**, *21*, 283.
- [62] X. Sun, A. Yariv, *J. Opt. Soc. Am. B* **2008**, *25*, 923.
- [63] A. W. Fang, R. Jones, H. Park, O. Cohen, O. Raday, M. J. Paniccia, J. E. Bowers, *Opt. Express* **2007**, *15*, 2315.
- [64] J. Van Campenhout, P. Rojo Romeo, P. Regreny, C. Seassal, D. Van Thourhout, S. Verstuyft, L. Di Cioccio, J.-M. Fedeli, C. Lagahe, R. Baets, *Opt. Express* **2007**, *15*, 6744.

- [65] X. Sun, A. Zadok, M. J. Shearn, K. A. Diest, A. Ghaffari, H. A. Atwater, A. Scherer, A. Yariv, *Opt. Lett.* **2009**, *34*, 1345.
- [66] A. W. Fang, H. Park, O. Cohen, R. Jones, M. J. Paniccia, J. E. Bowers, *Opt. Express* **2006**, *14*, 9203.
- [67] J. A. Misewich, R. Martel, Ph. Avouris, J. C. Tsang, S. Heinze, J. Tersoff, *Science* **2003**, *300*, 783.
- [68] N. A. Peyyety, S. Kumar, M.-K. Li, S. Dehm, R. Krupke, *ACS Appl. Mater. Interfaces* **2022**, *14*, 9525.
- [69] A. Riaz, F. Pyatkov, A. Alam, S. Dehm, A. Felten, V. S. K. Chakravadhanula, B. S. Flavel, C. Kübel, U. Lemmer, R. Krupke, *Nanotechnology* **2015**, *26*, 325202.
- [70] F. Pyatkov, V. Fütterling, S. Khasminskaya, B. S. Flavel, F. Hennrich, M. M. Kappes, R. Krupke, W. H. P. Pernice, *Nat. Photonics* **2016**, *10*, 420.
- [71] C. Ji, D. Liu, C. Zhang, L. Jay Guo, *Nat. Commun.* **2020**, *11*, 3367.
- [72] J.-W. Zhang, G.-A. Xue, Y.-C. Cui, R.-T. Liu, *Emerging Mater. Res.* **2018**, *7*, 142.
- [73] X. Shen, H. Choi, D. Chen, W. Zhao, A. M. Armani, *Nat. Photonics* **2020**, *14*, 95.
- [74] H. Rong, R. Jones, A. Liu, O. Cohen, D. Hak, A. Fang, M. Paniccia, *Nature* **2005**, *433*, 725.
- [75] L. Sirleto, M. A. Ferrara, *Micromachines* **2020**, *11*, 247.
- [76] Y. Takahashi, Y. Inui, M. Chihara, T. Asano, R. Terawaki, S. Noda, *Nature* **2013**, *498*, 470.
- [77] L. Sirleto, M. Antonietta Ferrara, T. Nikitin, S. Novikov, L. Khriachtchev, *Nat. Commun.* **2012**, *3*, 1220.
- [78] Y. Zhang, K. Zhong, H. K. Tsang, *Laser Photonics Rev.* **2021**, *15*, 2000336.
- [79] M. Ahmadi, W. Shi, S. LaRochelle, *Optica* **2021**, *8*, 804.
- [80] R. Guo, B. Wang, X. Wang, L. Wang, L. Jiang, Z. Zhou, *Opt. Lett.* **2012**, *37*, 1427.
- [81] J. D. B. Bradley, M. Pollnau, *Laser Photonics Rev.* **2011**, *5*, 368.
- [82] H. Isshiki, M. J. A. de Dood, A. Polman, T. Kimura, *Appl. Phys. Lett.* **2004**, *85*, 4343.
- [83] X. Wang, X. Zhuang, S. Yang, Y. Chen, Q. Zhang, X. Zhu, H. Zhou, P. Guo, J. Liang, Y. Huang, A. Pan, X. Duan, *Phys. Rev. Lett.* **2015**, *115*, 027403.
- [84] M. Miritello, R. Lo Savio, F. Iacona, G. Franzò, A. Irrera, A. M. Piro, C. Bongiorno, F. Priolo, *Adv. Mater.* **2007**, *19*, 1582.
- [85] B. Wang, P. Zhou, X. Wang, *Appl. Sci.* **2022**, *12*, 11712.
- [86] L. Yin, D. Shelhammer, G. Zhao, Z. Liu, C. Z. Ning, *Appl. Phys. Lett.* **2013**, *103*, 121902.
- [87] Xiaochen Sun, Jifeng Liu, L. C. Kimerling, J. Michel, *IEEE J. Sel. Top. Quantum Electron.* **2010**, *16*, 124.
- [88] R. E. Camacho-Aguilera, Y. Cai, N. Patel, J. T. Bessette, M. Romagnoli, L. C. Kimerling, J. Michel, *Opt. Express* **2012**, *20*, 11316.
- [89] J. Ke, L. Chrostowski, G. Xia, *IEEE Photonics J.* **2017**, *9*, 1501615.
- [90] G.-H. Duan, S. Olivier, S. Malhouitire, A. Accard, P. Kaspar, G. de Valicourt, G. Levaufre, N. Girard, A. Le Liepvre, A. Shen, D. Make, F. Lelarge, C. Jany, K. Ribaud, F. Mallecot, P. Charbonnier, H. Gariah, C. Kopp, J.-L. Gentner, *J. Lightwave Technol.* **2015**, *33*, 976.
- [91] S. Keyvaninia, S. Verstuft, L. Van Landschoot, F. Lelarge, G.-H. Duan, S. Messaoudene, J. M. Fedeli, T. De Vries, B. Smalbrugge, E. J. Geluk, J. Bolk, M. Smit, G. Morthier, D. Van Thourhout, G. Roelkens, *Opt. Lett.* **2013**, *38*, 5434.
- [92] S. Keyvaninia, M. Muneeb, S. Stanković, P. J. Van Veldhoven, D. Van Thourhout, G. Roelkens, *Opt. Mater. Express* **2013**, *3*, 35.
- [93] S. Chen, M. Tang, Q. Jiang, J. Wu, V. G. Dorogan, M. Benamara, Y. I. Mazur, G. J. Salamo, P. Smowton, A. Seeds, H. Liu, *ACS Photonics* **2014**, *1*, 638.
- [94] A. Y. Liu, C. Zhang, J. Norman, A. Snyder, D. Lubyshev, J. M. Fastenau, A. W. K. Liu, A. C. Gossard, J. E. Bowers, *Appl. Phys. Lett.* **2014**, *104*, 041104.
- [95] T. Wang, H. Liu, A. Lee, F. Pozzi, A. Seeds, *Opt. Express* **2011**, *19*, 11381.
- [96] A. Lee, Q. Jiang, M. Tang, A. Seeds, H. Liu, *Opt. Express* **2012**, *20*, 22181.
- [97] L. Vivien, L. Pavesi, **2013**. *Handbook of Silicon Photonics* (1st ed.).
- [98] R. Marchetti, C. Lacava, L. Carroll, K. Gradkowski, P. Minzioni, *Photonics Res.* **2019**, *7*, 201.
- [99] B. Liu, G. Yang, S. Desai, K. Powell, W. Xie, L. Li, X. Yi, in *17th Int. Conf. on Optical Communications and Networks (ICOON2018)*, (Ed.: Z. Li), SPIE, Bellingham, Washington **2019**, p. 125.
- [100] J. Wang, Y. Xuan, C. Lee, B. Niu, L. Liu, G. N. Liu, M. Qi, in *Optical Fiber Communication Conf.* (Ed.: A. Lord), OSA, Washington, D.C **2016**, p. M2I.6.
- [101] A. He, X. Guo, T. Wang, Y. Su, *ACS Photonics* **2021**, *8*, 3226.
- [102] R. Takei, M. Suzuki, E. Omoda, S. Manako, T. Kamei, M. Mori, Y. Sakakibara, *Appl. Phys. Lett.* **2013**, *102*, 101108.
- [103] A. Mekis, S. Gloeckner, G. Masini, A. Narasimha, T. Pinguet, S. Sahni, P. de Dobbelaere, *IEEE J. Sel. Top. Quantum Electron.* **2011**, *17*, 597.
- [104] N. Chen, B. Dong, X. Luo, H. Wang, N. Singh, G.-Q. Lo, C. Lee, *Opt. Express* **2018**, *26*, 26242.
- [105] Z. Ren, B. Dong, Q. Qiao, X. Liu, J. Liu, G. Zhou, C. Lee, *InfoMat* **2022**, *4*, e12264.
- [106] Y.-S. Lin, C. P. Ho, K. H. Koh, C. Lee, *Opt. Lett.* **2013**, *38*, 902.
- [107] X. Mu, S. Wu, L. Cheng, H. Y. Fu, *Appl. Sci.* **2020**, *10*, 1538.
- [108] J. Wang, Y. Xuan, C. Lee, B. Niu, L. Liu, G. N. Liu, M. Qi, in *Optical Fiber Communication Conf.* (Ed.: K. Tse), Optica Publishing Group, Washington, D.C **2016** p. M2I.6.
- [109] P. Pitchappa, C. P. Ho, L. Cong, R. Singh, N. Singh, C. Lee, *Adv. Opt. Mater.* **2016**, *4*, 391.
- [110] Yu-Sheng Lin, Chia-Yi Huang, Chengkuo Lee, *IEEE J. Sel. Top. Quantum Electron.* **2015**, *21*, 93.
- [111] P. Pitchappa, C. P. Ho, Y. Qian, L. Dhakar, N. Singh, C. Lee, *Sci. Rep.* **2015**, *5*, 11678.
- [112] M. Manjappa, P. Pitchappa, N. Wang, C. Lee, R. Singh, *Adv. Opt. Mater.* **2018**, *6*, 1800141.
- [113] R. A. Shelby, D. R. Smith, S. Schultz, *Science* **2001**, *292*, 77.
- [114] J. B. Pendry, *Phys. Rev. Lett.* **2000**, *85*, 3966.
- [115] T. Baba, *Nat. Photonics* **2008**, *2*, 465.
- [116] D. Hasan, P. Pitchappa, J. Wang, T. Wang, B. Yang, C. P. Ho, C. Lee, *ACS Photonics* **2017**, *4*, 302.
- [117] C. P. Ho, P. Pitchappa, Y. S. Lin, C. Y. Huang, P. Kropelnicki, C. Lee, *Appl. Phys. Lett.* **2014**, *104*, 161104.
- [118] D. Hasan, C. Lee, D. Hasan, C. Lee, *Adv. Sci.* **2018**, *5*, 1700581.
- [119] H. Zhou, X. Hui, D. Li, D. Hu, X. Chen, X. He, L. Gao, H. Huang, C. Lee, X. Mu, *Adv. Sci.* **2020**, *7*, 2001173.
- [120] D. Hasan, C. Lee, *Adv. Sci.* **2018**, *5*, 1700581.
- [121] P. Pitchappa, C. Pei Ho, P. Kropelnicki, N. Singh, D.-L. Kwong, C. Lee, *Appl. Phys. Lett.* **2014**, *104*, 201114.
- [122] P. Pitchappa, C. P. Ho, P. Kropelnicki, N. Singh, D.-L. Kwong, C. Lee, *J. Appl. Phys.* **2014**, *115*, 193109.
- [123] P. Pitchappa, C. P. Ho, L. Dhakar, C. Lee, *Optica* **2015**, *2*, 571.
- [124] P. Pitchappa, C. Pei Ho, Y.-S. Lin, P. Kropelnicki, C.-Y. Huang, N. Singh, C. Lee, *Appl. Phys. Lett.* **2014**, *104*, 151104.
- [125] Y.-S. Lin, C. Lee, *Appl. Phys. Lett.* **2014**, *104*, 251914.
- [126] Z. Liu, C.-Y. Huang, H. Liu, X. Zhang, C. Lee, *Opt. Express* **2013**, *21*, 6519.
- [127] F. Ma, Y. Qian, Y.-S. Lin, H. Liu, X. Zhang, Z. Liu, J. Ming-Lin Tsai, C. Lee, *Appl. Phys. Lett.* **2013**, *102*, 161912.
- [128] Y.-S. Lin, F. Ma, C. Lee, *Opt. Lett.* **2013**, *38*, 3126.
- [129] Z. Wang, T. Li, A. Soman, D. Mao, T. Kananen, T. Gu, *Nat. Commun.* **2019**, *10*, 3547.

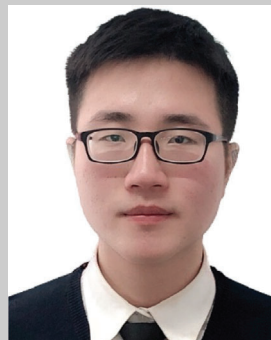
- [130] R. Halir, A. Ortega-Monux, D. Benedikovic, G. Z. Mashanovich, J. G. Wanguemert-Perez, J. H. Schmid, I. Molina-Fernandez, P. Cheben, *Proc. IEEE* **2018**, *106*, 2144.
- [131] P. Cheben, R. Halir, J. H. Schmid, H. A. Atwater, D. R. Smith, *Nature* **2018**, *560*, 565.
- [132] B. Shen, P. Wang, R. Polson, R. Menon, *Nat. Photonics* **2015**, *9*, 378.
- [133] R. Halir, P. Cheben, J. M. Luque-González, J. D. Sarmiento-Merenguel, J. H. Schmid, G. Wanguemert-Pérez, D. X. Xu, S. Wang, A. Ortega-Moñux, I. Molina-Fernández, *Laser Photonics Rev.* **2016**, *10*, 1039.
- [134] D. Hasan, C. P. Ho, P. Pitchappa, C. Lee, *ACS Photonics* **2015**, *2*, 890.
- [135] J. Wei, C. Lee, *Opt. Lett.* **2019**, *44*, 6041.
- [136] N. Chen, D. Hasan, C. P. Ho, C. Lee, *Adv. Mater. Technol.* **2018**, *3*, 1800014.
- [137] K. Shih, P. Pitchappa, M. Manjappa, C. P. Ho, R. Singh, C. Lee, *J. Appl. Phys.* **2017**, *121*, 023102.
- [138] X. Zhao, B. Yang, J. Liu, P. Pitchappa, D. Hasan, C. P. Ho, C. Yang, C. Lee, *J. Opt.* **2016**, *18*, 075101.
- [139] R. Takei, E. Omoda, M. Suzuki, S. Manako, T. Kamei, M. Mori, Y. Sakakibara, *Appl. Phys. Express* **2012**, *5*, 052202.
- [140] F. van Laere, G. Roelkens, M. Ayre, J. Schrauwen, D. Taillaert, D. van Thourhout, T. F. Krauss, R. Baets, *J. Lightwave Technol.* **2007**, *25*, 151.
- [141] Y. Luo, Z. Nong, S. Gao, H. Huang, Y. Zhu, L. Liu, L. Zhou, J. Xu, L. Liu, S. Yu, X. Cai, *Opt. Lett.* **2018**, *43*, 474.
- [142] S. Romero-García, F. Merget, F. Zhong, H. Finkelstein, J. Witzens, *Opt. Lett.* **2013**, *38*, 2521.
- [143] W. D. Sacher, J. C. Mikkelsen, Y. Huang, J. C. C. Mak, Z. Yong, X. Luo, Y. Li, P. Dumais, J. Jiang, D. Goodwill, E. Bernier, P. G.-Q. Lo, J. K. S. Poon, *Proc. IEEE* **2018**, *106*, 2232.
- [144] J. C. C. Mak, W. D. Sacher, H. Ying, X. Luo, P. G.-Q. Lo, J. K. S. Poon, *Opt. Express* **2018**, *26*, 30623.
- [145] S. Molesky, Z. Lin, A. Y. Piggott, W. Jin, J. Vucković, A. W. Rodriguez, *Nat. Photonics* **2018**, *12*, 659.
- [146] S. So, T. Badloe, J. Noh, J. Bravo-Abad, J. Rho, *Nanophotonics* **2020**, *9*, 1041.
- [147] J. Jiang, M. Chen, J. A. Fan, *Nat. Rev. Mater.* **2020**, *6*, 679.
- [148] J. S. Jensen, O. Sigmund, *Laser Photonics Rev.* **2011**, *5*, 308.
- [149] J. Peurifoy, Y. Shen, L. Jing, Y. Yang, F. Cano-Renteria, B. G. DeLacy, J. D. Joannopoulos, M. Tegmark, M. Soljačić, *Sci. Adv.* **2018**, *4*, eaar4206.
- [150] S. Mao, L. Cheng, C. Zhao, F. N. Khan, Q. Li, H. Y. Fu, *Appl. Sci.* **2021**, *11*, 3822.
- [151] X. Tu, W. Xie, Z. Chen, M.-F. Ge, T. Huang, C. Song, H. Y. Fu, *J. Lightwave Technol.* **2021**, *39*, 2790.
- [152] L. Cheng, S. Mao, Z. Chen, Y. Wang, C. Zhao, H. Y. Fu, *Opt. Express* **2021**, *29*, 33728.
- [153] R. Yang, Y. Shi, C. Dai, C. Wan, S. Wan, Z. Li, *Opt. Lett.* **2020**, *45*, 5640.
- [154] M. Zhu, Y.-S. Lin, C. Lee, *J. Appl. Phys.* **2014**, *116*, 173106.
- [155] N. Wang, F.-L. Hsiao, M. Palaniapan, C. Lee, *J. Appl. Phys.* **2014**, *115*, 094904.
- [156] N. Wang, F.-L. Hsiao, J. M. Tsai, M. Palaniapan, D.-L. Kwong, C. Lee, *J. Micromech. Microeng.* **2013**, *23*, 065030.
- [157] Y.-S. Lin, Y. Qian, F. Ma, Z. Liu, P. Kropelnicki, C. Lee, *Appl. Phys. Lett.* **2013**, *102*, 111908.
- [158] N. Wang, J. M.-L. Tsai, F.-L. Hsiao, B. W. Soon, D.-L. Kwong, M. Palaniapan, C. Lee, *J. Microelectromech. Syst.* **2012**, *21*, 801.
- [159] N. Wang, F.-L. Hsiao, J. M. Tsai, M. Palaniapan, D.-L. Kwong, C. Lee, *J. Appl. Phys.* **2012**, *112*, 024910.
- [160] N. Wang, F.-L. Hsiao, M. Palaniapan, C. Lee, *Appl. Phys. Lett.* **2011**, *99*, 234102.
- [161] N. Wang, J. M. Tsai, F.-L. Hsiao, B. W. Soon, D.-L. Kwong, M. Palaniapan, C. Lee, *IEEE Electron Device Lett.* **2011**, *32*, 821.
- [162] M. Manjappa, P. Pitchappa, N. Singh, N. Wang, N. I. Zheludev, C. Lee, R. Singh, *Nat. Commun.* **2018**, *9*, 4056.
- [163] S. Gröblacher, K. Hammerer, M. R. Vanner, M. Aspelmeyer, *Nature* **2009**, *460*, 724.
- [164] Kun Wang, Ark-Chew Wong, C. T.-C. Nguyen, *J. Microelectromech. Syst.* **2000**, *9*, 347.
- [165] T. Makkonen, A. Holappa, J. Ella, M. M. Salomea, *IEEE Trans. Ultrason. Ferroelectr. Freq. Control* **2001**, *48*, 1241.
- [166] Y. Liu, Y. Cai, Y. Zhang, A. Tovstopyat, S. Liu, C. Sun, *Micromachines* **2020**, *11*, 630.
- [167] Chengkuo Lee, Fu-Li Hsiao, T. Kobayashi, Kah How Koh, P. V. Ramana, Wenfeng Xiang, bin Yang, Chee Wei Tan, D. Pinjala, *IEEE J. Sel. Top. Quantum Electron.* **2009**, *15*, 93.
- [168] K. H. Koh, T. Kobayashi, C. Lee, *IEEE Photonics Technol. Lett.* **2010**, *22*, 1355.
- [169] K. H. Koh, C. Lee, T. Kobayashi, *J. Microelectromech. Syst.* **2010**, *19*, 1370.
- [170] A. Unamuno, R. Blue, D. Uttamchandani, *J. Microelectromech. Syst.* **2013**, *22*, 1229.
- [171] K. Isamoto, K. Kato, A. Morosawa, C. Chong, H. Fujita, H. Toshiyoshi, *IEEE J. Sel. Top. Quantum Electron.* **2004**, *10*, 570.
- [172] K. H. Koh, T. Kobayashi, J. Xie, A. Yu, C. Lee, *J. Micromech. Microeng.* **2011**, *21*, 075001.
- [173] K. H. Koh, T. Kobayashi, C. Lee, *Sens. Actuators, A* **2012**, *184*, 149.
- [174] K. H. Koh, T. Kobayashi, C. Lee, *Opt. Express* **2011**, *19*, 13812.
- [175] K. H. Koh, T. Kobayashi, F.-L. Hsiao, C. Lee, *Sens. Actuators, A* **2010**, *162*, 336.
- [176] D. Wang, C. Watkins, H. Xie, *Micromachines* **2020**, *11*, 456.
- [177] B. Yang, *J. Micro/Nanolithogr., MEMS, MOEMS* **2010**, *9*, 023002.
- [178] Q. Shi, T. Wang, T. Kobayashi, C. Lee, *Appl. Phys. Lett.* **2016**, *108*, 193902.
- [179] H. Liu, S. Zhang, R. Kathiresan, T. Kobayashi, C. Lee, *Appl. Phys. Lett.* **2012**, *100*, 223905.
- [180] Q. Shi, T. Wang, C. Lee, *Sci. Rep.* **2016**, *6*, 24946.
- [181] H. Liu, C. J. Tay, C. Quan, T. Kobayashi, C. Lee, *Microsyst. Technol.* **2011**, *17*, 1747.
- [182] H. Liu, C. Lee, T. Kobayashi, C. J. Tay, C. Quan, *Sens. Actuators, A* **2012**, *186*, 242.
- [183] H. Liu, C. Lee, T. Kobayashi, C. J. Tay, C. Quan, *Smart Mater. Struct.* **2012**, *21*, 035005.
- [184] H. Liu, S. Zhang, T. Kobayashi, T. Chen, C. Lee, *Micro Nano Lett.* **2014**, *9*, 286.
- [185] H. Liu, C. J. Tay, C. Quan, T. Kobayashi, C. Lee, *J. Microelectromech. Syst.* **2011**, *20*, 1131.
- [186] D. S. Nguyen, E. Halvorsen, G. U. Jensen, A. Vogl, *J. Micromech. Microeng.* **2010**, *20*, 125009.
- [187] T. Wang, T. Kobayashi, C. Lee, *Appl. Phys. Lett.* **2015**, *106*, 013501.
- [188] T. Wang, R. Sawada, C. Lee, *IEEE Electron Device Lett.* **2015**, *36*, 957.
- [189] T. Wang, C. Lee, *J. Microelectromech. Syst.* **2015**, *24*, 2083.
- [190] T. Wang, T. Kobayashi, B. Yang, H. Wang, C. Lee, in *2016 IEEE 11th Annual Int. Conf. on Nano/Micro Engineered and Molecular Systems (NEMS)* (Ed.: S. Tanaka), IEEE, Piscataway, NJ **2016**, pp. 294–299.
- [191] K. Sakoda, *Optical Properties of Photonic Crystals*, Springer, Berlin **2005**.
- [192] C. López, *Adv. Mater.* **2003**, *15*, 1679.
- [193] C. P. Ho, P. Pitchappa, P. Kropelnicki, J. Wang, H. Cai, Y. Gu, C. Lee, *J. Nanophotonics* **2014**, *8*, 084096.
- [194] B. Li, C. P. Ho, F.-L. Hsiao, C. Lee, *J. Nanophotonics* **2014**, *8*, 084090.
- [195] B. Li, F.-L. Hsiao, C. Lee, *Sens. Actuators, A* **2011**, *169*, 352.
- [196] H.-T. Chien, C. Lee, H.-K. Chiu, K.-C. Hsu, C.-C. Chen, J.-A. A. Ho, C. Chou, *J. Lightwave Technol.* **2009**, *27*, 2570.
- [197] C. Lee, R. Radhakrishnan, C.-C. Chen, J. Li, J. Thillaigovindan, N. Balasubramanian, *J. Lightwave Technol.* **2008**, *26*, 839.

- [198] C. P. Ho, P. Pitchappa, P. Kropelnicki, J. Wang, H. Cai, Y. Gu, C. Lee, *Opt. Lett.* **2015**, *40*, 2743.
- [199] D. Marpaung, J. Yao, J. Capmany, *Nat. Photonics* **2019**, *13*, 80.
- [200] Y. Chassagneux, R. Colombelli, W. Maineult, S. Barbieri, H. E. Beere, D. A. Ritchie, S. P. Khanna, E. H. Linfield, A. G. Davies, *Nature* **2009**, *457*, 174.
- [201] R. K. Kushwaha, P. Karuppanan, L. D. Malviya, *Phys. B* **2018**, *545*, 107.
- [202] Q. Qiao, C. Peng, J. Xia, C. Lee, G. Zhou, *Opt. Express* **2019**, *27*, 35600.
- [203] Y. Chang, S. Xu, B. Dong, J. Wei, X. Le, Y. Ma, G. Zhou, C. Lee, *Nano Energy* **2021**, *89*, 106446.
- [204] C. P. Ho, P. Pitchappa, B. W. Soon, C. Lee, *Opt. Express* **2015**, *23*, 10598.
- [205] X. Wang, W. Shi, H. Yun, S. Grist, N. A. F. Jaeger, L. Chrostowski, *Opt. Express* **2012**, *20*, 15547.
- [206] P. B. Deotare, M. W. McCutcheon, I. W. Frank, M. Khan, M. Lončar, *Appl. Phys. Lett.* **2009**, *95*, 031102.
- [207] Q. Quan, P. B. Deotare, M. Loncar, *Appl. Phys. Lett.* **2010**, *96*, 203102.
- [208] Q. Qiao, J. Xia, C. Lee, G. Zhou, *Micromachines* **2018**, *9*, 541.
- [209] H. Zhou, D. Li, X. Hui, X. Mu, *Int. J. Optomechatron.* **2021**, *15*, 97.
- [210] J. S. Foresi, P. R. Villeneuve, J. Ferrera, E. R. Thoen, G. Steinmeyer, S. Fan, J. D. Joannopoulos, L. C. Kimerling, H. I. Smith, E. P. Ippen, *Nature* **1997**, *390*, 143.
- [211] F. Sun, Y. Yang, Z. Li, D. Yang, H. Tian, C. Lee, *Opt. Express* **2022**, *30*, 21764.
- [212] F. Sun, J. Wei, B. Dong, Y. Ma, Y. Chang, H. Tian, C. Lee, *Opt. Express* **2019**, *27*, 14085.
- [213] J. Wei, F. Sun, B. Dong, Y. Ma, Y. Chang, H. Tian, C. Lee, *Opt. Lett.* **2018**, *43*, 5407.
- [214] J. Haavisto, G. A. Pajer, *Opt. Lett.* **1980**, *5*, 510.
- [215] J. Ravi, R. Chandrasekar, *Adv. Opt. Mater.* **2021**, *9*, 2100550.
- [216] A. V. Kumar, E. Mamontov, T. Murzina, R. Chandrasekar, *Adv. Opt. Mater.* **2023**, *11*, 2201507.
- [217] P. T. Lin, V. Singh, H.-Y. G. Lin, T. Tiwald, L. C. Kimerling, A. M. Agarwal, *Adv. Opt. Mater.* **2013**, *1*, 732.
- [218] Y. Zou, S. Chakravarty, P. Wray, R. T. Chen, *Sens. Actuators, B* **2015**, *221*, 1094.
- [219] T.-P. Ngo, M. el Kurdi, X. Checoury, P. Boucaud, J. F. Damlencourt, O. Kermarrec, D. Bensahel, *Appl. Phys. Lett.* **2008**, *93*, 241112.
- [220] G. Poberaj, H. Hu, W. Sohler, P. Günter, *Laser Photonics Rev.* **2012**, *6*, 488.
- [221] A. Y. Liu, J. Bowers, *IEEE J. Sel. Top. Quantum Electron.* **2018**, *24*, 6000412.
- [222] W. Li, P. Anantha, S. Bao, K. H. Lee, X. Guo, T. Hu, L. Zhang, H. Wang, R. Soref, C. S. Tan, *Appl. Phys. Lett.* **2016**, *109*, 241101.
- [223] J. M. Ramirez, Q. Liu, V. Vakarin, J. Frigerio, A. Ballabio, X. le Roux, D. Bouville, L. Vivien, G. Isella, D. Marras-Morini, *Opt. Express* **2018**, *26*, 870.
- [224] C. Xiong, W. H. P. Pernice, H. X. Tang, *Nano Lett.* **2012**, *12*, 3562.
- [225] S. Zhu, G.-Q. Lo, *Opt. Express* **2016**, *24*, 12501.
- [226] N. Li, C. P. Ho, S. Zhu, Y. H. Fu, Y. Zhu, L. Y. T. Lee, *Nanophotonics* **2021**, *10*, 2347.
- [227] N. Li, C. P. Ho, Y. Cao, S. Zhu, G. F. R. Chen, Y. H. Fu, Y. Zhu, D. T. H. Tan, L. Y. T. Lee, in *Conf. on Lasers and Electro-Optics* (Ed.: C. Saraceno), Optica Publishing Group, Washington, D.C, **2021**, p. SThH.3.
- [228] B. Dong, X. Luo, S. Zhu, T. Hu, M. O. Li, D. Hasan, L. I. Zhang, S. J. Chua, J. Wei, Y. Chang, Y. Ma, P. Vachon, G.-Q. Lo, K. W. Ang, D.-L. Kwong, C. Lee, *Opt. Express* **2019**, *27*, 19815.
- [229] B. Dong, X. Luo, S. Zhu, M. Li, D. Hasan, L. Zhang, S. J. Chua, J. Wei, Y. Chang, G.-Q. Lo, K. W. Ang, D.-L. Kwong, C. Lee, *Opt. Lett.* **2019**, *44*, 73.
- [230] V. V. Pradeep, R. Chandrasekar, *Adv. Opt. Mater.* **2022**, *10*, 2201150.
- [231] B. Min, E. Ostby, V. Sorger, E. Ulin-Avila, L. Yang, X. Zhang, K. Vahala, *Nature* **2009**, *457*, 455.
- [232] B. Li, C. P. Ho, C. Lee, *IEEE Photonics J.* **2016**, *8*, 4501910.
- [233] B. Peng, Ş. K. Özdemir, W. Chen, F. Nori, L. Yang, *Nat. Commun.* **2014**, *5*, 5082.
- [234] F. Sun, F. Sun, F. Sun, F. Sun, B. Dong, B. Dong, J. Wei, J. Wei, Y. Ma, Y. Ma, H. Tian, H. Tian, C. Lee, C. Lee, C. Lee, *Opt. Express* **2020**, *28*, 30736.
- [235] C. P. Ho, B. Li, A. J. Danner, C. Lee, *Microsyst. Technol.* **2013**, *19*, 53.
- [236] B. Li, C. Lee, *Sens. Actuators, A* **2011**, *172*, 61.
- [237] G. Liang, C. Lee, A. J. Danner, *AIP Adv.* **2011**, *1*, 042171.
- [238] F. Hsiao, C. Lee, *IEEE Sens. J.* **2010**, *10*, 1185.
- [239] F. Sun, B. Dong, J. Wei, Y. Ma, H. Tian, C. Lee, *Opt. Express* **2020**, *28*, 30736.
- [240] F. Hsiao, C. Lee, *J. Micro/Nanolithogr., MEMS, MOEMS* **2011**, *10*, 013001.
- [241] V. M. N. Passaro, B. Troia, M. la Notte, F. de Leonardi, *RSC Adv.* **2013**, *3*, 25.
- [242] J. Hodgkinson, R. P. Tatam, *Meas. Sci. Technol.* **2013**, *24*, 012004.
- [243] Y. Zuo, Y. Gao, S. Qin, Z. Wang, D. Zhou, Z. Li, Y. Yu, M. Shao, X. Zhang, *Nanophotonics* **2019**, *9*, 123.
- [244] Y. Chen, H. Li, M. Li, *Sci. Rep.* **2012**, *2*, 622.
- [245] W. Li, Z. Wang, C. Feng, Q. Li, H. Yu, *Sens. Actuators, A* **2019**, *285*, 300.
- [246] X. Zhao, J. M. Tsai, H. Cai, X. M. Ji, J. Zhou, M. H. Bao, Y. P. Huang, D. L. Kwong, A. Q. Liu, *Opt. Express* **2012**, *20*, 8535.
- [247] H. C. Leo Tsui, O. Alsalmi, B. Mao, A. Alodhayb, H. Albritthen, A. P. Knights, M. P. Halsall, I. F. Crowe, *Sci. Rep.* **2020**, *10*, 9592.
- [248] X. Guan, X. Wang, L. H. Frandsen, *Opt. Express* **2016**, *24*, 16349.
- [249] Y. Zhang, J. Zou, Z. Cao, J.-J. He, *Opt. Lett.* **2019**, *44*, 299.
- [250] X. Liu, W. Liu, Z. Ren, Y. Ma, B. Dong, G. Zhou, C. Lee, *Int. J. Optomechatron.* **2021**, *15*, 120.
- [251] T. Wang, J. Wang, J. He, C. Wu, W. Luo, Y. Shuai, W. Zhang, C. Lee, *Sensors* **2018**, *18*, 1498.
- [252] N. N. Klimov, S. Mittal, M. Berger, Z. Ahmed, *Opt. Lett.* **2015**, *40*, 3934.
- [253] H. Li, Z. An, Q. Mao, S. Zuo, W. Zhu, S. Zhang, C. Zhang, E. Li, J. D. P. García, *Nanomaterials* **2021**, *12*, 29.
- [254] Y. Zhao, X. Li, X. Zhou, Y. Zhang, *Sens. Actuators, B* **2016**, *231*, 324.
- [255] Q. Sun, X. Sun, W. Jia, Z. Xu, H. Luo, D. Liu, L. Zhang, *IEEE Photonics Technol. Lett.* **2016**, *28*, 383.
- [256] Z. Li, J. Zou, H. Zhu, B. T. T. Nguyen, Y. Shi, P. Y. Liu, R. C. Bailey, J. Zhou, H. Wang, Z. Yang, Y. Jin, P. H. Yap, H. Cai, Y. Hao, A. Q. Liu, *ACS Sens.* **2020**, *5*, 2448.
- [257] N. Chandrasekhar, M. A. Mohiddin, R. Chandrasekar, *Adv. Opt. Mater.* **2013**, *1*, 305.
- [258] A. Vinod Kumar, M. Rohullah, M. Chosenyah, J. Ravi, U. Venkataramudu, R. Chandrasekar, *Angew. Chem., Int. Ed.* **2023**, *62*, e202300046.
- [259] Y. Ma, B. Dong, C. Lee, *Nano Convergence* **2020**, *7*, 12.
- [260] Y. Chang, B. Dong, Y. Ma, J. Wei, Z. Ren, C. Lee, *Opt. Express* **2020**, *28*, 6251.
- [261] N. T. Benítez, B. Baumgartner, J. Missinne, S. Radosavljevic, D. Wacht, S. Hugger, P. Leszcz, B. Lendl, G. Roelkens, *Opt. Express* **2020**, *28*, 27013.
- [262] W. Liu, Y. Ma, X. Liu, J. Zhou, C. Xu, B. Dong, C. Lee, *Nano Lett.* **2022**, *22*, 6112.
- [263] Z. Li, H. Zhang, B. T. T. Nguyen, S. Luo, P. Y. Liu, J. Zou, Y. Shi, H. Cai, Z. Yang, Y. Jin, Y. Hao, Y. Zhang, A.-Q. Liu, *Photonics Res.* **2021**, *9*, B38.
- [264] J. Zhou, Z. Zhang, B. Dong, Z. Ren, W. Liu, C. Lee, *ACS Nano* **2023**, *17*, 711.
- [265] F. Arab Hassani, Q. Shi, F. Wen, T. He, A. Haroun, Y. Yang, Y. Feng, C. Lee, *Smart Mater. Med.* **2020**, *1*, 92.

- [266] M. Zhu, Z. Yi, B. Yang, C. Lee, *Nano Today* **2021**, *36*, 101016.
- [267] M. Zhu, Z. Sun, T. Chen, C. Lee, *Nat. Commun.* **2021**, *12*, 2692.
- [268] Z. Zhang, Q. Shi, T. He, X. Guo, B. Dong, J. Lee, C. Lee, *Nano Energy* **2021**, *90*, 106517.
- [269] T. He, C. Lee, *IEEE Open J. Circuits Syst.* **2021**, *2*, 702.
- [270] X. Hou, M. Zhu, L. Sun, T. Ding, Z. Huang, Y. Shi, Y. Su, L. Li, T. Chen, C. Lee, *Nano Energy* **2022**, *93*, 106894.
- [271] Y. Pang, X. Zhu, C. Lee, S. Liu, *Nano Energy* **2022**, *97*, 107219.
- [272] T. He, F. Wen, Y. Yang, X. Le, W. Liu, C. Lee, *Anal. Chem.* **2023**, *95*, 490.
- [273] A. Panneer Selvam, S. Muthukumar, V. Kamakoti, S. Prasad, *Sci. Rep.* **2016**, *6*, 23111.
- [274] Y. Zhao, X. Hu, S. Hu, Y. Peng, *Biosens. Bioelectron.* **2020**, *166*, 112447.
- [275] B. Li, F.-L. Hsiao, C. Lee, *IEEE Trans. Nanotechnol.* **2011**, *10*, 789.
- [276] W. Xiang, C. Lee, *IEEE J. Sel. Top. Quantum Electron.* **2009**, *15*, 1323.
- [277] Y. Chang, D. Hasan, B. Dong, J. Wei, Y. Ma, G. Zhou, K. W. Ang, C. Lee, *ACS Appl. Mater. Interfaces* **2018**, *10*, 38272.
- [278] K. Shih, P. Pitchappa, L. Jin, C.-H. Chen, R. Singh, C. Lee, *Appl. Phys. Lett.* **2018**, *113*, 071105.
- [279] J. Xu, Z. Ren, B. Dong, X. Liu, C. Wang, Y. Tian, C. Lee, *ACS Nano* **2020**, *14*, 12159.
- [280] B. Dong, T. Hu, X. Luo, Y. Chang, X. Guo, H. Wang, D.-L. Kwong, G.-Q. Lo, C. Lee, *Nanomaterials* **2018**, *8*, 893.
- [281] M. Vlk, A. Datta, S. Alberti, H. D. Yallew, V. Mittal, G. S. Murugan, J. Jágorská, *Light: Sci. Appl.* **2021**, *10*, 26.
- [282] Z. Ren, Z. Zhang, J. Wei, B. Dong, C. Lee, *Nat. Commun.* **2022**, *13*, 3859.
- [283] H. Zhou, L. Xu, Z. Ren, J. Zhu, C. Lee, *Nanoscale Adv.* **2023**, *5*, 538.
- [284] J. Zhu, Z. Ren, C. Lee, *ACS Nano* **2021**, *15*, 894.
- [285] F. Wen, Z. Sun, T. He, Q. Shi, M. Zhu, Z. Zhang, L. Li, T. Zhang, C. Lee, *Adv. Sci.* **2020**, *7*, 2000261.
- [286] M. Zhu, T. He, C. Lee, *Appl. Phys. Rev.* **2020**, *7*, 031305.
- [287] Z. Zhang, T. He, M. Zhu, Z. Sun, Q. Shi, J. Zhu, B. Dong, M. R. Yuce, C. Lee, *npj Flexible Electron.* **2020**, *4*, 29.
- [288] Q. Shi, Z. Zhang, T. He, Z. Sun, B. Wang, Y. Feng, X. Shan, B. Salam, C. Lee, *Nat. Commun.* **2020**, *11*, 4609.
- [289] M. S. Yazici, B. Dong, D. Hasan, F. Sun, C. Lee, *Opt. Express* **2020**, *28*, 11524.
- [290] W. Tian, H. Zhou, L. Li, *Small* **2017**, *13*, 1702107.
- [291] L. Dou, Y. M. Yang, J. You, Z. Hong, W. H. Chang, G. Li, Y. Yang, *Nat. Commun.* **2014**, *5*, 5404.
- [292] J. Zhou, J. Huang, *Adv. Sci.* **2018**, *5*, 1700256.
- [293] J. Xue, Y. Gu, Q. Shan, Y. Zou, J. Song, L. Xu, Y. Dong, J. Li, H. Zeng, *Angew. Chem., Int. Ed.* **2017**, *56*, 5232.
- [294] C. Cheng, C. Zhu, B. Huang, H. Zhang, H. Zhang, R. Chen, W. Pei, Q. Chen, H. Chen, *Adv. Mater. Technol.* **2019**, *4*, 1800729.
- [295] L. Shen, E. Y. B. Pun, J. C. Ho, *Mater. Chem. Front.* **2017**, *1*, 630.
- [296] Z. Sheng, L. Liu, J. Brouckaert, S. He, D. van Thourhout, *Opt. Express* **2010**, *18*, 1756.
- [297] Z. Sheng, L. Liu, J. Brouckaert, S. He, D. van Thourhout, R. Baets, in *2009 IEEE Int. Conf. on Indium Phosphide & Related Materials* (Eds: T. Hussain, J. Schulman), IEEE, Piscataway, NJ **2009**, pp. 159–162.
- [298] H. Chen, P. Verheyen, P. de Heyn, G. Lepage, J. de Coster, S. Balakrishnan, P. Absil, W. Yao, L. Shen, G. Roelkens, J. van Campenhout, *Opt. Express* **2016**, *24*, 4622.
- [299] Y. Du, B. Xu, G. Wang, Y. Miao, B. Li, Z. Kong, Y. Dong, W. Wang, H. H. Radamson, *Nanomaterials* **2022**, *12*, 741.
- [300] Q. Liang, Q. Wang, Q. Zhang, J. Wei, S. X. Lim, R. Zhu, J. Hu, W. Wei, C. Lee, C. Sow, W. Zhang, A. T. S. Wee, *Adv. Mater.* **2019**, *31*, 1807609.
- [301] L. Huang, B. Dong, X. Guo, Y. Chang, N. Chen, X. Huang, W. Liao, C. Zhu, H. Wang, C. Lee, K.-W. Ang, *ACS Nano* **2019**, *13*, 913.
- [302] Y. Ma, B. Dong, J. Wei, Y. Chang, L. Huang, K. Ang, C. Lee, *Adv. Opt. Mater.* **2020**, *8*, 2000337.
- [303] P. L. Chen, Y. Chen, T. Y. Chang, W. Q. Li, J. X. Li, S. Lee, Z. Fang, M. Li, A. Majumdar, C. H. Liu, *ACS Appl. Mater. Interfaces* **2022**, *14*, 24856.
- [304] Y. Ma, Y. Chang, B. Dong, J. Wei, W. Liu, C. Lee, *ACS Nano* **2021**, *15*, 10084.
- [305] J. Wei, C. Xu, B. Dong, C.-W. Qiu, C. Lee, *Nat. Photonics* **2021**, *15*, 614.
- [306] F. Xia, T. Mueller, Y. Lin, A. Valdes-Garcia, P. Avouris, *Nat. Nanotechnol.* **2009**, *4*, 839.
- [307] M. Long, P. Wang, H. Fang, W. Hu, *Adv. Funct. Mater.* **2019**, *29*, 1803807.
- [308] A. D. Oyedele, S. Yang, L. Liang, A. A. Puretzky, K. Wang, J. Zhang, P. Yu, P. R. Pudasaini, A. W. Ghosh, Z. Liu, C. M. Rouleau, B. G. Sumpter, M. F. Chisholm, W. Zhou, P. D. Rack, D. B. Geohegan, K. Xiao, *J. Am. Chem. Soc.* **2017**, *139*, 14090.
- [309] Y. Ma, B. Dong, B. Li, K.-W. Ang, C. Lee, *Opt. Lett.* **2018**, *43*, 5504.
- [310] C. Xie, F. Yan, *ACS Appl. Mater. Interfaces* **2017**, *9*, 1569.
- [311] J. Wei, Y. Li, L. Wang, W. Liao, B. Dong, C. Xu, C. Zhu, K.-W. Ang, C.-W. Qiu, C. Lee, *Nat. Commun.* **2020**, *11*, 6404.
- [312] J. Wei, Y. Chen, Y. Li, W. Li, J. Xie, C. Lee, K. S. Novoselov, C.-W. Qiu, *Nat. Photonics* **2023**, *17*, 171.
- [313] K. Tan, Y. Huang, G.-Q. Lo, C. Lee, C. Yu, *Opt. Express* **2016**, *24*, 14506.
- [314] K. Tan, Y. Huang, G.-Q. Lo, C. Yu, C. Lee, *Opt. Express* **2017**, *25*, 3234.
- [315] A. Politis, M. J. Cryan, J. G. Rarity, S. Yu, J. L. O'Brien, *Science* **2008**, *320*, 646.
- [316] G. Zhou, Z. H. Lim, Y. Qi, F. S. Chau, G. Zhou, *Int. J. Optomechatron.* **2021**, *15*, 61.
- [317] X. Liu, Q. Qiao, B. Dong, W. Liu, C. Xu, S. Xu, G. Zhou, *Int. J. Optomechatron.* **2022**, *16*, 42.
- [318] S. Chung, M. Nakai, H. Hashemi, *Opt. Express* **2019**, *27*, 13430.
- [319] M. R. Watts, J. Sun, C. DeRose, D. C. Trotter, R. W. Young, G. N. Nielson, *Opt. Lett.* **2013**, *38*, 733.
- [320] C. Wang, M. Zhang, X. Chen, M. Bertrand, A. Shams-Ansari, S. Chandrasekhar, P. Winzer, M. Lončar, *Nature* **2018**, *562*, 101.
- [321] M. He, M. Xu, Y. Ren, J. Jian, Z. Ruan, Y. Xu, S. Gao, S. Sun, X. Wen, L. Zhou, L. Liu, C. Guo, H. Chen, S. Yu, L. Liu, X. Cai, *Nat. Photonics* **2019**, *13*, 359.
- [322] M. Xu, M. He, H. Zhang, J. Jian, Y. Pan, X. Liu, L. Chen, X. Meng, H. Chen, Z. Li, X. Xiao, S. Yu, S. Yu, X. Cai, *Nat. Commun.* **2020**, *11*, 3911.
- [323] M. Li, J. Ling, Y. He, U. A. Javid, S. Xue, Q. Lin, *Nat. Commun.* **2020**, *11*, 4123.
- [324] S. Xu, Z. Ren, B. Dong, J. Zhou, W. Liu, C. Lee, *Adv. Opt. Mater.* **2023**, *11*, 2202228.
- [325] W. M. Green, M. J. Rooks, L. Sekaric, Y. A. Vlasov, *Opt. Express* **2007**, *15*, 17106.
- [326] B. Dong, Y. Yang, Q. Shi, S. Xu, Z. Sun, S. Zhu, Z. Zhang, D. L. Kwong, G. Zhou, K. W. Ang, C. Lee, *ACS Nano* **2020**, *14*, 8915.
- [327] P. Edinger, A. Y. Takabayashi, C. Errando-Herranz, U. Khan, H. Sattari, P. Verheyen, W. Bogaerts, N. Quack, K. B. Gylfason, *Opt. Lett.* **2021**, *46*, 5671.
- [328] H. Sattari, T. Graziosi, M. Kiss, T. J. Seok, S. Han, M. C. Wu, N. Quack, *Opt. Express* **2019**, *27*, 18959.
- [329] H. Sun, Q. Qiao, J. Xia, C. Lee, G. Zhou, *Opt. Lett.* **2022**, *47*, 5801.
- [330] M. Wuttig, H. Bhaskaran, T. Taubner, *Nat. Photonics* **2017**, *11*, 465.
- [331] L. Huang, B. Dong, Z. G. Yu, J. Zhou, Y. Ma, Y.-W. Zhang, C. Lee, K.-W. Ang, *Mater. Today Adv.* **2021**, *12*, 100170.
- [332] V. Sorianello, M. Midrio, G. Contestabile, I. Asselberghs, J. Van Campenhout, C. Huyghebaert, I. Goykhman, A. K. Ott, A. C. Ferrari, M. Romagnoli, *Nat. Photonics* **2018**, *12*, 40.

- [333] Q. Qiao, M. S. Yazici, B. Dong, X. Liu, C. Lee, G. Zhou, *Opt. Lett.* **2020**, *45*, 5620.
- [334] Y. Li, H. Yu, T. Dai, J. Jiang, G. Wang, L. Yang, W. Wang, J. Yang, X. Jiang, *IEEE Photonics Technol. Lett.* **2016**, *28*, 284.
- [335] C. Ríos, M. Stegmaier, P. Hosseini, D. Wang, T. Scherer, C. D. Wright, H. Bhaskaran, W. H. P. Pernice, *Nat. Photonics* **2015**, *9*, 725.
- [336] C. Ríos, Q. Du, Y. Zhang, C.-C. Popescu, M. Y. Shalaginov, P. Miller, C. Roberts, M. Kang, K. A. Richardson, T. Gu, S. A. Vitale, J. Hu, *Photonix* **2022**, *3*, 26.
- [337] J. Geler-kremer, F. Eltes, P. Stark, D. Stark, D. Caimi, H. Siegwart, B. Jan Offrein, J. Fompeyrine, S. Abel, *Nat. Photonics* **2022**, *16*, 491.
- [338] W. Zhang, R. Mazzarello, M. Wuttig, E. Ma, *Nat. Rev. Mater.* **2019**, *4*, 150.
- [339] D. Ielmini, H. S. P. Wong, *Nat. Electron.* **2018**, *1*, 333.
- [340] A. Sebastian, M. Le Gallo, R. Khaddam-Aljameh, E. Eleftheriou, *Nat. Nanotechnol.* **2020**, *15*, 529.
- [341] Z. Zhang, Z. Wang, T. Shi, C. Bi, F. Rao, Y. Cai, Q. Liu, H. Wu, P. Zhou, *InfoMat* **2020**, *2*, 261.
- [342] S. Hong, in *2010 Int. Electron Devices Meeting* (Ed.: M. Ieong), IEEE, Piscataway, NJ **2010**, pp. 12.4.1–12.4.4.
- [343] C. A. Barrios, M. Lipson, *J. Light. Technol.* **2006**, *24*, 2898.
- [344] J. Song, X. Luo, A. E. Lim, C. Li, Q. Fang, T. Liow, L.-X. Jia, X.-G. Tu, Y. Huang, H.-F. Zhou, G.-Q. Lo, *Sci. Rep.* **2016**, *6*, 22616.
- [345] H. Lai, Y. Zhou, H. Zhou, N. Zhang, X. Ding, P. Liu, X. Wang, W. Xie, *Adv. Mater.* **2022**, *34*, 2110278.
- [346] C. Liu, X. Zou, M. Wu, Y. Wang, Y. Lv, X. Duan, S. Zhang, X. Liu, W. Wu, W. Hu, Z. Fan, L. Liao, *Adv. Funct. Mater.* **2021**, *31*, 2100781.
- [347] Y. Sun, M. Li, Y. Ding, H. Wang, H. Wang, Z. Chen, D. Xie, *InfoMat* **2022**, *4*, e12317.
- [348] A. Sawa, *Mater. Today* **2008**, *11*, 28.
- [349] M. A. A. Mohd Abdah, N. H. N. Azman, S. Kulandaivalu, Y. Sulaiman, *Mater. Des.* **2020**, *186*, 108199.
- [350] Y. Zhang, P. Wu, Z. Zhou, X. Chen, Z. Yi, J. Zhu, T. Zhang, H. Jile, *IEEE Access* **2020**, *8*, 85154.
- [351] R. Shi, N. Shen, J. Wang, W. Wang, A. Amini, N. Wang, C. Cheng, *Appl. Phys. Rev.* **2019**, *6*, 011312.
- [352] I. Olivares, L. Sánchez, J. Parra, R. Larrea, A. Griol, M. Menghini, P. Homm, L.-W. Jang, B. van Bilzen, J. W. Seo, J.-P. Locquet, P. Sanchis, *Opt. Express* **2018**, *26*, 12387.
- [353] Y. Jung, H. Han, A. Sharma, J. Jeong, S. S. P. Parkin, J. K. S. Poon, *ACS Photonics* **2022**, *9*, 217.
- [354] B. Zhi, G. Gao, H. Xu, F. Chen, X. Tan, P. Chen, L. Wang, W. Wu, *ACS Appl. Mater. Interfaces* **2014**, *6*, 4603.
- [355] M. Nakano, K. Shibuya, D. Okuyama, T. Hatano, S. Ono, M. Kawasaki, Y. Iwasa, Y. Tokura, *Nature* **2012**, *487*, 459.
- [356] B. Hu, Y. Ding, W. Chen, D. Kulkarni, Y. Shen, V. V. Tsukruk, Z. L. Wang, *Adv. Mater.* **2010**, *22*, 5134.
- [357] J. Wang, L. Wang, J. Liu, *IEEE Access* **2020**, *8*, 121211.
- [358] C. Wu, H. Yu, H. Li, X. Zhang, I. Takeuchi, M. Li, *ACS Photonics* **2019**, *6*, 87.
- [359] N. Youngblood, C. Talagrand, B. F. Porter, C. G. Galante, S. Kneepkens, G. Triggs, S. Ghazi Sarwat, D. Yarmolich, R. S. Bonilla, P. Hosseini, R. A. Taylor, H. Bhaskaran, *ACS Photonics* **2022**, *9*, 90.
- [360] Z. Fang, R. Chen, J. Zheng, A. I. Khan, K. M. Neilson, S. J. Geiger, D. M. Callahan, M. G. Moebius, A. Saxena, M. E. Chen, C. Rios, J. Hu, E. Pop, A. Majumdar, *Nat. Nanotechnol.* **2022**, *17*, 842.
- [361] C. Ríos, Y. Zhang, M. Y. Shalaginov, S. Deckoff-Jones, H. Wang, S. An, H. Zhang, M. Kang, K. A. Richardson, C. Roberts, J. B. Chou, V. Liberman, S. A. Vitale, J. Kong, T. Gu, J. Hu, *Adv. Photonics Res.* **2021**, *2*, 2000034.
- [362] Z. Guan, H. Hu, X. Shen, P. Xiang, N. Zhong, J. Chu, C. Duan, *Adv. Electron. Mater.* **2020**, *6*, 1900818.
- [363] L. W. Martin, A. M. Rappe, *Nat. Rev. Mater.* **2016**, *2*, 16087.
- [364] J. Geler-kremer, F. Eltes, P. Stark, D. Stark, D. Caimi, H. Siegwart, B. J. Offrein, J. Fompeyrine, S. Abel, F. Eltes, J. E. Ortmann, A. Messner, P. Castera, T. Wagner, D. Urbonas, A. Rosa, A. M. Gutierrez, D. Tulli, P. Ma, B. Baeuerle, A. Josten, W. Heni, D. Caimi, L. Czornomaz, A. A. Demkov, J. Leuthold, P. Sanchis, J. Fompeyrine, *Nat. Mater.* **2019**, *18*, 42.
- [365] J. Feldmann, N. Youngblood, C. D. Wright, H. Bhaskaran, W. H. P. Pernice, *Nature* **2019**, *569*, 208.
- [366] D. Pérez-López, A. López, P. DasMahapatra, J. Capmany, *Nat. Commun.* **2020**, *11*, 6359.
- [367] M. Prabhu, C. Roques-Carmes, Y. Shen, N. Harris, L. Jing, J. Carolan, R. Hamerly, T. Baehr-Jones, M. Hochberg, V. Čeperič, J. D. Joannopoulos, D. R. Englund, M. Soljačić, *Optica* **2020**, *7*, 551.
- [368] C. Wu, X. Yang, H. Yu, R. Peng, I. Takeuchi, Y. Chen, M. Li, *Sci. Adv.* **2022**, *8*, 2956.
- [369] S. Xu, J. Wang, S. Yi, W. Zou, *Nat. Commun.* **2022**, *13*, 7970.
- [370] B. Bai, Q. Yang, H. Shu, L. Chang, F. Yang, B. Shen, Z. Tao, J. Wang, S. Xu, W. Xie, W. Zou, W. Hu, J. E. Bowers, X. Wang, *Nat. Commun.* **2023**, *14*, 66.
- [371] J. Cheng, W. Zhang, W. Gu, H. Zhou, J. Dong, X. Zhang, *ACS Photonics* **2022**, *10*, 2173.
- [372] X. Xu, M. Tan, B. Corcoran, J. Wu, A. Boes, T. G. Nguyen, S. T. Chu, B. E. Little, D. G. Hicks, R. Morandotti, A. Mitchell, D. J. Moss, *Nature* **2021**, *589*, 44.
- [373] Y. Shen, N. C. Harris, S. Skirlo, M. Prabhu, T. Baehr-Jones, M. Hochberg, X. Sun, S. Zhao, H. Larochelle, D. Englund, M. Soljačić, *Nat. Photonics* **2017**, *11*, 441.
- [374] H. Zhang, M. Gu, X. D. Jiang, J. Thompson, H. Cai, S. Paesani, R. Santagati, A. Laing, Y. Zhang, M. H. Yung, Y. Z. Shi, F. K. Muhammad, G. Q. Lo, X. S. Luo, B. Dong, D. L. Kwong, L. C. Kwek, A. Q. Liu, *Nat. Commun.* **2021**, *12*, 457.
- [375] F. Ashtiani, A. J. Geers, F. Aflatouni, *Nature* **2022**, *606*, 501.
- [376] X. Xu, G. Ren, T. Feleppa, X. Liu, A. Boes, A. Mitchell, A. J. Lowery, *Nat. Photonics* **2022**, *16*, 595.
- [377] Y. Shi, J. Ren, G. Chen, W. Liu, C. Jin, X. Guo, Y. Yu, X. Zhang, *Nat. Commun.* **2022**, *13*, 6048.
- [378] H. Zhou, Y. Zhao, X. Wang, D. Gao, J. Dong, X. Zhang, *ACS Photonics* **2020**, *7*, 792.
- [379] H. Zhang, J. Thompson, M. Gu, X. D. Jiang, H. Cai, P. Y. Liu, Y. Shi, Y. Zhang, M. F. Karim, G. Q. Lo, X. Luo, B. Dong, L. C. Kwek, A. Q. Liu, *ACS Photonics* **2021**, *8*, 1662.
- [380] G. Cong, N. Yamamoto, T. Inoue, Y. Maegami, M. Ohno, S. Kita, S. Namiki, K. Yamada, *Nat. Commun.* **2022**, *13*, 3261.
- [381] I. A. D. Williamson, T. W. Hughes, M. Minkov, B. Bartlett, S. Pai, S. Fan, *IEEE J. Sel. Top. Quantum Electron.* **2020**, *26*, 7700412.
- [382] B. Dong, Q. Shi, T. He, S. Zhu, Z. Zhang, Z. Sun, Y. Ma, D. Kwong, C. Lee, *Adv. Sci.* **2020**, *7*, 1903636.
- [383] X. Zhang, K. Kwon, J. Henriksson, J. Luo, M. C. Wu, *Nature* **2022**, *603*, 253.
- [384] H. Shu, L. Chang, Y. Tao, B. Shen, W. Xie, M. Jin, A. Netherton, Z. Tao, X. Zhang, R. Chen, B. Bai, J. Qin, S. Yu, X. Wang, J. E. Bowers, *Nature* **2022**, *605*, 457.
- [385] Q. Shi, B. Dong, T. He, Z. Sun, J. Zhu, Z. Zhang, C. Lee, *InfoMat* **2020**, *2*, 1131.
- [386] J. Zhu, M. Zhu, Q. Shi, F. Wen, L. Liu, B. Dong, A. Haroun, Y. Yang, P. Vachon, X. Guo, T. He, C. Lee, *EcoMat* **2020**, *2*, e12058.
- [387] C. Wang, Q. Shi, C. Lee, *Nanomaterials* **2022**, *12*, 1366.
- [388] Q. Shi, Y. Yang, Z. Sun, C. Lee, *ACS Mater. Au* **2022**, *2*, 394.
- [389] H. Wang, T. Wu, Q. Zeng, C. Lee, *Micromachines* **2020**, *11*, 865.
- [390] Q. Shi, Z. Zhang, T. Chen, C. Lee, *Nano Energy* **2019**, *62*, 355.
- [391] M. Zhu, Z. Sun, Z. Zhang, Q. Shi, T. He, H. Liu, T. Chen, C. Lee, *Sci. Adv.* **2020**, *6*, eaaz8693.
- [392] G. Tang, Q. Shi, Z. Zhang, T. He, Z. Sun, C. Lee, *Nano Energy* **2021**, *81*, 105582.

- [393] Z. Sun, M. Zhu, C. Lee, *Nanoenergy Adv.* **2021**, *1*, 81.
- [394] L. Liu, Q. Shi, Z. Sun, C. Lee, *Nano Energy* **2021**, *86*, 106154.
- [395] X. Le, Q. Shi, Z. Sun, J. Xie, C. Lee, *Adv. Sci.* **2022**, *9*, 2201056.
- [396] Z. Sun, M. Zhu, X. Shan, C. Lee, *Nat. Commun.* **2022**, *13*, 5224.
- [397] J. Zhu, S. Ji, J. Yu, H. Shao, H. Wen, H. Zhang, Z. Xia, Z. Zhang, C. Lee, *Nano Energy* **2022**, *103*, 107766.
- [398] C. v. Poulton, A. Yaacobi, D. B. Cole, M. J. Byrd, M. Raval, D. Vermeulen, M. R. Watts, *Opt. Lett.* **2017**, *42*, 4091.
- [399] J. Park, B. G. Jeong, S. il Kim, D. Lee, J. Kim, C. Shin, C. B. Lee, T. Otsuka, J. Kyoung, S. Kim, K.-Y. Yang, Y.-Y. Park, J. Lee, I. Hwang, J. Jang, S. H. Song, M. L. Brongersma, K. Ha, S.-W. Hwang, H. Choo, B. L. Choi, *Nat. Nanotechnol.* **2021**, *16*, 69.
- [400] T. Raj, F. H. Hashim, A. B. Huddin, M. F. Ibrahim, A. Hussain, *Electronics* **2020**, *9*, 741.
- [401] A. Rueda, F. Sedlmeir, M. Kumari, G. Leuchs, H. G. L. Schwefel, *Nature* **2019**, *568*, 378.
- [402] V. Torres-Company, A. M. Weiner, *Laser Photonics Rev.* **2014**, *8*, 368.
- [403] P. Del'Haye, O. Arcizet, A. Schliesser, R. Holzwarth, T. J. Kippenberg, *Phys. Rev. Lett.* **2008**, *101*, 053903.
- [404] T. Fortier, E. Baumann, *Commun. Phys.* **2019**, *2*, 153.
- [405] J. Mishra, T. P. McKenna, E. Ng, H. S. Stokowski, M. Jankowski, C. Langrock, D. Heydari, H. Mabuchi, M. M. Fejer, A. H. Safavi-Naeini, *Optica* **2021**, *8*, 921.
- [406] J. Ravi, T. Feiler, A. Mondal, A. A. L. Michalchuk, C. M. Reddy, B. Bhattacharya, F. Emmerling, R. Chandrasekar, *Adv. Opt. Mater.* **2023**, *11*, 2201518.
- [407] A. Vinod Kumar, R. Chandrasekar, *J. Mater. Chem. C* **2023**, *11*, 7995.
- [408] F. Balzer, V. G. Bordo, A. C. Simonsen, H.-G. Rubahn, *Appl. Phys. Lett.* **2003**, *82*, 10.
- [409] R. Chandrasekar, *Adv. Opt. Mater.* **2023**, *11*, 2301124.
- [410] R. Chandrasekar, *Phys. Chem. Chem. Phys.* **2014**, *16*, 7173.
- [411] M. Annadhasan, A. R. Agrawal, S. Bhunia, V. V. Pradeep, S. S. Zade, C. M. Reddy, R. Chandrasekar, *Angew. Chem., Int. Ed.* **2020**, *59*, 13852.
- [412] M. Annadhasan, S. Basak, N. Chandrasekhar, R. Chandrasekar, *Adv. Opt. Mater.* **2020**, *8*, 2000959.
- [413] R. Chinnasamy, J. Ravi, V. Vinay Pradeep, D. Manoharan, F. Emmerling, B. Bhattacharya, S. Ghosh, R. Chandrasekar, *Chemistry - Eur. J.* **2022**, *28*, e202200905.
- [414] A. V. Kumar, R. Chandrasekar, *Adv. Opt. Mater.* **2023**, *11*, 2201009.
- [415] N. Mitetelo, J. Ravi, S. Mondal, U. Venkataramudu, E. Mamnov, M. Popov, A. Maydykovskiy, G. Vaiteeswaran, T. Murzina, R. Chandrasekar, *Adv. Opt. Mater.* **2023**, *11*, 2201635.
- [416] J. Clark, G. Lanzani, *Nat. Photonics* **2010**, *4*, 438.
- [417] X. Hu, P. Jiang, C. Ding, H. Yang, Q. Gong, *Nat. Photonics* **2008**, *2*, 185.
- [418] M.-P. Zhuo, Y.-C. Tao, X.-D. Wang, Y. Wu, S. Chen, L.-S. Liao, L. Jiang, *Angew. Chem.* **2018**, *130*, 11470.
- [419] C. Zhang, C.-L. Zou, Y. Zhao, C.-H. Dong, C. Wei, H. Wang, Y. Liu, G.-C. Guo, J. Yao, Y. S. Zhao, *Sci. Adv.* **2015**, *1*, e1500257.
- [420] A. V. Kumar, M. Godumala, J. Ravi, R. Chandrasekar, *Angew. Chem., Int. Ed.* **2022**, *61*, e202212382.
- [421] J. Ravi, A. V. Kumar, D. P. Karothu, M. Annadhasan, P. Naumov, R. Chandrasekar, *Adv. Funct. Mater.* **2021**, *31*, 2105415.
- [422] J. Ravi, M. Annadhasan, A. V. Kumar, R. Chandrasekar, *Adv. Funct. Mater.* **2021**, *31*, 2100642.
- [423] J. Ravi, A. Vinod Kumar, M. Annadhasan, R. Chandrasekar, *Adv. Opt. Mater.* **2022**, *10*, 2102545.
- [424] V. Vinay Pradeep, C. Tardío, I. Torres-Moya, A. M. Rodríguez, A. Vinod Kumar, M. Annadhasan, A. Hoz, P. Prieto, R. Chandrasekar, *Small* **2021**, *17*, 2006795.



**Zian Xiao** received his B.Eng. degree from the School of Electronic and Information at Soochow University, Suzhou, China, in 2020. After that, he received his M.Sc. degree from the Department of Electrical and Computer Engineering (ECE), National University of Singapore (NUS), in 2021. He is currently a Ph.D. student in the Department of ECE, NUS. His research interests are focused on specific integrated photonics circuits for artificial intelligence.



**Weixin Liu** received his B.Eng. degree in mechatronics engineering from the School of Mechanical Engineering at Zhejiang University, Hangzhou, China, in 2019. He is currently a Ph.D. candidate in the Department of ECE, NUS. His research interests focus mainly on MEMS piezoelectric resonant sensors and nanophotonic waveguides.



**Chengkuo Lee** received Ph.D. degree in precision engineering from the University of Tokyo in 1996. He is currently the GlobalFoundries Chair Professor of Engineering and the director of the Center for Intelligent Sensors and MEMS, National University of Singapore. In 2001, he cofounded Asia Pacific Microsystems, Inc., where he was the vice president. From 2006 to 2009, he was a senior member of the technical staff with the Institute of Microelectronics, A-STAR, Singapore.